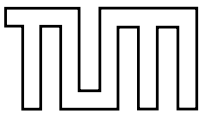

Technische Universität München
Ingenieurfakultät Bau Geo Umwelt
Fachgebiet Satellitengeodäsie

Refinement of Reduced-Dynamic Orbit Determination for Low Earth Satellites

Dissertation

von
Stefan Hackel

Technische Universität München
Ingenieurfakultät Bau Geo Umwelt
Fachgebiet Satellitengeodäsie

Refinement of Reduced-Dynamic Orbit Determination for Low Earth Satellites

Stefan Franz Gerhard Hackel

Vollständiger Abdruck der von der Ingenieurfakultät Bau Geo Umwelt der Technischen Universität München zur Erlangung des akademischen Grades eines

Doktor - Ingenieurs

genehmigten Dissertation.

Vorsitzender:		Prof. Dr. rer. nat. Thomas Kolbe
Prüfer der Dissertation:	1.	Priv.-Doz. Dr. rer. nat. habil. Oliver Montenbruck
	2.	Prof. Dr. phil. nat. Urs Hugentobler
	3.	Prof. Dr. Adrian Jäggi, Universität Bern, Schweiz

Die Dissertation wurde am 04.02.2019 bei der Technischen Universität München eingereicht und durch die Ingenieurfakultät Bau Geo Umwelt am 22.05.2019 angenommen.

Contents

Summary

Precise orbit information for Earth observation satellites gains ever more importance as the request for high quality remote sensing products increases. Global Positioning System (GPS)-based reduced-dynamic orbit determination has evolved as the state-of-the-art for high-precision orbit estimation of low altitude spacecraft. It combines a priori models of the spacecraft dynamics with varying levels of empirical parameters to best exploit the high precision of the available GPS observations. The optimum trade-off between the quality of dynamical models, the required level of stochastic parameters, and the geometric strength of the GPS observations is a matter of ongoing research and focus of this work. Given the high quality of orbit determination solutions that has been demonstrated even without any non-gravitational force models in missions such as CHAllenging Minisatellite Payload (CHAMP), Gravity Recovery And Climate Experiment (GRACE), Gravity field and steady-state Ocean Circulation Explorer (GOCE), and Swarm, the present thesis aims to answer the question whether and to what extent refined dynamical models and refined GPS processing techniques can contribute to further improve the achievable orbit determination accuracy.

The study is based on a comprehensive set of current Earth observation missions in low Earth orbit that are equipped with geodetic-grade GPS receivers. This comprises the Sentinel-1A, Swarm-C, and TerraSAR-X/TanDEM-X missions with altitude of 450 km to 693 km, where notable perturbations due to atmospheric forces affect the satellite motion. For each of these missions, dedicated macro models have been established and used for the description of atmospheric drag and lift forces, solar radiation pressure, and Earth radiation pressure with targeted modeling accuracies at the one nm/s^2 level. The benefit of using such models is assessed through different performance metrics

including self-consistency tests, satellite laser ranging (SLR), and radar ranging as an external validation technique.

Use of advanced atmospheric density models and spacecraft macro models for atmospheric forces is found to slightly reduce the associated empirical accelerations but does not allow to entirely waive the estimation of such parameters. With respect to radiation pressure, the macro model appear to be essential for a realistic description of Earth radiation pressure (ERP). In particular, it benefits the modeling of the radial ERP acceleration, which directly impacts the height leveling of the resulting orbit, and is such of key relevance for altimetry missions.

With respect to GPS observation modeling, the use of ambiguity fixing is shown as a key technique to achieve improved orbit determination accuracy for all orbit geometries. Its benefit largely outweigh that of non-gravitational force models and contribute to major improvements in the horizontal (along-track/cross-track) position knowledge. On the other hand, the reduced vertical dilution of precision still makes the resulting orbit solutions sensitive to geometric orbit modeling errors in radial direction and justifies the use of refined radial acceleration models. Overall, ambiguity fixing can offer 33 % improvement in orbit determination accuracy and allows to reach a one-cm level (1-D) performance, as evidenced by the analysis of SLR residuals for the aforementioned missions.

Radar-ranging is shown to enable independent validation of precise orbit determination solutions in Synthetic Aperture Radar (SAR) missions. However, it is not yet fully competitive with SLR in terms of both accuracy and coverage. In particular, it is confined to high resolution SAR imaging, and a global network of corner cube reflectors would be required for a wider use.

Zusammenfassung

Präzise Bahninformation von Erdbeobachtungssatelliten gewinnt bei steigendem Bedarf an genauen und zuverlässigen Fernerkundungsdaten zunehmend an Bedeutung. Global Positioning System (GPS)-basierte reduziert-dynamische Bahnbestimmung hat sich als Technik für die präzise Bahnbestimmung niedrig fliegender Satelliten etabliert. Hierbei werden a priori Modelle der Satellitendynamik mit unterschiedlichen Stufen an empirischen Parametern kombiniert, um die hohe Genauigkeit der verfügbaren GPS-Beobachtungen bestmöglich zu nutzen. Das optimale Verhältnis zwischen der Qualität der dynamischen Modelle, dem benötigten Maß an empirischen Beschleunigungen sowie dem geometrischen Gewicht der GPS-Beobachtungen ist Gegenstand der Forschung und im Fokus dieser Arbeit. In Anbetracht der hohen Qualität von Bahnlösungen beispielsweise von CHAllenging Minisatellite Payload (CHAMP), Gravity Recovery And Climate Experiment (GRACE), Gravity field and steady-state Ocean Circulation Explorer (GOCE) und Swarm, die komplett ohne nicht-gravitative Kräftemodelle auskommen, wird in der vorliegenden Arbeit die Frage untersucht, ob und in welchem Ausmaß verfeinerte dynamische Modelle und Techniken der GPS-Prozessierung zu einer verbesserten Bahngenauigkeit beitragen.

Die Arbeit stützt sich auf eine Auswahl aktueller Erdbeobachtungssatelliten im niedrigen Erdorbit, welche mit geodätisch-qualifizierten GPS-Empfängern ausgestattet sind. Konkret stehen die Satelliten Sentinel-1A, Swarm-C und TerraSAR-X/TanDEM-X mit einer Bahnhöhe zwischen 450 km und 693 km im Fokus, wo verstärkt atmosphärische Kräfte die Bahnbewegung des Satelliten beeinflussen. Für jede dieser Missionen wurden Plattenmodelle entwickelt und für die Modellierung der Luftreibung, des solaren Strahlungsdrucks und des Erdstrahlungsdrucks angewendet. Die angestrebte Modellierungsgenauigkeit liegt hier im Bereich von einem nm/s^2. Der Einfluss dieser Modelle auf die Bahnlösungen wird anhand verschiedener Qualitätsmetriken untersucht. Hierzu zählen Tests zur Selbstkonsistenz sowie Satellite Laser Ranging (SLR) und radarbasierte Entfernungsmessung als externe Technik zur Validierung.

Die Verwendung moderner atmosphärischer Dichtemodelle in Kombination mit den genannten Plattenmodellen führt zu einer leichten Reduzierung der empirischen Beschleunigungen, erlaubt aber nicht den Verzicht auf diese. Besondere Bedeutung erlangen die Plattenmodelle bei der Modellierung des Erdstrahlungsdrucks. Die resultierende Beschleunigung wirkt primär in radialer Richtung und beeinflusst somit die Lagerung der

Bahn in dieser Richtung, ein Aspekt, der insbesonders bei Altimetrie-Missionen wichtig ist.

Im Hinblick auf die Modellierung der GPS-Beobachtungen erwies sich die Fixierung der Mehrdeutigkeiten als Schlüsseltechnik zu einer verbesserten Bahngenauigkeit für sämtliche untersuchte Orbitgeometrien. Der erlangte Nutzen überwiegt größtenteils denen der nicht-gravitativen Kräftemodelle, wie sich in signifikanten Verbesserungen der horizontalen (entlang und quer zur Flugrichtung) Positionskenntnis zeigt. Zum Anderen sind die resultierenden Bahnlösungen auf Grund der reduzierten vertikalen Dilution of Precision (DOP) sensitiv für radiale geometrische Modellfehler. Aus diesem Grund werden exakte radiale Beschleunigungsmodelle benötigt. Zusammenfassend zeigen die Lösungen mit fixierten Mehrdeutigkeiten eine 33 % Verbesserung in der Bahnbestimmungsgenauigkeit und erlauben eine Bahnbestimmung im ein-cm-Bereich (1-D), wie SLR-Residuen der genannten Missionen zeigen.

Die radarbasierte Validierung der Bahnlösungen dient als weitere unabhängige Technik für Synthetic Aperture Radar (SAR) Missionen. Mit Hinblick auf Genauigkeit und Abdeckung ist dieses Verfahren nicht mit SLR gleichzusetzen. Speziell die Eingrenzung auf SAR-Missionen limitiert den Nutzerkreis, aber auch der Ausbau des Netzes mit geeigneten Reflektoren wäre für eine weitere Nutzung erforderlich.

1

Introduction

The first section of the introduction highlights the motivation behind the present study as well as the research contributions. State-of-the-art orbit modeling techniques are explained in the second section. The third and last section briefly elaborates the structure of this study.

1.1 Motivation

Satellites play an important role in geodesy and for Earth observation, as the geodetical or optical sensors in space provide huge amounts of spatial data with high resolution [Heipke, 2017]. The techniques often require knowledge of the satellite orbits, either for geo-referencing or validating the correction models, applied in the data preprocessing of the Earth observation data. Since most Earth observing satellites are low Earth orbiters, Global Navigation Satellite System (GNSS) measurements provide an excellent basis for accurately determining the position and velocity of such spacecraft. Depending on the extent, to which the GNSS observations are combined with dynamical models of satellite motion, three categories of precise orbit determination (POD) are distinguished, which are known as kinematic, dynamic, and reduced-dynamic. While

reduced-dynamic orbit determination represents the most widely applied concept for GNSS-based POD, present implementations differ widely concerning the quality of a priori models for the satellite dynamics and the amount of stochastic parameters. Within this study, refined non-gravitational models serve for improving the dynamics within the applied reduced-dynamic orbit determination approach. For this purpose, a satellite macro model is applied, which describes the geometry as well as the optical properties of the satellite surface. This panel model is employed for modeling surface-related accelerations like solar and Earth radiation pressure. Another dominant non-gravitational component are aerodynamic accelerations, since the spacecraft in low Earth orbit are exposed molecules from the remaining atmosphere. For deriving satellite orbits of highest quality, several atmospheric density models and different drag and lift implementations are introduced and assessed. Improving the GNSS processing by means of higher-order ionospheric corrections and estimating carrier phase integer ambiguities lead to further improvements of the orbit solutions. First, appropriate models are introduced and subsequently analyzed by means of their influence on the orbits. The resulting orbit solutions are validated by optical satellite laser ranging (SLR) measurements, and radar range measurements. This unique technique is finally employed to assess the quality of POD solutions and compared to classical orbit validation techniques like satellite laser ranging.

Since the reduced-dynamic orbit determination approach incorporates both dynamical models and GNSS observations, the key question of this research is: how much empiricism in terms of empirical accelerations is sufficient to significantly increase precision of the derived spacecraft orbits.

The present study builds on Global Positioning System (GPS) data from the Earth observation spacecraft TerraSAR-X, TanDEM-X, Sentinel-1A, and Swarm-C. Both, the Terra-SAR-X and the TanDEM-X spacecraft carry an advanced high-frequency multimode Synthetic Aperture Radar (SAR) X-band sensor for high-resolution mapping of the Earth surface on a global scale [Buckreuss et al., 2003; Eineder et al., 2003]. At an altitude of 515 km, the spacecraft experience notable drag forces, and the dusk-dawn geometry results in a pronounced lateral radiation pressure. For precise orbit determination and validation, the satellites are equipped with a dual-frequency GPS receiver as well as a laser retro reflector. Sentinel-1A carries a C-Band SAR in an altitude of 693 km [Attema et al., 2012; Torres et al., 2012]. The spacecraft is also equipped with a dual-frequency GPS receiver, which supports testing of refined satellite dynamics and GPS processing models and techniques. The spacecraft Swarm-C is part the Earth mag-

netic field observation mission Swarm, launched in 2013, and orbiting the Earth in an altitude of 450 km [Friis-Christensen et al., 2008]. This spacecraft is primarily selected for assessing the influence of the ambiguity fixing technique.

1.2 Orbit Determination Concepts

The three-dimensional nature of GPS measurements provides an excellent basis for accurately determining the position and velocity of low Earth orbit (LEO) satellites. Depending on the extent, to which the GPS observations are combined with dynamical models of satellite motion, three categories of POD are distinguished. These are commonly known as kinematic, dynamic, and reduced-dynamic POD. Among others, a description of the different orbit determination concepts is available in Rim and Schutz [2002], GPS-based concepts are introduced in Gill and Montenbruck [2004].

Kinematic Orbit Determination The kinematic approach is exclusively based on GPS (or, more generally, GNSS) measurements and does not involve any dynamical models at all. Similar to precise point positioning [PPP; Zumberge et al., 1997; Kouba and Héroux, 2001], the kinematic POD is typically performed with undifferenced observations and makes use of precomputed GNSS orbit and clock products, that are held fixed in the adjustment of the LEO satellite positions. Due to its purely kinematic nature, the approach is of primary interest, whenever the dynamics does not allow an appropriate modeling, or when the computed orbits shall be fully independent of any gravitational or non-gravitational models. As a key application, kinematic POD is frequently used for deriving gravity field information from LEO satellite missions equipped with GPS/GNSS receivers. Here, the GNSS-based positions can be used as pseudo-observations in a subsequent dynamical orbit and gravity field adjustment [Beutler et al., 2010] or other alternatives such as the energy-integral approach [Gerlach et al., 2003]. Kinematic POD has first been proposed by Švehla and Rothacher [2002] and widely been employed for gravity recovery in the context of the CHAllenging Minisatellite Payload (CHAMP), Gravity Recovery And Climate Experiment (GRACE), Gravity field and steady-state Ocean Circulation Explorer (GOCE), and, most recently, Swarm missions [Švehla and Rothacher, 2005; Jäggi et al., 2011; van den IJssel et al., 2015; Freeden and Rummel, 2017]. Subject to the availability of proper GNSS orbit and clock products, a precision at the 5 cm level has been demonstrated in the above missions based on comparison with reduced-dynamic orbit solutions and/or SLR observations.

Limiting factors for the achievable performance include the quality of the GNSS orbit and clock products, and the contribution of unmodelled effects such as phase center variations, noise, multipath, and high-order ionospheric effects. These impact the positioning accuracy in direct relation to the geometric dilution of precision [GDOP; Langley, 1999], which depends on the number of tracked GNSS satellites and the distribution of their line-of-sight vectors. Kinematic POD is most challenging for receivers with a low number of tracking channels and in regions with reduced satellite visibility (polar gap) or increased tracking outages (e.g. due to scintillation in polar and equatorial regions; van den IJssel et al. [2015]).

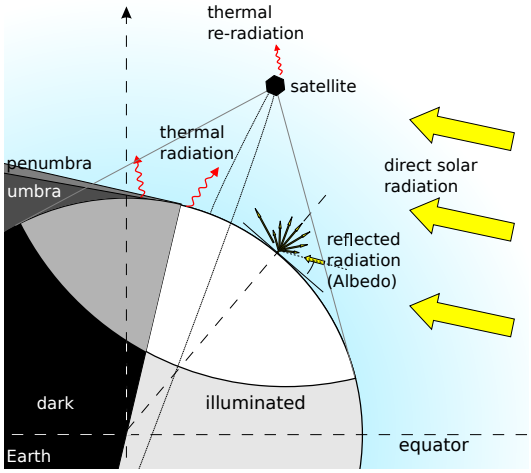

Fig. 1.1: Overview of non-gravitational forces.

Dynamic Orbit Determination Dynamic orbit determination [Vetter, 2007; Tapley et al., 2004] represents the traditional approach for satellite orbit determination using ground-based radiometric or optical observations and is originally driven by the need to reconstruct a continuous satellite orbit despite large visibility and tracking gaps. The quality of the derived orbits largely depends on the quality of the employed force models. Accordingly, a purely dynamic approach requires high-precision gravitational and non-gravitational force models [Perosanz et al., 1997] to achieve geodetic-grade orbit determination performance. Figure 1.1 shows the dominant non-gravitational force models and especially highlight considerations regarding shadow. The magnitudes of accelerations depending on the altitude of the spacecraft are show in Table 1.1. The acceleration due to solar radiation pressure is the second most dominating on low Earth orbit spacecraft like TerraSAR-X [Capderou, 2014]. Contrary to the aerodynamic accelerations,

Table 1.1: Magnitudes of gravitational and non-gravitational forces on the TerraSAR-X spacecraft.

Acceleration	Magnitude	Unit
Earth harmonic gravity field	8.40	m/s^2
Moon point mass	639.50	nm/s^2
Sun point mass	346.20	nm/s^2
Solid Earth tides	195.40	nm/s^2
Atmospheric drag	87.20	nm/s^2
Solar radiation pressure	43.30	nm/s^2
Relativity	16.30	nm/s^2
Ocean tides	12.40	nm/s^2
Pole tides	0.20	nm/s^2

which rapidly decreases with distance from the Earth's atmosphere, the solar radiation pressure influence is only present, whenever the spacecraft is illuminated.

Concerning non-gravitational contributions, detailed satellite surface models are typically required to properly account for drag and radiation-induced forces. First applications of such models for LEO POD have been demonstrated in the TOPography EXperiment [TOPEX/Poseidon; Marshall and Luthcke, 1994]. The benefit of sophisticated satellite macro models has further been highlighted in Ziebart et al. [2005].

Reduced-Dynamic Orbit Determination Given the high precision of GNSS carrier phase observations it is generally difficult to achieve a fully consistent dynamical modeling accuracy. To best combine the advantages of purely kinematic and purely dynamic methods, the reduced-dynamic orbit determination concept has been proposed by Wu et al. [1991] for GPS-based LEO POD. The reduced-dynamic approach requires a pseudo-stochastic parameterization to compensate potential deficits in the employed force models. While process noise provides a natural way of controlling the confidence in the dynamical modeling in sequential estimators [Tapley et al., 2004; Montenbruck et al., 2005], different forms of empirical parameters can be employed in a batch least squares estimation. These may include instantaneous velocity changes (impulses), piecewise constant accelerations, and piecewise linear accelerations as discussed in Jäggi et al. [2006]. By including such quantities into the set of solve-for parameters, additional degrees of freedom are introduced into the orbit determination process which allow the resulting trajectory to deviate from the given dynamical models. Irrespective of the specific parameterization, the empirical parameters are typically constrained to zero a priori values. Depending on the chosen a priori variance and the

weight of the actual measurements, different levels of stiffness may be imposed on the resulting trajectory. While tight constraints place more confidence in the dynamical model, loose constraints result in a more kinematic orbit. The choice of constraints and the total number of empirical parameters is commonly based on a "tuning" process making use of overlap comparisons, inter-agency comparisons, or external validation tests (e.g. with SLR). The incorporation of empirical constant and once-per-revolution (1/rev) accelerations into the set of estimation parameters, which has a long history in geodetic orbit determination and is naturally motivated by the characteristics of near circular orbital motion [Colombo, 1989], represents an early form of reduced-dynamic POD. However, a single set of such parameters would generally be insufficient to achieve the desired accuracy for GNSS-based LEO orbit determination. The reduced-dynamic solution directly yields a center of mass (COM) trajectory constrained by the dynamical model.

Reduced-dynamic POD nowadays represents a well established technique and is most widely applied in LEO missions requiring utmost orbit restitution accuracy. However, different levels of reduced-dynamics are employed in different software packages and by different institutions. Most notably, the packages differ in the effort to concisely model the non-gravitational forces. While tools such as GNSS-Inferred Positioning System and Orbit Analysis Simulation Software [GIPSY; Lichten, 2005], GEODYN [Pavlis et al., 2007], and Navigation Package for Earth Observation Satellites [NAPEOS; Springer, 2009] traditionally support the use of detailed macro models for the surface forces, the Bernese GNSS Software Dach et al. [2015], for example, copes without any non-gravitational force models at all. Only simple cannon-ball models were originally employed in the GNSS High Precision Orbit Determination Software Tools [GHOST; Montenbruck et al., 2005], which served as starting point for the present study.

Despite the widely different complexity and sophistication of the employed dynamical models, a high level of precision and accuracy has been achieved in all cases, thus demonstrating the capability of the reduced-dynamic concept to recover the orbit of a LEO satellite from GNSS observations. Largely consistent performances of a 3-5 cm 3-D root mean square (RMS) accuracy and down to 1 cm radial accuracy have been reported by different institutions for a wide range of missions such as GRACE, GOCE, Meteorological Operational Satellite (MetOp), Jason, and Swarm [Jäggi et al., 2007; Bock et al., 2011; Montenbruck et al., 2008; Flohrer et al., 2011; Haines et al., 2011; van den IJssel et al., 2015]. Despite the remarkable precision achieved even in a complete absence of a priori models for the non-gravitational forces, a high-level of em-

pirical parameterization remains a matter of continued concern. Aside from a possibly reduced stiffness of the resulting orbit solution, the leveling in radial and lateral (cross-track) direction depends to a large extent on the assumed dynamics. In the absence of dynamical constraints, the estimated trajectory becomes highly sensitive to uncertainties in the phase center location of the GNSS receiver antenna. However, in-flight calibrations using a residual stacking or direct estimation [Jäggi et al., 2009] cannot recover the phase center offset (but only phase center variations) unless the motion of the center-of-mass is defined through a proper dynamical model.

1.3 Structure

The thesis is separated in six chapters, which are briefly explained below. As a general guideline, this work is structured from employed principals at the beginning to the results and a final conclusion at the end.

Chapter 1 *Introduction*: the first chapter is dedicated to the motivation of this work, which includes a brief state-of-the-art summary, and the objectives of this work.

Chapter 2 *Data and Methodology*: basic information regarding selected satellite missions, the precise orbit determination concept, and the performance assessment strategy are summarized in this chapter.

Chapter 3 *Non-Gravitational Forces – Models*: important modeling aspects of the satellite macro model, the solar radiation and Earth radiation model, as well as different aerodynamic models are discussed.

Chapter 4 *Non-Gravitational Forces – Assessment*: this chapter comprises an assessment of the models, introduced in the previous chapter. The analysis includes atmospheric density comparisons, orbit determination performance metrices like empirical accelerations, and orbit quality parameters like satellite laser ranging measurements.

Chapter 5 *Ambiguity Fixing*: the methodology for GPS integer ambiguity fixing is addressed in this section. The resulting orbit quality is assessed by means of satellite laser ranging measurements, which are compared to a radar-based validation technique.

Chapter 6 *Conclusions and Recommendations*: a summary of the thesis as well as outlook and recommendations are addressed in the last chapter.

An overview of the selected satellite missions Sentinel-1A (S-1A), Swarm-C (SWC), TerraSAR-X (TSX-1), and TanDEM-X (TDX-1) as well as the research focus and validation techniques are shown in Figure 1.2. Basis notations, used throughout this thesis are as follows: vectors are denoted with bold, italic letters, like $\boldsymbol{r}$.

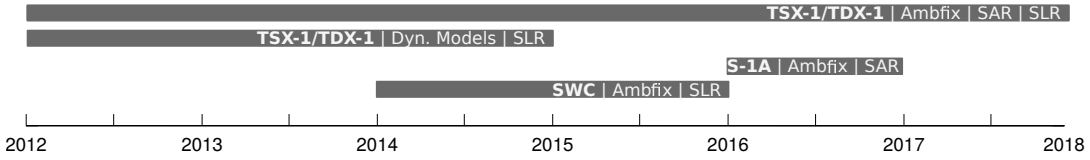

Fig. 1.2: Overview of selected satellite missions Sentinel-1A (S-1A), Swarm-C (SWC), TerraSAR-X (TSX-1), and TanDEM-X (TDX-1) including research focus and validation techniques as used in this thesis.

A list with required acronyms and their explanation is available from page 119 onwards, an index with employed Greek symbols and important variables is listed starting on page 122.

2

Data and Methodology

2.1 Satellite Missions

Four satellite missions in low Earth orbit are selected to study the influence of refined orbit modeling techniques. Within this section, the missions are briefly introduced stating the overall aim of the missions, the corresponding orbit characteristics, and a description of the spacecraft.

2.1.1 TerraSAR-X

Following the first microwave radar imaging mission European Remote Sensing Satellite 1 (ERS-1), launched on July 17, 1991 [Duchossois and Fea, 1993], the Shuttle Radar Topography Mission (SRTM), launched on February 11, 2000 [Farr et al., 2007], showed impressively the potential of the radar imaging technique, which provides global and repetitive observations, irrespective of sunlight or cloud coverage. The sustainable request for high-resolution and high-precision radar images was the initiative to develop the high-resolution X-band satellite mission TerraSAR-X [Buckreuss et al., 2003], which is the continuation of the scientifically and technologically successful radar mis-

sion SRTM. For supporting both scientific and commercial applications, the mission is realized as a public-private partnership between the Deutsches Zentrum für Luft- und Raumfahrt (DLR) and Airbus Defence and Space (Airbus DS), and was signed on March 25, 2002 as Germany's first national remote sensing satellite mission. Both parties have different responsibilities regarding the spacecraft, the orbit control, and the product policies [Werninghaus and Buckreuss, 2010].

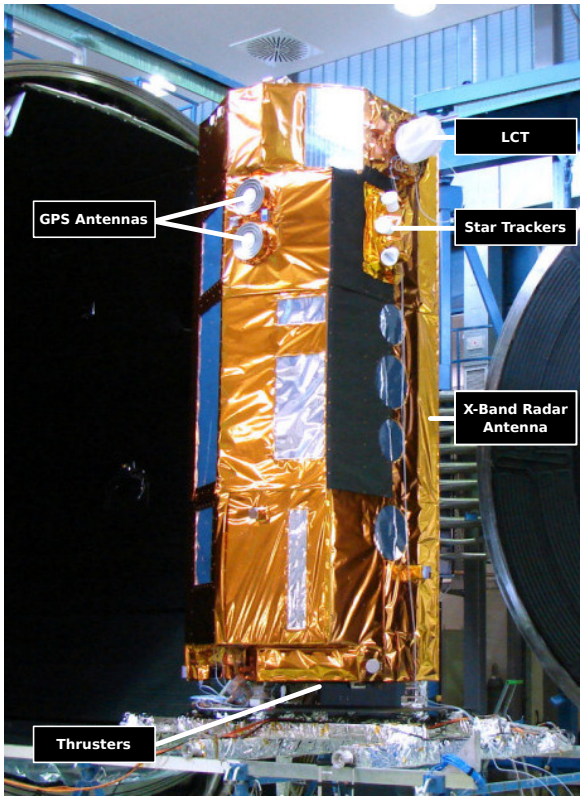

Fig. 2.1: Photo of deployed TerraSAR-X satellite, ready for vacuum chamber test. Courtesy: IABG

The Mission The satellite TSX-1, which is illustrated in Figure 2.1, was successfully launched on June 15, 2007 at 02:14:01.23 universal time coordinated (UTC) on top of a Russian Dnepr-1 rocket from Baikonour Cosmodrome, Kazakhstan [Kahle et al., 2007]. After successfully performing the launch and early orbit phase (LEOP), and the commissioning phase, the German Space Operations Center (GSOC) at DLR continues with the mission operations and the operational science orbit product generation. The spacecraft carries an advanced high-frequency multi mode SAR X-band sensor with

a center frequency of 9.65 GHz and a bandwidth of 300 MHz. The SAR instrument provides three different imaging modes Stripmap, Spotlight, and ScanSAR, which have different swath widths and resolutions. Thus, the mission provides a broad spectrum of scientific application areas reaching from cartography to oceanography [Eineder et al., 2003].

Satellite Orbit The spacecraft orbits the Earth in an altitude of 514 km on a Sun-synchronous dusk-dawn near polar orbit with an inclination of 97.44 °, being a good compromise between radar performance, revisit, and order-to-acquisition time. The ground track repeats every 11 days. Figure 2.2 shows the ground track of TerraSAR-X for one revolution of 90 minutes. Due to the chosen orbit configuration along with the terminator, the satellite is almost constantly illuminated by the Sun. As the elevation of the Sun above the orbit plane is slightly varying, short orbit passages in the Earth shadow are possible. Due to the objective of the interferometric campaigns, the strict orbit requirements for TerraSAR-X are formulated in the form of a 250 m toroidal tube around a pre-flight determined reference trajectory.

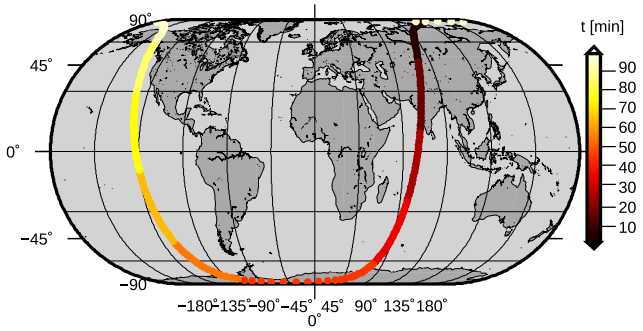

Fig. 2.2: One revolution of TerraSAR-X on DOY 170/2012.

The GSOC at the DLR in Oberpfaffenhofen, Germany, is in charge of generating the precise science orbit (PSO) products of the TerraSAR-X mission. The PSOs of TerraSAR-X are estimated in a reduced-dynamic approach with a set of consolidated models. The orbit solutions exhibit a reported 3-D accuracy of 4.2 cm, which is much better than the initially specified orbit accuracy of 20 cm [Yoon et al., 2009]. Due to the rapid development of advanced techniques in geodetic SAR imaging, the pixel geo location accuracy has been improved to approximately 1 cm in range direction [Balss et al., 2013].

Spacecraft The spacecraft was built by Airbus DS and launched with a wet mass of 1,350 kg (including fuel of 120 kg), and is characterized by a hexagonal outer shape with a total height of 5 m and a diameter of 2.4 m. Dimensions of the associated plate model are available in Table 3.1. The satellite bus carries the X-band radar instrument, the SAR antenna, which in flight attitude points 33.8 °off nadir, and the X-band downlink antenna, which is mounted on the whisk boom to avoid interferences during simultaneous radar imaging and data transmission to ground [Buckreuss et al., 2003]. Power supply is provided by solar array mounted in direction of the Sun, the deep-space looking surface is used for the laser communication terminal (LCT) and as thermal radiator [Lange and Smutny, 2007]. Star trackers for attitude determination, reaction wheels and magnetorquers for momentum unloading are utilized for determining the spacecraft's attitude with a pointing accuracy smaller than 40 arcsec [Kahle et al., 2007].

In order to enable high-precision orbit reconstruction for supporting high quality SAR images, the satellite is equipped with an integrated geodetic and occultation receiver (IGOR), which serves as main receiver for the purpose of POD, and a backup single frequency receiver MosaicGNSS [Airbus DS, 2014]. IGOR is a heritage of the BlackJack receiver [Montenbruck and Kroes, 2003], known from satellite missions like GRACE [Tapley et al., 2011] or CHAMP [Reigber et al., 2002]. The receiver tracks dual-frequency microwave GPS signals and has additional radio-occultation capabilities for atmospheric sounding. Embedded in the tracking, occultation, and ranging (TOR) project [Rothacher and Grunwaldt, 2006], the Deutsches GeoForschungsZentrum (GFZ) and the University of Texas Center for Space Research provided both the IGOR and a laser retro reflector (LRR), which is introduced later. The TerraSAR-X GPS antenna system employs a total of five antennas. Two of them are commercial-grade patch antennas Sensor Systems S67–1575–14 [Sensor Systems, 2004] (on L_1 and L_2 frequency) and connected to the IGOR, they serve for orbit determination. Two L_1 antennas are connected to the MosaicGNSS receiver, and one antenna serves for radio occultation measurements. The corresponding phase patterns are a priori known from calibration on ground.

The mentioned LRR, a precisely manufactured arrangement of four cube corner prisms, each with a vertex length of 28 mm, completes the payload of TerraSAR-X [Grunwaldt et al., 2006]. This instrument is essential for validating the satellite orbits, as is allows a direct two-way ranging between a network of SLR ground stations and the satellite. Figure 2.3 shows both the SAR antenna, as well as the SLR reflector, which are employed for orbit validation.

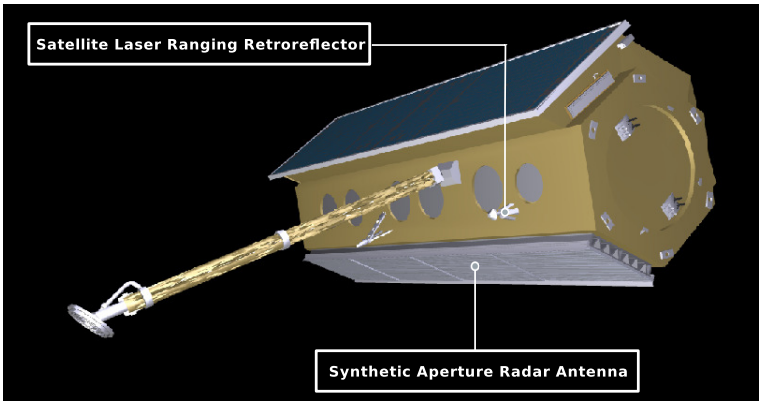

Fig. 2.3: Selected validation instruments of TerraSAR-X.

TanDEM-X On June 21, 2010, the TerraSAR-X mission was successfully complemented with launch of the satellite TDX-1. The mission is designed as an add-on for the TerraSAR-X mission, aiming at the generation of a consistent global digital elevation model (DEM), among others [Krieger et al., 2007]. The satellite is designed for a nominal lifetime of 5 years, and has a nominal overlap of TSX-1 with 3 years. The TSX-1 and the TDX-1 satellite are technically similar, with few modifications: TSX-1 carries a LCT, TDX-1 is equipped with a cold gas propellant system and is capable of receiving data from TSX-1 via inter satellite link. They orbit the Earth in a pendulum and helix formation with a baseline length, selectable between less than 2 km up to 50 km, which depends on the imaging mode [Moreira et al., 2004; Krieger et al., 2007; Fiedler and Krieger, 2004; Fiedler et al., 2005]. Identical to TSX-1, GSOC is in charge of the orbit determination.

The twin-satellites TerraSAR-X and TanDEM-X have been chosen for the present study since there is an increasing demand for accurately determined orbit solutions. Both spacecraft provide GPS observations of high quality, and required auxiliary data like the spacecraft's attitude or details on the surface description are available. Moreover, both spacecraft provide long timeseries, and support orbit validation by SLR and radar ranging.

2.1.2 Sentinel-1A

S-1A is the first satellite of the Sentinel mission within the European Earth observation program Copernicus [Aschbacher and Milagro-Perez, 2012; Attema et al., 2012; Torres et al., 2012]. The spacecraft was successfully launched on April 3, 2014 from Korou, French Guiana. The satellite is equipped with C-Band SAR, three star trackers for attitude determination, and two 8-channel GPS units to support POD. The GPS observation unit is provided by RüstungsUnternehmen-AktienGesellschaft (RUAG) Space. The 8-channel receivers are in principle the same as on the Swarm satellites, introduced in the next section [Zangerl et al., 2014]. Compared to Swarm, the antennas are equipped with a new patch excited cup (PEC) element and two choke rings [Óhgren et al., 2011].

Fig. 2.4: Artist's view of the Sentinel-1A spacecraft, indicating selected equipment. Courtesy: ESA

Due to the lack of a laser retro reflector, orbit validation with satellite laser ranging is not possible. Within the established Copernicus POD (CPOD) service, several agencies compute orbit solutions of S-1A, which are compared to the official Global Monitoring for Environment and Security (GMES) solutions [GMES Sentinel-1-Team, 2012; Fernandez and Femenias, 2014; Peter et al., 2017]. The requirement for the orbit accuracy is given to be better than 5 cm.

The spacecraft is orbiting the Earth on a near-polar, Sun-synchronous orbit with a 12 day repeat cycle in a height of 693 km and an inclination of 98.18°. For interferometry,

the main purpose of the radar system, the spacecraft requires stringent orbit control for positioning and synchronization of the interferometric pairs. Therefore, the orbit is defined in an Earth-fixed orbital tube with a 50 m RMS radius around the nominal path. For most of it's lifetime, the spacecraft shall stay within this tube.

The satellite, illustrated by Figure 2.4 has been built by Thales Alenia Space and Airbus DS. It is based on the Piattaforma Riconfigurabile Italiana Multi-Applicativa (PRIMA) platform. The main satellite bus is supplemented with two large solar arrays, capable of producing 5,900 W, and the SAR antenna. Detailed dimensions of the 2,300 kg spacecraft are indicated by Table 3.2. Studies on the spacecraft's thermal budget, are available in Perellón et al. [2015].

S-1A has been selected for the purpose of demonstrating the effect of the GPS ambiguity fixing technique. Due to the SAR instrument, orbit validation is supported by radar range measurements. Data used within this study have kindly been provided by the Sentinel Quality Working Group, whereas science orbit products are computed by Grupo Mecánica del Vuelo (GMV), Spain.

2.1.3 Swarm-C

The Earth's magnetic field plays an important role for understanding the processes in the Earth's interior. In 1979, the satellite Magnetic Field Satellite (MagSat) was launched to first obtain a quantitative survey of the Earth's magnetic field from outer space [NASA, 2000]. With the launch of CHAMP and Satélite de Aplicaciones Científicas-C (SAC-C) in 2000, geomagnetic data have been delivered to the scientific community for 13 years. The Swarm satellite mission aims at studying the Earth's magnetic field as the 5th Earth Explorer Programme of the European Space Agency (ESA). As a secondary objective of the Swarm mission is dedicated to measure the Earth's gravity field [Friis-Christensen et al., 2008].

Three identical satellites were launched on November 22, 2013 at 12:02:29 UTC onboard a Rockot rocket from Plesetsk Cosmodrome Site, Russia. Swarm-A and -C fly side-by side in a near polar, circular orbit in an altitude of 450 km and an inclination of 87.4 °. The third satellite Swarm-B complements the constellation in a circular orbit with an altitude of 530 km and 86.6 ° inclination. Figure 2.5 shows one satellite of the Swarm constellation.

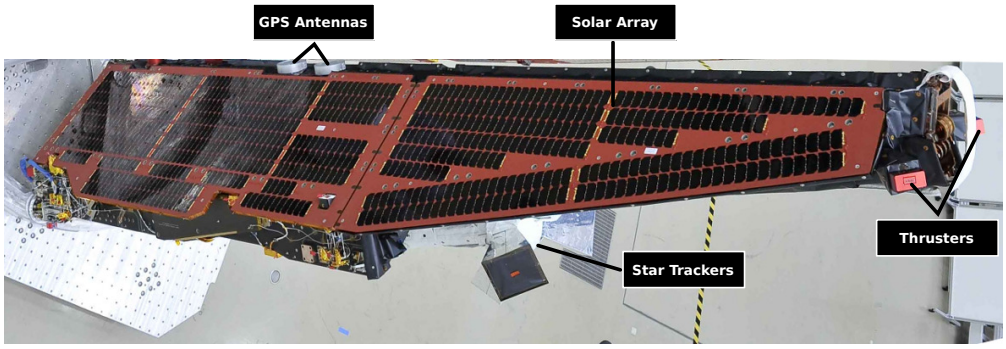

Fig. 2.5: Artist's illustration of one Swarm satellite in deployed configuration, indicating selected equipment. Courtesy: Airbus DS

The spacecraft, each with a wet launch mass of 473 kg, were manufactured by Airbus DS. The total satellite length of 9.1 m includes a deployable boom of 4 m, the satellite body is 1.5 m wide and 0.85 m high [Zangerl et al., 2014]. The core instruments of each satellite are vector and scalar magnetometers to measure the Earth's magnetic field and equipment for measuring the Earth's electric field. Accelerometers have been placed onboard to measure the non-gravitational accelerations. For providing a precise orbit determination, the satellites are equipped with 8-channel dual-frequency GPS receivers, supplied by RUAG Space [Zangerl et al., 2014; Sust et al., 2014]. These receivers are also employed to measure the Earth's gravity field. The orbit validation is provided by SLR reflectors. PSOs products of the Swarm mission are operationally generated at Faculty of Aerospace Engineering at Delft University of Technology [van den IJssel et al., 2015].

The spacecraft Swarm-C is selected for assessing the impact of solar radiation pressure, Earth radiation pressure, aerodynamics, and ambiguity fixing. Operational orbit solutions have been kindly provided by TU Delft.

2.2 Precise Orbit Determination Concept

As stated in the introduction, orbit determination requires availability of different models. Applied models and key parameters of the orbit determination setup are introduced in this section as a starting point for subsequent model enhancements.

2.2.1 Generic Models

The applied reduced-dynamic orbit determination relies on both the quality of the GPS observations, and the underlaying dynamical models, which describe a multitude of accelerations of gravitational and non-gravitational nature, acting on the spacecraft. The present study builds on the GNSS High Precision Orbit Determination Software Tools (GHOST), which have been developed at DLR/GSOC [Montenbruck et al., 2005; Wermuth et al., 2010]. The basic set of employed key models and estimated parameters is shown in Table 2.1, which covers the measurement model, the dynamical model, and, finally, the reduced-dynamic setup. Starting from a basic set of selected dynamical models as applied in the operational precise science orbit generation, the model sophistication is continuously increased within this study and the impact of these modifications on the orbit solutions is analyzed.

For the TerraSAR-X mission, the measurement model is adopted without any significant modifications from the PSO processing and based upon L_1 and L_2 code and phase measurements. The observations are combined in an ionosphere-free (first order) linear combination. GPS satellite antenna phase center offset (PCO) and phase center variation (PCV) corrections are obtained from the igs08.atx [Schmid et al., 2016] and igs14.atx [Rebischung and Schmid, 2016, from January 2017 onwards] of the International GNSS Service (IGS). TerraSAR-X GPS antenna PCOs corrections are calibrated on-ground [Montenbruck et al., 2009], whereas the corresponding PCV corrections are adjusted from PSO carrier phase residuals. The required GPS orbit and high-rate (30 s) clock offset products (finals) are obtained from the Center for Orbit Determination in Europe (CODE) [Dach et al., 2009; Bock et al., 2009]. GPS carrier phase wind up is taken into account according to Wu et al. [1993]. The attitude is measured by the onboard star trackers and provided in intervals of 10 s [Kahle et al., 2007].

Besides the measurement model described above, reduced-dynamic orbit determination requires gravitational and non-gravitational models. The gravity field is modeled by

Table 2.1: Overview of selected key models, and reduced-dynamic orbit parameterization.

Quantity	PSO	Enhanced
Measurement Model:		
GPS measurements	GPS ionosphere-free L_1 and L_2 pseudo range and carrier phase at 30 s intervals	
GPS satellite PCOs+PCVs	igs08.atx [Schmid et al., 2016], igs14.atx [Rebischung and Schmid, 2016]	
GPS orbits and clocks	Final CODE products at 30 s sampling [Dach et al., 2009]	
LEO satellite GPS antenna PCOs	On-ground calibrated for TSX-1 and TDX-1, none for S-1A and SWC	
LEO satellite GPS antenna PCVs	In-flight calibrated	
Phase wind up	Wu et al. [1993]	
Relativity	Shapiro effect [Kutschera and Zajiczek, 2010]	
Spacecraft attitude	Quaternions, provided by onboard star trackers (10 s)	
Dynamical Model:		
Gravity models	GGM01S [Tapley et al., 2003]	GOCO03s [Mayer-Gürr et al., 2012]
	100×100	120×120
Ocean Tides	CSR/Topex3.0 [Eanes and Bettadpur, 1995]	FES2004 [Lyard et al., 2006]
Perturb. Sun/Moon	Analytical series of luni-solar coordinates	
Solid Earth tides	IERS2003 [McCarthy and Petit, 2003]	
Solid Earth pole and ocean pole tides	IERS2003 [McCarthy and Petit, 2003]	
Solar radiation pressure	cannon-ball	macro-model (see Sect. 3.2.1)
Earth radiation pressure		macro-model (see Sect. 3.2.2)
Solar proxies and indices	NOAA/SWPC solar flux and geomagnetic activity data	
Aerodynamics	cannon-ball, drag	macro-model, drag and lift (see Sect. 3.3)
Atmospheric density	Jacchia-71G [Gill, 1996]	DTM 2012 [Bruinsma et al., 2012]
		NRLMSISE-00 [Picone et al., 2002]
Atmospheric wind		HWM-07 [Drob et al., 2008]
Reference Frames Transformation:		
Conventions	IERS1996 [McCarthy, 1996]	
EOPs	IGS finals	
Reduced-Dynamic setup:		
Empirical Accelerations	One set of constant accelerations in radial (R), along-track (T) and normal (N) direction per 10 min interval	
A priori sigma	5 nm/s^2 in R and 15 nm/s^2 in T and N direction	
Non-gravitational scaling parameters	One per orbit arch for drag, and solar radiation	+ Earth radiation
Iterations	3	
Numerical integrator	variable order and stepsize multistep method [Shampine and Gordon, 1975]	

the GRACE Gravity Model 01S [GGM01S; Tapley et al., 2003] up to degree and oder 100 or the Gravity Observation COmbination 03s [GOCO03s; Mayer-Gürr et al., 2012] up to degree and order 120. Gravity field time variability is considered by a linear drift of the gravity field coefficients $\dot{C}_{20}$, $\dot{C}_{21}$, and $\dot{S}_{21}$. Further variations, e.g. annual or semi-annual are not treated. According to Couhert et al. [2015], these variations could exhibit a radial error of approximately 2 mm in case of Jason-1. Center for Space Research (CSR)/Topex 3.0 [Eanes and Bettadpur, 1995] and Finite Element Solution 2004 [FES2004; Lyard et al., 2006] serve as ocean tide models, both are based on measurements from the Topex/Poseidon (T/P) mission. Third body gravitational perturbations from the position of the Sun and the Moon are provided by an analytical series of luni-solar coordinates. General relativity is primarily considered by the acceleration due to the Shapiro effect [Kutschera and Zajiczek, 2010]. The accelerations due to Lense-Thirring and Geodesic Precession are orders of magnitudes smaller and were, therefore, neglected [Ries et al., 2003].

The considered non-gravitational accelerations comprise the aerodynamic, the solar radiation pressure, and the Earth radiation pressure accelerations (cf. Chapter 3). All of these non-gravitational accelerations originate from surface forces and their modeling requires proper knowledge of the satellite geometry and material properties. While the operational science orbits treat the surface as a simplified sphere, the present study assesses the impact of a macro or plate model in combination with the non-gravitational accelerations. Details on the selected models are provided in Section 3.1.

Reference frames transformations are based on the International Earth Rotation and Reference Systems Service (IERS) 1996 [McCarthy, 1996] conventions. The required Earth orientation parameters (EOPs) are provided by the IGS [Kouba and Mireault, 1998].

In accordance with the PSOs, the orbit arcs of 30 h are centered at noon, which allows an overlap of 6 h between two consecutive arcs. Therefore, the resulting orbit solutions exhibit smooth transitions at midnight and the orbit transitions at day boundaries allow validating the internal orbit consistency (cf. Section 2.3.2). The variable order and variable stepsize multistep integrator described by Shampine and Gordon [1975] serves as numerical integrator. For given models of the acceleration as a function of time t, position $\boldsymbol{r}$, and velocity $\boldsymbol{v}$, the motion of a satellite can be obtained from given initial conditions using a step-wise numerical integration.

The reduced-dynamic approach is iterated three times, where the results clearly converge. Maneuvers, which are required for formation control of the TSX-1/TDX-1 space-

craft, are considered by their start time and burn duration in radial, tangential, and normal direction [Yoon et al., 2009].

2.2.2 Empirical Parameters

To compensate any deficiencies in the employed dynamical models, piecewise constant empirical accelerations are estimated in radial, tangential, and normal (RTN) direction in intervals of 10 minutes. The amplitudes of these accelerations are not known beforehand. Thus, the applied a priori constraints are based on a tuning process of the empirical accelerations and kept at 5 nm/s^2 in radial, and 15 nm/s^2 in tangential, and normal direction for ease of comparison. Herein, a reduction of the 10 min interval would not significantly improve the orbit quality, but increase the processing time. Increasing this time interval is linked to a loss of orbit quality, since it depends on the orbit height of the spacecraft and the resulting impact of the accelerations. A proper understanding of the empirical accelerations is of vital importance. In general, tight constraints on the empirical accelerations puts high trust in the employed dynamical models. Vice versa, loose constraints put more trust on the employed kinematic observations. In addition, individual scaling parameters for the non-gravitational models of aerodynamics, solar radiation pressure, and Earth radiation pressure are introduced (a detailed description is following in the model section). Since the estimation parameter is directly connected to the acceleration model, the coefficients are used for assessing model impacts in the orbit solutions.

2.2.3 Antenna Phase Center Offsets and Variations

In GPS-based LEO POD, a precise modeling of phase center offsets and variation of the satellite receiver GPS antenna is mandatory [Jäggi et al., 2009]. According to Teunissen and Kleusberg [1998], computation of the geometric distance between the antenna phase location of the GPS satellite at signal emission time and the antenna phase center location of the receiving antenna at signal reception time is required for modeling GPS observations.

The antennas of satellite missions are first calibrated on ground, whereas the (post) in-flight calibration is essential for precise orbit determination [Montenbruck et al., 2009]. Generally, the PCOs correspond to the difference between the mean center of the wave

front and the antenna reference point (ARP), whereas phase variations are direction-dependent distortions of the wave front. In this system, the ARP is the only mechanical point.

Due to distortions, induced by the asymmetric antenna geometry and due to the influence of the supporting structure, the real wave front does not correspond to a spherical wavefront with a common center. The deviations can be described by

$$\zeta_{\mathrm{PCO/PCV}} = e^{\mathrm{T}}\left(\boldsymbol{r}_{\mathrm{PCO,sat}} - \boldsymbol{r}_{\mathrm{PCO,rcv}}\right) + \left(\zeta_{\mathrm{PCV,sat}}(-\boldsymbol{e}) + \zeta_{\mathrm{PCV,rcv}}(\boldsymbol{e})\right) \quad . \tag{2.1}$$

Herein, $\boldsymbol{e}$ denotes to the receiver-to-satellite unit vector, $\boldsymbol{r}$ is the PCO vector, and ζ denotes the direction-dependent PCV of the receiver and satellite antenna [Teunissen and Montenbruck, 2017, Chapters 17, 19]. Phase center variations for the transmitting antennas of the GNSS satellites are provided by the IGS in the antenna exchange (ANTEX) format [Schmid et al., 2016]. The receiver antennas were first calibrated on ground [Montenbruck et al., 2009]. Within this thesis, the LEO GPS phase maps are estimated in an iterative residuals stacking process [Jäggi et al., 2009]. Based on carrier phase residuals stemming from the reduced-dynamic orbit determination, the phase center variations are estimated from these residuals, and then utilized as a priori phase center variation map during the next iteration. This procedure is illustrated in Figure 2.6. Within the present approach, daily carrier phase residual files of at least one week are iteratively employed for phase pattern estimation. Typically, three iterations are required. Details on phase pattern estimation are available e.g. in Jäggi et al. [2009].

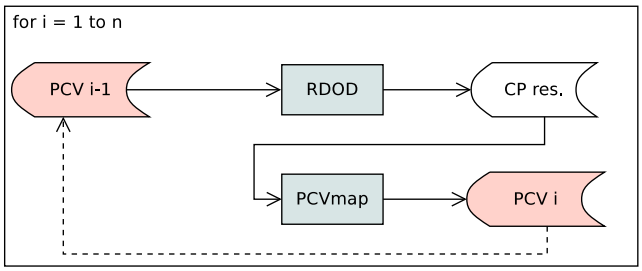

Fig. 2.6: Illustration of phase pattern estimation utilizing the Reduced-Dynamic Orbit Determination (RDOD), and Phase Pattern estimation (PCVmap) tool.

2.2.4 Ionospheric Delay

The ionosphere is a neutral ionized gas, which principally consists of free electrons, ions, and neutral atoms or molecules. The ionosphere is part of the Earth's atmosphere between 60 km and 1,000 km, the region includes the thermosphere, and parts of the mesosphere and exosphere. Especially the expansion in lower atmophere layers depends on the illuminaiton by the Sun [Bychkov et al., 2014]. The highly dynamical plasma density characterizes the ionosphere, which is rather difficult to model. The radio-wave propagation through the ionosphere is well documented, e.g. by Budden [1985]. The ionospheric impact on GPS observations causes a signal delay due to the electron content of the atmosphere. Magnitudes can be up to several tens of nanoseconds. During electromagnetic storms, the influence is even larger [Bychkov et al., 2014].

First order ionospheric effects are, however, eliminated by the ionosphere-free linear combination (Sect. 5.1), which removes effects that are proportional to $1/f^2$ [Hofmann-Wellenhof et al., 2008]. Dual-frequency GPS observations allow to eliminate the first order ionospheric group delay, which is in the order of up to several meter, depending on the ionospheric condition, the solar cycle, the satellite elevation, and the local time. Whereas first order effects are completely removed by the ionosphere-free linear combination (cf. Equation 5.3), the higher order effects are not eliminated [Bassiri and Hajj, 1993].

While the first-order terms simply depend on the electron content along the ray path, higher-order ionospheric effects depend on coupling between the electron density along the line of sight, and the Earth magnetic field. The magnitude of the second order effects is up to 2 cm [Hoque and Jakowski, 2007]. A couple of studies discusses the impact of ionospheric effects on GPS measurements and products [Fritsche et al., 2005; Steigenberger et al., 2006].

According to Bassiri and Hajj [1993], the pseudorange and carrier phase equations read

$$\begin{aligned} p_i &= \varrho + \frac{q}{f_i^2} + \frac{s}{f^3} \\ \varphi_i &= \varrho + \lambda_i N_i - \frac{q}{f_i^2} - \frac{1}{2}\frac{s}{f_i^3} \end{aligned} \tag{2.2}$$

with i = 1,2 denotes either GPS L_1 or L_2 frequency. Herein, q and s are computed via

$$\begin{aligned} q &= 40.3 \times \mathrm{TEC} \\ s &= 7527c \int NB_0 \cos\vartheta_B dL \quad , \end{aligned} \tag{2.3}$$

where ϑ_B is the angle between the Earth's magnetic field and the direction of signal propagation, c is the speed of light in vacuum, normal/cross-track (N) the number density of electrons, and total electron content (TEC).

Since the model depends on tracing of the magneto-ionic interactions along the signal path between receiver and transmitter, knowledge of the magnitude and direction of the geomagnetic field is required. For this purpose, the International Geomagnetic Reference Field 12 (IGRF-12) model has been selected [Thébault et al., 2015]. A detailed explanation of the applied model is available in Kedar et al. [2003] and Bassiri and Hajj [1993]. The TEC is computed using GPS pseurorange and differential code biases [Teunissen and Montenbruck, 2017, Chapter 39].

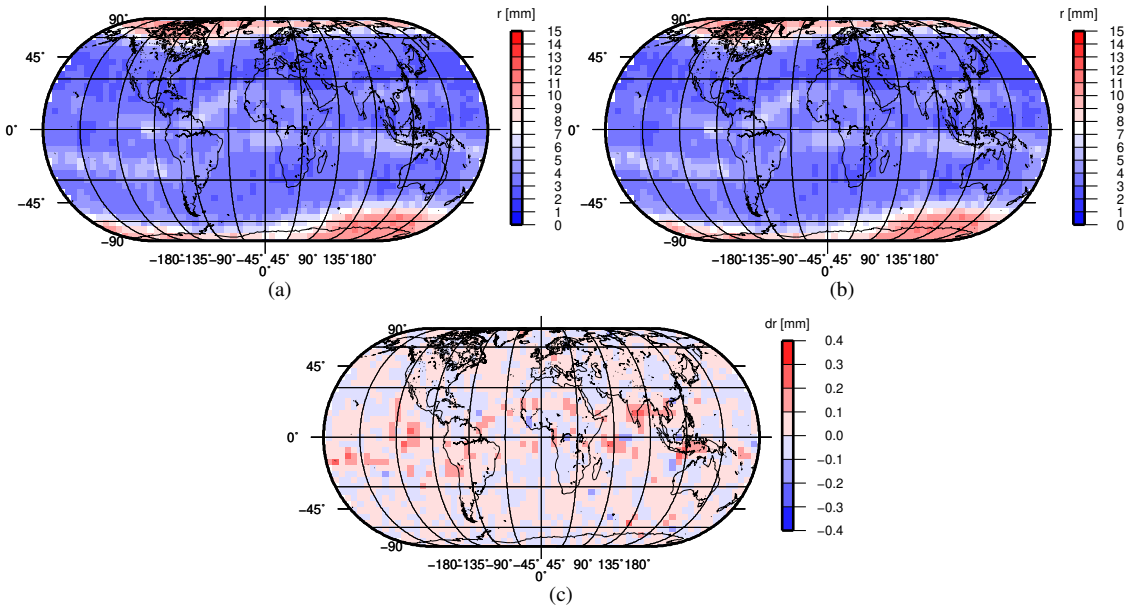

Fig. 2.7: RMS of carrier phase residuals per bin (a) with 1st order (b) 1st+2nd order correction, and (c) difference (b) – (a). DOYs 305 to 365/14; Swarm-C.

For assessing the influence of second order ionospheric correction, GPS observations of Swarm-C were selected within the period of days of year (DOYs) 305 to 365/2014 at

high solar activity. Reduced-dynamic orbit solutions were computed with first and first plus second order corrections, the obtained solutions were then compared.

Figure 2.7 shows the resulting carrier phase residuals with applied first and first plus second order ionospheric corrections. RMS of the daily residuals are gridded and averaged in quadratic bins of 5 °. The figure exhibits clearly small carrier phase residuals of up to 7 mm along the equator and at mid latitudes, and a pronounced magnitude up to 15 mm at the pole caps, where charged particles can easily pass the magnetic field. Considering second order ionospheric corrections does not cause any significant changes. The difference map between both corrections shows the impact of the applied second order term, compared to the first one. Herein, differences along the geomagnetic belt become visible, but with a maximum amplitude of 0.5 mm only.

The mean orbit difference of 0.4 mm, computed by direct orbit comparison, is fairly below 1 mm in all three directions. The values have been derived by a direct ephemeris comparison of one solution with first, and one with first and second order ionospheric corrections. In addition, also the empirical accelerations do not show any change. Due to the small magnitude and the relevance for the scope of this thesis, the second order ionospheric corrections are not applied for further tests or orbit solutions.

2.3 Performance Assessment Strategy

Within this chapter, different orbit quality indicators are introduced, which are essential for a proper orbit quality assessment. Following the reduced-dynamic orbit determination (RDOD) internal quality indicators like empirical accelerations and scaling parameters, the focus is on satellite laser ranging and the radar technique as external quality parameters.

2.3.1 Empirical Accelerations and Scaling Parameters

Both, empirical accelerations and scaling parameters are direct performance indicators of the reduced-dynamic orbit determination. The accelerations are a measure of potentially mis-modeled effects. Detailed analysis of this accelerations may hint to deficits in the employed modeling approach (eg. 1-per-rev influences). In addition, a priori

constraints on the empirical accelerations are applied. They define the weight of the dynamical models (trust).

Secondly, the non-gravitational force models include a scaling parameter, i.e. C_D for atmospheric accelerations, C_E for Earth, and C_R for solar radiation pressure. The scaling parameters are estimated in the RDOD iterations. A factor larger than one indicates that the modeled acceleration is too small, and vice versa. In case of aerodynamic accelerations, this could indicate that the cross sectional area for drag computation is too small. In addition, a time-variability hints to effects that are not captured by the models.

2.3.2 Orbit Transitions at Day Boundaries

The internal orbit consistency is evaluated by means of 3-D orbit discontinuities at day boundaries, which is the direct comparison of positions from different orbit solutions. As can be seen by Figure 2.8, the orbit positions at day i are compared to the corre-

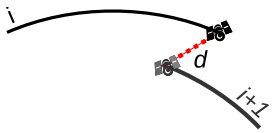

Fig. 2.8: Orbit transitions at day boundaries.

sponding orbit position at day $i+1$. Finally, the discontinuities d at day boundaries are computed via

$$d = \sqrt{(x_{i+1} - x_i)^2 + (y_{i+1} - y_i)^2 + (z_{i+1} - z_i)^2} \quad . \tag{2.4}$$

For the present study, the discontinuities are computed at 24:00, or, respectively, 00:00 UTC.

2.3.3 Satellite Laser Ranging

Satellite laser ranging is a well-established technique for validating orbit solutions. The SLR measurements are utilized as an external validation technique by comparing the ranges from SLR indicated by r_{SLR} with those, derived from the reduced-dynamic orbit solutions r_{POD}:

$$\Delta r = r_{SLR} - r_{POD} \quad . \tag{2.5}$$

Basically, satellite laser ranging requires a laser reflector on the spacecraft, as well as laser ranging stations on ground, capable of tracking spacecraft. The coordinates of the laser reflector, as well as the laser station need to be known very precisely. It is essential to note, that the spacecraft's attitude needs to be known to transform the LRR-COM offset from the spacecraft system to the inertial reference system, which is required to compute the range.

The optical SLR observations are independent of the microwave GPS observations [Pavlis and Beard, 1996; Urschl et al., 2005]. The satellite is tracked by SLR stations from the International Laser Ranging Service (ILRS) network [Pearlman et al., 2002], which tracks numerous targets with a dedicated tracking priority. TSX-1,and TDX-1 are ranking at position 3 and 4, SWC is at position 16 [International Laser Ranging Service, 2017a]. The SLR measurements consist of normal points (NPs), a sequence of individual laser measurements averaged in a time interval of 5 seconds [International Laser Ranging Service, 2015] for low Earth orbiters. For this analysis, periods between January 2012 until December 2017 were chosen. Such long-term analyses require reliable tracking stations that are available over the whole analysis period. The chosen configuration of 11 ILRS stations is shown in Fig. 2.9.

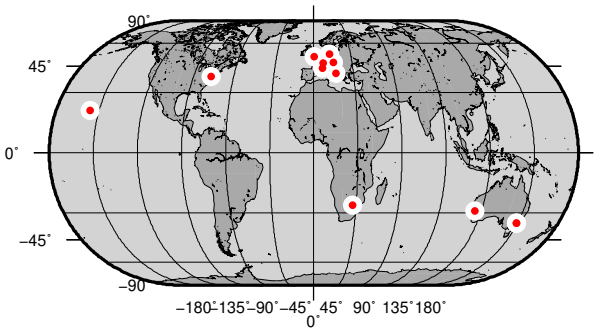

Fig. 2.9: Selected satellite laser ranging stations of the ILRS tracking network.

The setup of the SLR validation is kept fixed for all following orbit validations and only observations above 10 ° elevation the horizon are considered. Especially altimetry missions often apply high elevation masks of 60 ° or higher. At these high elevations, the SLR data provides a direct measure of the radial orbit error [Cerri et al., 2010]. Such analysis clearly strengthens the radial component, and results in small residuals. Within the present study, a conservative angle has been chosen, whereas the SLR-based position offsets, introduced later in this section, allow a detailed analysis of direction-dependent systematics[Hackel et al., 2017]. The applied threshold for SLR residuals screening is

Table 2.2: Different ocean loading models and results of TerraSAR-X orbit validation, period 2012–2015.

Model	$\bar{x}$,σ_x [mm]	Reference
FES2004	1.7 ± 12.7	[Lyard et al., 2006]
GOT00.2	1.7 ± 12.7	[Ray, 1999]
GOT4.8	1.7 ± 12.7	[Ray, 1999, updated]
EOT11a	1.7 ± 12.7	[Savcenko et al., 2012]

kept fixed at 6 cm. Compared to results obtained by 15 cm screening level, less than one percent of observations are neglected, without any significant change in the resulting residuals. Required station coordinates are taken from Satellite Laser Ranging Frame 2014 [SLRF2014; Pavlis, 2009; International Laser Ranging Service, 2017b], ocean loading is considered by Finite Element Solution 2004 [FES2004; Lyard et al., 2006].

Since the effect of ocean loading plays an important role for the derived results, a variety of well-established ocean tide models have been tested [Stammer et al., 2014; Shum et al., 1997]. The utilization of other ocean tide models, i.e. Goddard Ocean Tide model 00.2 [GOT00.2; Ray, 1999], Goddard Ocean Tide model 4.8 [GOT4.8; Ray, 1999, updated], and Empirical Ocean Tide model 11a [EOT11a; Savcenko et al., 2012] has been analyzed by a time series from 2012–2014, but did not show any significant influence on the SLR analysis, compared to the selected Finite Element Solution 2004 (FES2004). Results are summarized in Table 2.2 by means of TerraSAR-X SLR residuals, obtained from the 2012–2015 period.

The LRR range correction is considered as a function of azimuth and nadir angle and takes into account the difference between the station distance from the LRR reference point and the actual signal path within the LRR [Arnold et al., 2018a]. For the TSX-1, TDX-1, and SWC, the phase center range correction is provided by the GFZ [Neubert et al., 1998]. The Sentinel-3A LRR range correction is available in Montenbruck and Neubert [2011].

The number of normal points within one tracking pass, i.e. the passage where the instrument on ground follows and tracks the spacecraft, may vary from satellite pass to pass. For TSX-1, on average 15 NPs are collected during one tracking pass, which corresponds to an average tracking length of 75 sec. The tracking length is also explained by the switch between TSX-1 and TDX-1, which is performed by many stations during one pass. Within the 2012–2017 period, which is covered by the analysis in Section 5.3, the spacecraft TSX-1 was tracked by 34 different ILRS stations, yielding a wide range

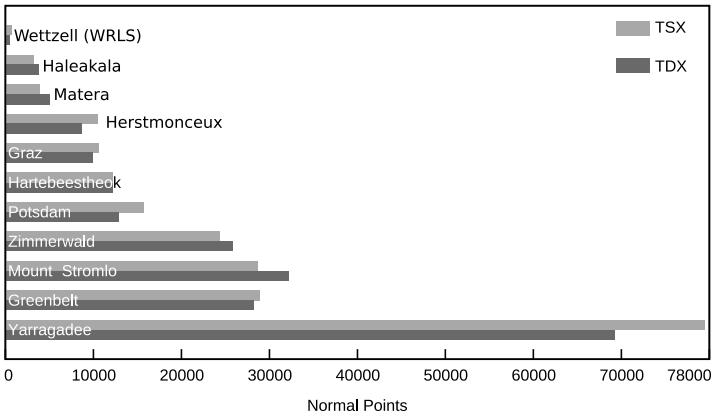

Fig. 2.10: Number of accepted normal points for selected ILRS stations between 2012 and 2017.

from only 5 to up to 75,000 normal points per station. Considering the 11 stations, a total of 206,401 normal points is available for TSX-1 within the 6 years (cf. Figure 2.10). Applying an elevation cutoff-angle of 10 °, and a threshold of 6 cm for the residuals, this leads to a total of 204,667 NPs, which are employed within this study. This corresponds to a screening rate of $0.84\,\%$. For the spacecraft TDX-1, the number of accepted normal points used throughout this analysis amounts to 195,506. Despite the higher ranking of TDX-1, the number of available normal points during the analysis period is slightly larger for TSX-1. This is related to the fact that TanDEM-X performs more maneuvers than TerraSAR-X, and that SLR tracking is not possible during maneuvers.

While SLR residuals provide an overall quality indicator for the assessment of the GPS-based orbit solutions, they ignore the information content provided in the variation of the residuals across individual tracking passes. A different analysis concept has therefore been applied to obtain further information on systematic orbit errors from the SLR measurements. Such systematic errors may, for example, arise from antenna offset errors, radiation pressure modeling errors, etc. and can be described by constant offsets $\Delta r_{\mathrm{R,T,N}}$ in radial (R), tangential/along-track (T), and normal/cross-track (N) direction. The offset between the SLR orbit, and and the GPS-based orbit solution can thus be modeled as

$$\Delta \boldsymbol{r} = \boldsymbol{e}_{\mathrm{R}} \cdot \Delta r_{\mathrm{R}} + \boldsymbol{e}_{\mathrm{T}} \cdot \Delta r_{\mathrm{T}} + \boldsymbol{e}_{\mathrm{N}} \cdot \Delta r_{\mathrm{N}} \quad , \tag{2.6}$$

where $\boldsymbol{e}_{\mathrm{R,T,N}}$ denote the unit vectors in R, T, and N direction (see Figure 2.11). This difference gives rise to a correction $\Delta\rho_{\mathrm{SLR}} = \boldsymbol{e} \cdot \Delta\boldsymbol{r}$ of the modeled SLR observations, where

$$\boldsymbol{e} = \frac{\boldsymbol{r}_{\mathrm{SLR}}}{\|\boldsymbol{r}_{\mathrm{SLR}}\|} \tag{2.7}$$

denotes the line-of-sight vector. It is thus possible to estimate the offsets $r_{\mathrm{R,T,N}}$ from SLR observations over an extended data interval using a least squares approach. For the TerraSAR-X mission, data intervals of one month have been selected. Within these intervals, the RTN position offsets are assumed to be constant while at the same time a sufficient number of observations and tracking passes is available.

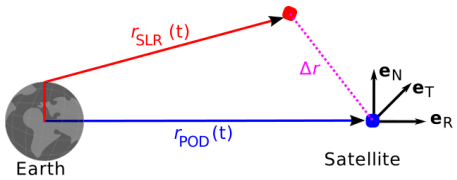

Fig. 2.11: Utilization of SLR for estimating position corrections by comparing the SLR-derived position r_{SLR} with those from the RD orbits r_{POD}.

Contrary to the pure SLR residuals, the obtained SLR-derived position offsets are sensitive in radial, tangential, and normal direction. An analysis, therefore, provides clear indicators of the orbit stability in different directions.

2.3.4 Radar Ranging

The spacecraft TSX-1, TDX-1, and S-1A are equipped with a synthetic aperture radar, which allows deriving detailed information on the ground below, e.g. by synthetic aperture radar interferometry [Bamler and Hartl, 1998]. Basically, the radar systems provide the two-way travel time of the radar pulses from the radar transmitter to ground, and back. Based on the vacuum velocity of light, the travel time can be expressed as geometric distance, but electrons in the ionosphere, dry air and water vapour as well as other corrections have to be taken into account. Radar ranging measurements to a corner cube reflector (CCR), which results in a sharp backscatter of the radar impulse, allow the determination of a bias in azimuth (in flight direction) and range (cross direction; cf. Figure 2.13) except of a time-invariant offset (internal time delay of the SAR instrument, which is subject to the instrument calibration). This requires knowledge of the satellite and the corner cube position in a common reference frame.

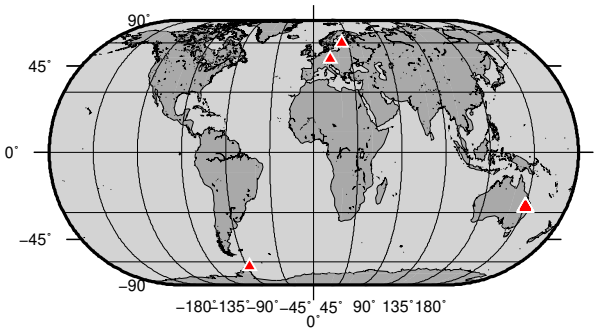

Fig. 2.12: Network of corner cube reflectors.

Range-Doppler equations in zero-Doppler geometry [Cumming and Wong, 2005] are used for validation. These relate the satellite trajectory, given by the time-dependent position vector $\boldsymbol{X}_\mathrm{s}$ and velocity vector $\dot{\boldsymbol{X}}_\mathrm{s}$, and the reflector position vector $\boldsymbol{X}_\mathrm{r}$ with the observed radar times t and τ, also referred to as slow time and fast time or azimuth and range, respectively.

$$\tau = 2/c \cdot |\boldsymbol{X}_s(t) - \boldsymbol{X}_r| \tag{2.8}$$

$$0 = \frac{\dot{\boldsymbol{X}}_s(t) \cdot (\boldsymbol{X}_s(t) - \boldsymbol{X}_r)}{\left|\dot{\boldsymbol{X}}_s(t)\right| \cdot |\boldsymbol{X}_s(t) - \boldsymbol{X}_r|} \tag{2.9}$$

The conversion of geometrical distance for the τ uses the speed of light in vacuum c. The slow time t is linked to the satellite trajectory and can be resolved by interpolating a given orbit solution and performing an iterative search for the instant of Doppler-zero using the Equation 2.9. Subsequently, the corresponding round trip time τ is derived from Equation 2.8. From a geometrical point of view, the combination of the Equations 2.8 and 2.9 models a circle located at the satellite's zero-Doppler position and oriented according to the zero-Doppler plane, and which intersects with the reflector position on ground. For details the reader is referred to Hackel et al. [2018].

Primarily intended for SAR validation purposes, a network of CCRs has been built-up by DLR/Technische Universität München (TUM) since 2011, starting with a reflector at Wettzell (WTZ), Germany. In 2013, the network was complemented with the reflectors at the German Antarctic Receiving Station (GARS) O'Higgins (OHG), Antarctica, Metsähovi (MET), Finland, and a second reflector in Wettzell. The network has been established by the Institute of Remote Sensing at DLR, in cooperation with local station providers [Balss et al., 2012]. The stated stations are selected for validating the orbit so-

lutions of TSX-1 and TDX-1, and shown in Figure 2.12. In addition and especially with focus on S-1A, the network is extended by measurements to 6 corner cubes, located in Australia, and operated by Geoscience Australia [Garthwaite et al., 2015; Garthwaite, 2017]. Within this study, the corner cubes in Australia are solely utilized for validating the orbit solutions of Sentinel-1A, since the spacecraft does not support any external validation technique like SLR [Peter et al., 2017].

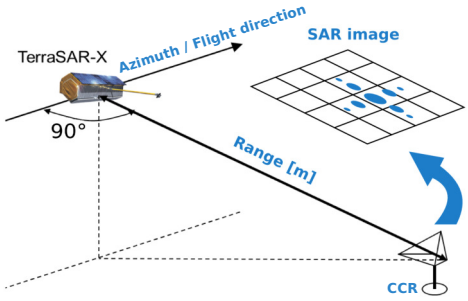

Fig. 2.13: Geometry of radar range measurements [Gisinger et al., 2015].

The passive reflectors on ground do not require a direct overflight of TerraSAR-X, since the reflectors have been precisely aligned to the TerraSAR-X orbit configuration. Typically, a reflector is seen from three adjacent ground tracks with a distance in viewing geometry ranging from 600 to 700 km. Herein, the incidence angle varies between approximately 25 and 55 degrees. The Sentinel-1A measurements are taken at an incidence angle of 38 degrees.

During the years 2012 to 2017, where the analysis in Section 5.3 refers to, the satellites TerraSAR-X and TanDEM-X have acquired in total 1,033 scenes for the five reflectors located at the geodetic stations. The imaging mode was the TerraSAR-X high resolution spotlight mode, which features an average resolution of 0.6 m by 1.1 m in slant range and azimuth, as well as a scene extent of approximately 5 km by 10 km [Fritz and Eineder, 2013]. Out of these acquisitions, 68 scenes had to be eliminated from the processing because they were rendered unusable by snow or water in the reflectors, which significantly reduce the signal backscatter. The degraded measurements are easily detected by computing the signal-to-clutter ratio (SCR) from the corner reflector point response in the radar image, and comparing it to the average SCR of the data series. Both satellites TSX-1 and TDX-1 captured data for all of the available reflectors, but in

the case of TDX-1 the majority of the data was acquired at OHG, while for TSX-1 the data distribution across the sites is more homogeneous.

3

Non-Gravitational Forces – Models

3.1 Satellite Macro Models

Modeling of accelerations, which act on the satellite surface like solar radiation pressure or atmospheric drag, require a description of the satellite geometry. The cannon-ball model, which is simple and robust, considers the satellite surface as a sphere with a fixed size and one set of surface properties. The complexity of the satellite shape can not be modeled properly with such models, e.g. during maneuvers, when the attack angle of e.g. photons in case of solar radiation pressure, changes.

Macro or plate models allow an approximation of the real satellite shape through a finite number of surface elements and, therefore, a simplified model of surface forces. Alternatives are detailed ray tracing simulations, which allow a very detailed surface description, but require detailed computer-aided design (CAD) models of the spacecraft and are computationally extensive. Accelerations are pre-computed depending on the grid point and position of radiation source, and then directly applied for POD purposes. In literature, examples of such ray tracing models for Jason-1 are available in Ziebart [2004], Adhya [2005] and Cerri et al. [2010]. Klinkrad and Fritsche [1998] discuss the impact of such models on the orbit determination of ERS-1.

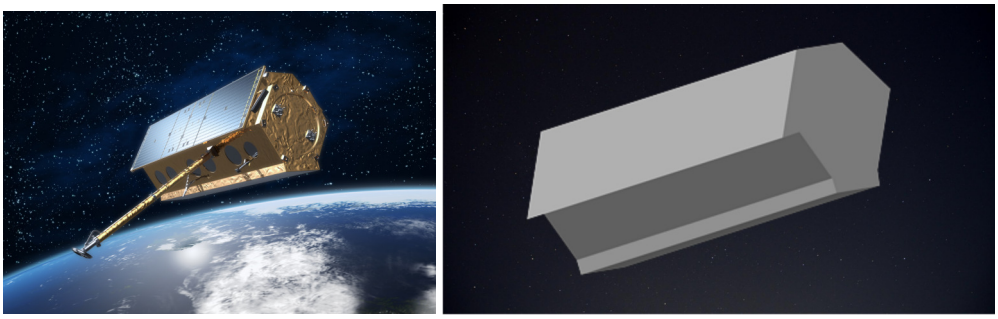

(a) (b)

Fig. 3.1: Artists view of (a) TerraSAR-X, and the corresponding (b) satellite plate model. Courtesy: DLR.

The spacecraft panel model, as it is used throughout this thesis, is characterized by a set of geometrical and optical properties. It is composed of several panels i, each with a size A_i, and the body-fixed surface normal vector $\boldsymbol{n}_i$. Specifically for radiation-dependent accelerations like solar or Earth radiation pressure, a set of optical properties is defined in visual (VIS) and infrared (IR) spectrum individually for each plate.

The satellite is mostly covered by foils like Black Kapton, Beta Cloth, or Aluminium/Alodin Foil, which prevent the spacecraft's payload from the extreme radiation [Pompea and Breault, 2009]. An overview of materials and coatings used in space industry is provided by Henninger [1984]. The passive thermal control system (PTCS) like multilayer insulation (MLI), or mirrors as optical solar reflector (OSR) are typical components of the spacecraft's thermal control system. The active thermal control system (ATCS) actively regulates the thermal budget by thermoelectric heaters/coolers. The OSR consists of coated surfaces (quarz or aluminized Teflon mirrors). The optical properties of these surfaces slowly change with time due to de-lamination. Especially the LEO regime is, due to the presence of atomic oxygen (cf. Section 3.3) affected by this type of degradation [Wernham, 2013; Gilmore et al., 2002; Gilmore, 2002]. Typical OSR absorptivity values at begin of lifetime (BOL) are at 5 %, whereas simulations stated values of 20 % at end of lifetime (EOL) for the Swarm OSR radiators. More on optical coefficients of materials in space are available e.g. in Shedal [2014] and Pompea and Breault [2009].

Within the following sections, the plate models of S-1A, SWC and TSX-1/TDX-1 are described in detail, whereas the stated optical properties provided at BOL, without considering any aging effects.

Table 3.1: Dimensions and visual optical properties of TerraSAR-X/TanDEM-X (total mass approx. 1,325 kg). Vectors in satellite body frame.

#						visual			infrared		
Plate	Surface	$\boldsymbol{n}_{i,x}$	$\boldsymbol{n}_{i,y}$	$\boldsymbol{n}_{i,z}$	$A_i\ [m^2]$	α_i	δ_i	ρ_i	α_i	δ_i	ρ_i
1	Solar array	0.0000	−0.9897	0.1434	5.93	0.70	0.07	0.23	0.81	0.04	0.15
2	Side 2 (MLI)	0.0000	−0.5586	−0.8295	3.89	0.21	0.63	0.16	0.70	0.24	0.06
3	Side 3 (MLI)	0.0000	0.3316	−0.9434	4.41	0.49	0.41	0.10	0.70	0.24	0.06
4	Side 4 (MLI)	0.0000	0.9927	−0.1208	6.23	0.30	0.56	0.14	0.65	0.28	0.07
5	SAR antenna	0.0000	0.6109	0.7917	3.69	0.48	0.42	0.10	0.71	0.23	0.06
6	Side 6 (MLI)	0.0000	−0.2716	0.9624	4.99	0.30	0.56	0.14	0.65	0.28	0.07
7	front (flight; MLI)	1.0000	0.0000	0.0000	3.20	0.34	0.53	0.13	0.62	0.30	0.08
8	rear (anti-flight; MLI)	−1.0000	0.0000	0.0000	3.20	0.34	0.53	0.13	0.62	0.30	0.08

3.1.1 TerraSAR-X/TanDEM-X

The geometrical and optical properties, which are required for building plate models, were provided by the spacecraft manufacturer Airbus DS by means of surface normal vectors and the plate size for representing the spacecraft's geometry [Ulrich and Airbus DS, 2013]. The average optical properties for each plate are described in the form of a material mixture matrix, which states all contributing materials with it's optical properties, and their percentage contribution to the plate. An illustration of the TDX-1/TSX-1 plate model, and an artist's illustration is shown in Figure 3.1.

The TSX-1 plate model is identical to the TDX-1 model and consists of 8 plates shown in Table 3.1. The geometric shape basically comprises the extruded, equilateral hexagon as body, whereas the SAR boom is not modeled separately. Each plate is characterized by a normal vector $\boldsymbol{n}_i$, which states the plate orientation in the satellite body-frame. A_i is the size of each plate.

Each plate has individual optical properties: the solar array (#1) for example, has a very high rate of radiation absorptivity, which is typical for solar arrays. Apart from the SAR antenna, the remaining plates have basically the purpose to shield the spacecraft from radiation. Therefore, their rate of reflectivity is rather high. Spontaneous re-emission is considered for each plate with a notable MLI contribution (cf. Table 3.1). Together with the spacecraft's attitude at time t, the plate orientation in inertial space can be computed.

Table 3.2: Dimensions and visual optical properties of the Sentinel-1A plate model (total mass approx. 2,145 kg). Vectors in satellite body frame.

#						visual			infrared		
Plate	Surface	$\boldsymbol{n}_{i,x}$	$\boldsymbol{n}_{i,y}$	$\boldsymbol{n}_{i,z}$	$A_i\ [m^2]$	α_i	δ_i	ρ_i	α_i	δ_i	ρ_i
1	front (flight; MLI)	1.0000	0.0000	0.0000	5.57	0.30	0.06	0.64	0.70	0.07	0.23
2	rear (anti flight; MLI)	−1.0000	0.0000	0.0000	5.57	0.30	0.06	0.64	0.70	0.07	0.23
3	side $+y$ (MLI)	0.0000	1.0000	0.0000	6.79	0.30	0.06	0.64	0.70	0.07	0.23
4	side $-y$ (MLI)	0.0000	−1.0000	0.0000	6.79	0.30	0.06	0.64	0.70	0.07	0.23
5	SAR antenna $+z$	0.0000	0.0000	1.0000	12.55	0.19	0.00	0.81	0.85	0.07	0.08
6	SAR antenna $-z$	0.0000	0.0000	−1.0000	12.55	0.44	0.00	0.56	0.76	0.12	0.12
7	Solar array front	0.0000	−0.8660	−0.5000	34.46	0.91	0.00	0.09	1.00	0.00	0.00
8	Solar array back	0.0000	0.8660	0.5000	34.46	0.92	0.00	0.08	0.72	0.18	0.00

3.1.2 Sentinel-1A

The macro model of S-1A has been developed during this thesis within the CPOD working group and is shown in Table 3.2. The model is based on the spacecraft description, available in Perellón et al. [2015]. The model basically represents the main spacecraft body as cube with attached solar arrays and SAR antenna. The solar array (#7) is characterized with a high absorptivity (91 %), no diffusive, and 9 % specular reflectivity. This is rather different compared to the TerraSAR-X solar cells, where the specular reflectivity is at 23 %, and reflects the uncertainties related to the provided optical properties. The Swarm plate model, for example, states a 10 % contribution of diffusive reflection but no specular reflection to the solar arrays. For the remaining plates of S-1A, the optical values are comparable to those from TSX-1.

3.1.3 Swarm-C

The macro model of SWC was developed during this thesis in cooperation with TU Delft and is based on optical data provided by the spacecraft manufacturer Airbus DS. Corresponding geometrical and optical properties are available in Table 3.3. Note that the complex shapes of coarse Earth Sun sensors (CESS) brackets, optical bench, launch bench, etc. are not considered. In total, the model consists of 15 plates, including the boom. The two solar array plates (#4 and #5) are characterized by a high level of absorptivity, comparable to the models of TerraSAR-X and Sentinel-1A.

Table 3.3: Dimensions and visual optical properties of Swarm-C (total mass approx. 473 kg). Vectors in body frame. Courtesy of Airbus DS.

#						visual			infrared		
Plate	Surface	$\boldsymbol{n}_{i,x}$	$\boldsymbol{n}_{i,y}$	$\boldsymbol{n}_{i,z}$	$A_i\ [m^2]$	α_i	δ_i	ρ_i	α_i	δ_i	ρ_i
1	Bottom surface (MLI)	0.0000	0.0000	1.0000	1.54	0.18	0.79	0.03	0.68	0.31	0.01
2	Tilted bottom surface center (MLI)	−0.1977	0.0000	0.9803	1.40	0.77	0.17	0.06	0.78	0.20	0.02
3	Tilted bottom surface boom (MLI)	−0.1381	0.0000	0.9904	1.60	0.86	0.14	0.00	0.78	0.22	0.00
4	Solar array left	0.0000	0.5878	−0.8090	3.45	0.90	0.10	0.00	0.72	0.28	0.00
5	Solar array right	0.0000	−0.5878	−0.8090	3.45	0.90	0.10	0.00	0.72	0.28	0.00
6	Top panel (MLI)	0.0000	0.0000	−1.0000	0.50	0.93	0.07	0.00	0.78	0.22	0.00
7	Front (MLI)	1.0000	0.0000	0.0000	0.56	0.20	0.80	0.00	0.17	0.83	0.00
8	Side wall (MLI)	0.0000	1.0000	0.0000	0.75	0.90	0.07	0.03	0.78	0.21	0.01
9	Side wall (MLI)	0.0000	−1.0000	0.0000	0.75	0.90	0.07	0.03	0.78	0.21	0.01
10	Shear panel front (MLI)	1.0000	0.0000	0.0000	0.80	0.45	0.00	0.55	0.80	0.00	0.20
11	Shear panel back (MLI)	−1.0000	0.0000	0.0000	0.80	0.93	0.07	0.00	0.78	0.22	0.00
12	Boom (MLI)	0.0000	1.0000	0.0000	0.60	0.67	0.03	0.30	0.79	0.09	0.12
13	Boom (MLI)	0.0000	−1.0000	0.0000	0.60	0.67	0.03	0.30	0.79	0.09	0.12
14	Boom (MLI)	−0.2392	0.0000	−0.9710	0.60	0.83	0.06	0.11	0.78	0.18	0.04
15	Boom (MLI)	0.2277	0.0000	0.9737	0.60	0.45	0.00	0.55	0.80	0.00	0.20

The nadir pointing panel #1 is equipped with OSR radiators, which results in a high level of diffusive reflection.

3.2 Radiation Pressure Models

Within this section, solar radiation pressure, and Earth radiation pressure models are introduced.

3.2.1 Solar Radiation

The Sun permanently emits solar photons, which impact upon the satellite surface, where they are either absorbed or reflected diffusively or specularly. The absorbed photons transfer their momentum to the spacecraft, following the principle of conservation of momentum. In addition, the reflected photons cause a recoil force on the spacecraft, and the impulse of the incident photon is transferred. Contrary to gravitational forces, the solar radiation pressure acceleration depends on structure and material of the surface, as well as the attitude of the spacecraft.

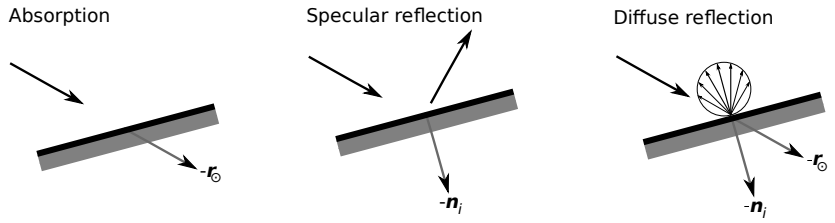

Fig. 3.2: Interaction of Photons (black arrow; emitted from the Sun ⊙) on a surface, and illustration of the resulting acceleration vectors.

Principally, the acceleration is directly proportional to the area of the spacecraft facing the Sun, inversely proportional to the spacecraft mass, and directly proportional to the solar irradiance. The solar irradiance is the energy flux per unit area at the spacecraft. Basically, the Sun emits radiation over a wide frequency spectrum. The energy distribution can be approximated by a black body radiator with a mean temperature of 5,785 K. Accounting for the emitted radiation at all wavelengths, the mean energy flux $P_\odot$ amounts to $1.367\,{}^{W}/_{m^2}$ at one astronomical unit (AU), which equals to $4.56 \cdot 10^{-6}\,{}^{N}/_{m^2}$ [McCarthy, 1996]. The symbol ⊙ denotes the Sun. The required optical

coefficients of diffusive reflection δ, specular reflection ρ, and absorption α (cf. Figure 3.2) are often determined by satellite manufacturers during the calibration and thermal tests on ground and available in Tables 3.2 for Sentinel-1A, 3.3 for Swarm-C, and 3.1 for TSX-1 and TDX-1.

The optical coefficients are related fulfilling

$$\alpha + \delta + \rho = 1 \quad . \tag{3.1}$$

In addition, the parameters of reflectivity ν, ranging from 0 (black) to 1 (white), and the specularity μ ranging from 0 (diffuse) to 1 (specular) are related via

$$\begin{aligned} \alpha &= 1 - \nu \\ \rho &= \mu\nu \\ \delta &= \nu(1 - \mu) \quad . \end{aligned} \tag{3.2}$$

Once the absorption α, the diffuse δ and the specular reflection ρ are known, one can easily determine the specularity of the corresponding material by

$$\mu = \frac{\rho}{1 - \alpha} \quad . \tag{3.3}$$

Solar Radiation Pressure Model

The interaction of particles with a surface causes an exchange of energy and momentum, as illustrated by Figure 3.2. Basic formulations of the implemented solar radiation pressure (SRP) model are published in Milani et al. [1987]. Important for applying the presented model are the availability of a macro model with geometrical and optical properties, as well as the spacecraft's position and attitude (cf. Section 3.1). Throughout this section, important parameters comprise:

m	total mass of spacecraft at time t,
A_i	surface of satellite plate,
α_i	fraction of absorbed photons,
δ_i	fraction of diffusely scattered photons,
ρ_i	fraction of specularly reflected photons,
$\boldsymbol{r}_\odot$	satellite to Sun direction unit vector,
$\boldsymbol{n}_i$	satellite surface normal unit vector, and

$\theta_i^{\odot}$ angle between surface normal and Sun direction vectors.

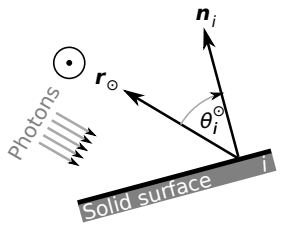

Fig. 3.3: Incident radiation from Sun on plate with unit vectors.

The parameter i denotes the plate number. Figure 3.3 illustrates the angle $\theta_i^{\odot}$ between the surface plate normal vector and the vector in direction to the incident radiation, which is described by

$$\cos\theta_i^{\odot} = \boldsymbol{r}_{\odot} \cdot \boldsymbol{n}_i \quad . \tag{3.4}$$

Note that the satellite plate i is only illuminated for $\theta_i^{\odot} > 0$. The solar radiation pressure model treats absorbed, specularly and diffusively reflected photons individually.

An absorbed photon transfers all its momentum to the panel, whereby the resulting acceleration is in direction away from the source of radiation, i.e. $-\boldsymbol{r}_{\odot}$. The corresponding absorption term reads:

$$\boldsymbol{C}_{R,\alpha,i} = -\alpha_i \boldsymbol{r}_{\odot} A_i \cos\theta_i^{\odot} \quad . \tag{3.5}$$

The contribution of specularly reflected photons is modeled according to

$$\boldsymbol{C}_{R,\rho,i} = -2\rho_i \cos\theta_i^{\odot} \boldsymbol{n}_i A_i \cos\theta_i^{\odot} \quad . \tag{3.6}$$

The coefficient is proportional to $A_i \cos\theta_i^{\odot}$ and to $2\cos\theta_i^{\odot}$, the $\boldsymbol{n}_i$ component transferred by the incident radiation.

The diffuse reflection term considers an absorbed component in direction $-\boldsymbol{r}_{\odot}$ and, according to Lambert's law, re-emitted photons:

$$\boldsymbol{C}_{R,\delta,i} = -\left(\delta_i \boldsymbol{r}_{\odot} + \frac{2}{3}\delta_i \boldsymbol{n}_i\right) A_i \cos\theta_i^{\odot} \quad . \tag{3.7}$$

Adding equations 3.5, 3.6, and 3.7 under consideration of Equation 3.1, the Sun as power of radiation, and the dimensionless scaling parameter C_R in

$$\ddot{\boldsymbol{r}} = C_R P_\odot \frac{1\mathrm{AU}^2}{r_\odot^2} \frac{1}{m} \sum_{i=1}^{n} \left[\boldsymbol{C}_{R,\alpha,i} + \boldsymbol{C}_{R,\rho,i} + \boldsymbol{C}_{R,\delta,i} \right] \quad , \tag{3.8}$$

one ends up with the equation from Milani et al. [1987]:

$$\ddot{\boldsymbol{r}} = -C_R P_\odot \frac{1\mathrm{AU}^2}{r_\odot^2} \frac{1}{m} \sum_{i=1}^{n} \left[\left((1-\rho_i)\boldsymbol{r}_\odot + 2\left(\frac{\delta_i}{3} + \rho_i \cos\theta_i^\odot\right)\boldsymbol{n}_i \right) A_i \cos\theta_i^\odot \right] \quad . \tag{3.9}$$

Equation 3.9 assumes that all absorbed energy is stored in the system. Structures like MLI have zero thermal capacity and completely prevent heat transfer towards the satellite interior. Considering these areas, Fliegel et al. [1992] states, that a part of the energy absorbed by the satellite is instantaneously re-radiated as heat. Considering Lambert's law and stating the absorption coefficient α, the coefficient for instantaneous thermal re-radiation reads

$$C_{R,\alpha t,i} = -\frac{2}{3} \alpha_i \boldsymbol{n}_i A_i \cos\theta^\odot \quad . \tag{3.10}$$

Adding this term to equation

$$\ddot{\boldsymbol{r}} = C_R P_\odot \frac{1\mathrm{AU}^2}{r_\odot^2} \frac{1}{m} \sum_{i=1}^{n} \left[C_{R,\alpha,i} + C_{R,\rho,i} + C_{R,\delta,i} + C_{R,\alpha t,i} \right] \quad , \tag{3.11}$$

one finally ends up with

$$\ddot{\boldsymbol{r}} = -C_R P_\odot \frac{1\mathrm{AU}^2}{r_\odot^2} \frac{1}{m} \sum_{i=1}^{n} \left[\left((\alpha_i + \delta_i)\boldsymbol{r}_\odot + \left(\frac{2}{3}(\delta_i + f_\alpha \alpha_i) + 2\rho_i \cos\theta_i^\odot\right)\boldsymbol{n}_i \right) A_i \cos\theta_i^\odot \right] \quad . \tag{3.12}$$

Equation 3.12 provides the acceleration on the spacecraft due to solar radiation pressure under the assumptions that a fraction f_α of the absorbed radiation is instantaneously re-radiated in the form of heat, which is valid for surface materials that have zero thermal capacity, and prevent heat transfer towards the satellite, like the MLI structure. For other surfaces that have thermal capacity, this assumption constrains the satellite model and may lead to systematic effects [Cerri et al., 2010; Rodriguez-Solano et al., 2012]. For SRP computations based on Equation 3.11 a factor of $f_\alpha = 1$ is employed for all panels of a macro model representing MLI-covered surfaces, while $f_\alpha = 0$ is assumed for all other panels. Related effects on the orbit solutions are shown in Section 4.2, which also comprises a comparison of different macro model sophistication levels.

Compared to the model in Equation 3.9, the cannon-ball model

$$\ddot{\boldsymbol{r}} = -C_R P_\odot \frac{A}{m} \frac{\boldsymbol{r}_\odot}{r_\odot^3} \mathrm{AU}^2 \tag{3.13}$$

assumes that the average normal surface vector $\boldsymbol{n}$ is pointing in the direction of the sun, which especially suffices for satellites with huge solar arrays [Montenbruck and Gill, 2005]. The relatively simplistic model only considers a single cross-sectional area A, and is independent from the attack angle.

3.2.2 Earth Radiation

The Earth radiation pressure (ERP) refers to short wave energy (ie. wavelength between $0.2\,\mu$m and $4.0\,\mu$m) reflected from Earth, and long wave energy (above $4\,\mu$m wavelength) emitted by the Earth, both impacting the satellite due to surface interactions (cf. Figure 1.1). Averaging the incoming energy from the Sun over the whole Earth surface, the mean incident energy is approximately $350\,\mathrm{W/m^2}$. Out of this, roughly one third is reflected in the visual spectrum (25 % reflected by clouds, and 7 % reflected by continents and oceans), while the remaining two thirds of the incident radiation are absorbed by the atmosphere, soil, and water. The absorbed energy is re-emitted primarily as infrared radiation, and the thermal component causes the Earth to appear as a black body radiator of a mean temperature at 253 K. Earth radiation models play a key role in understanding the energy balance of the system Earth [Stephens et al., 1981, 2015]. Physical modeling of Earth radiation pressure is similar to SRP, but with a different source of radiation. In case of solar radiation pressure, the irradiance is fairly stable and only varies slightly with the distance spacecraft-Sun. Contrary to that, the amount of radiation, which is (re-)radiated from the Earth's surface varies significantly over one orbit, since it depends on highly changeable environmental variables such as cloud or land cover. To properly model these aspects, a model with optical coefficients of the Earth's surface is introduced, which allows to describe the ERP flux as a function of time, Sun illumination and geographic location.

Earth Radiation Pressure Model

The ERP model implemented for the present work follows the basic concepts of Knocke et al. [1988] and Knocke [1989] but uses a slightly different partitioning of the visible Earth surface. The first step in Earth radiation pressure modeling is determining the ERP flux, i.e. the amount of the direct solar radiation flux, which is reflected and absorbed/emitted in the spectrum of visible and infrared energy. The Sun illuminates the Earth surface (the Earth is denoted by $\oplus$), and a part of the incident solar radiation is reflected in the direction of the satellite. As seen from the satellite, the visible Earth surface is divided into k elements of area ΔA_j, with $j = 1,\cdots,k$. Within the present study, $k = 3$ ring division of the sub-satellite Earth cap is chosen (cf. Figure 3.4). Under as-

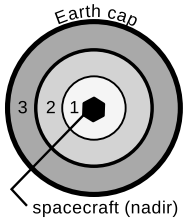

Fig. 3.4: Earth cap below the spacecraft and division in k=3 segments. Each segment j has a size A_j.

sumption of a Lambertian surface, the reflected energy flux of Earth surface element j is given by

$$P_{\oplus \mathrm{VIS},j} = P_{\odot} \frac{\rho_{\oplus}}{\pi r_j^2} \cos\theta_{\oplus \mathrm{in}} \cos\theta_{\oplus \mathrm{out}} \Delta A_j \tag{3.14}$$

with

$\rho_{\oplus}$	fraction of reflected photons in visual spectrum,
$\boldsymbol{r}_j$	vector between Earth surface element j and satellite,
$\theta_{\oplus \mathrm{in}}$	angle between Earth surface normal and incident, solar radiation vectors, and
$\theta_{\oplus \mathrm{out}}$	angle between Earth surface normal and satellite direction vectors.

The expression is only valid for $\cos\theta_{\oplus \mathrm{in}} \geq 0$ (Earth surface element illuminated by Sun), and $\cos\theta_{\oplus \mathrm{out}} \geq 0$ (satellite visible from Earth). In addition to the reflected radiation, the Earth absorbs incoming energy and re-emits it as thermal radiation. Given the emissivity

$\epsilon_\oplus$, i.e. the ratio of emitted radiation with respect to a perfect black body of the same temperature, the equation for the flux of re-emitted infrared radiation reads

$$P_{\oplus\mathrm{IR},j} = P_\odot \frac{\epsilon_\oplus}{4\pi r_j^2} \cos\theta_{\oplus\mathrm{out}} \tag{3.15}$$

with $\epsilon_\oplus$ stating the emissivity of a Earth surface element. The re-emitted infrared radiation covers the whole Earth surface $4\pi R_\oplus^2$ [Taylor, 2005].

Figure 3.5 shows the required angles. The coefficients $\rho_\oplus$ and $\epsilon_\oplus$ require knowledge of Earth radiation models, which are discussed later.

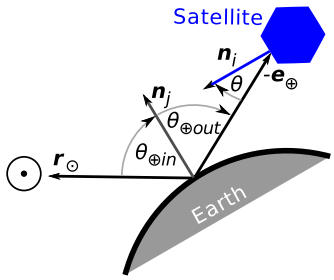

Fig. 3.5: Required angles for Earth radiation modeling.

For a macro model comprising plates $i = 1,\cdots,n$, the acceleration due to radiation reflected by the Earth surface element j is computed via

$$\ddot{\boldsymbol{r}}_{\mathrm{VIS},j} = P_{\oplus\mathrm{VIS},j} \frac{1}{m} \sum_{i=1}^{n} \left[\left((\alpha_i + \delta_i)(\boldsymbol{e}_{\oplus,j} + \frac{2}{3}\boldsymbol{n}_i) + 2\rho_i \cos\theta_i \boldsymbol{n}_i \right) A_i \cos\theta_i \right] \tag{3.16}$$

with

$P_{\oplus\mathrm{VIS},j}$	reflected power by Earth element j in VIS spectrum,
$\boldsymbol{e}_{\oplus,j}$	satellite to Earth surface element unit vector,
θ_i	angle between satellite surface normal vector and unit vector from satellite to Earth surface element,
α_i	fraction of absorbed photons,
δ_i	fraction of diffusely scattered photons and
ρ_i	fraction of specular reflected photons.

In the IR spectrum, the resulting acceleration $\ddot{r}_{\mathrm{IR}_j}$ corresponds to Equation 3.16, but the coefficients α_i, δ_i, and ρ_i have to be replaced by the values in the IR spectrum.

Both quantities consider absorption, thermal re-radiation, diffuse and specular reflection. The total acceleration due to ERP for all visible Earth surface elements k is obtained by summing the contributions from all surface elements of the visible part of the Earth:

$$\ddot{\boldsymbol{r}} = C_E \sum_{j=1}^{k} \left(\ddot{r}_{\mathrm{VIS},j} + \ddot{r}_{\mathrm{IR},j} \right) \quad . \tag{3.17}$$

The parameter C_E is a scaling factor that is estimated in the RDOD approach.

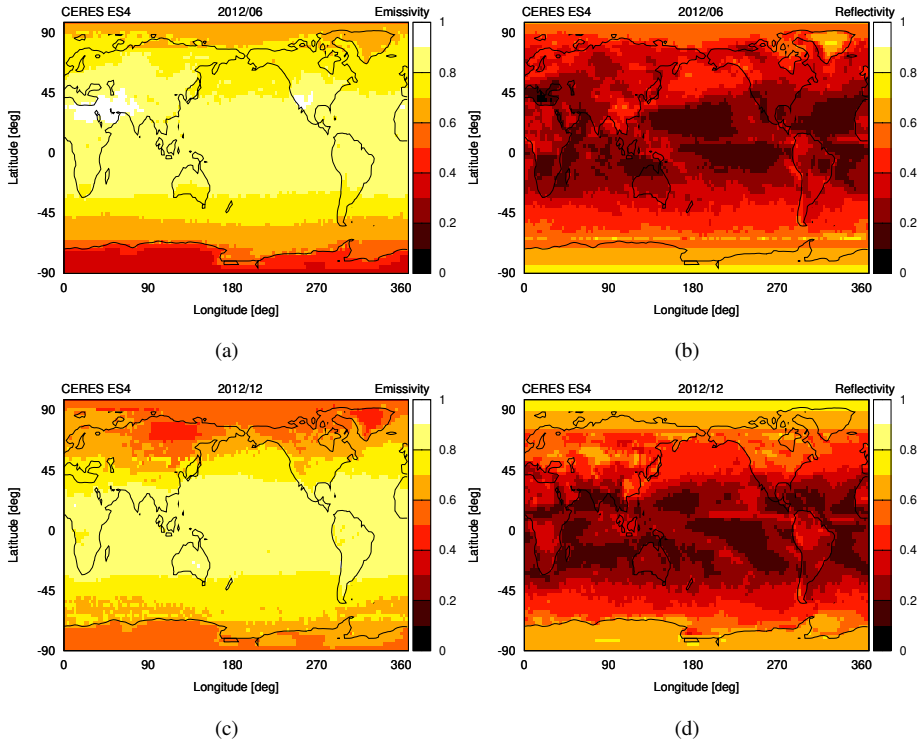

Fig. 3.6: Monthly CERES ES-4 maps for (a) emissivity and (b) reflectivity in June 2012, and (c) emissivity and (d) reflectivity in December 2012.

Earth Radiation Model CERES

Earth radiation requires knowledge of the Earth's emissivity (called albedo) and reflectivity. Therefore, the Clouds and Earth's Radiant Energy System (CERES) ES-4 data product is utilized, which basically delivers monthly fields of emissivity and reflectivity in global maps, each with a grid size of $2.5° \times 2.5°$, similar to the Earth Radiation Budget Experiment [ERBE; Wielicki et al., 1996; Barkstrom, 1984]. According to the CERES model description, the reflective shell of the Earth is considered at the top of atmosphere (TOA) in an altitude of 30 km [Priestley et al., 2011].

Figure 3.6 shows the emissivity and reflectivity of the Earth's surface as a monthly average in June 2012, gridded in bins of $2.5 \times 2.5°$. The emissivity is dominant along the equator, especially in desert regions. The reflectivity map shows a pronounced amount of reflectivity on the south pole, covered by snow, and over Greenland.

For a computationally efficient representation of the CERES data, the monthly fields are represented by simplified model functions. First, the monthly fields of emissivity ϵ and reflectivity ρ for epoch t are approximated through a second order polynomial of the sine of the geographical latitude φ [Knocke et al., 1988]:

$$\begin{aligned} \rho &= \rho_0(t) + \rho_1(t) \cdot P_1(\sin\varphi) + \rho_2(t) \cdot P_2(\sin\varphi) \quad , \\ \epsilon &= \epsilon_0(t) + \epsilon_1(t) \cdot P_1(\sin\varphi) + \epsilon_2(t) \cdot P_2(\sin\varphi) \quad , \end{aligned} \tag{3.18}$$

with

$$P_0(x) = 1; \quad P_1(x) = x; \quad P_2(x) = \frac{1}{2}(3x^2 - 1) \tag{3.19}$$

and denoting the Legendre polynomials of order one and two [Bronstein et al., 2008]. By averaging over all longitudes, the longitudinal dependence of the modeled emissivity and reflectivity is removed.

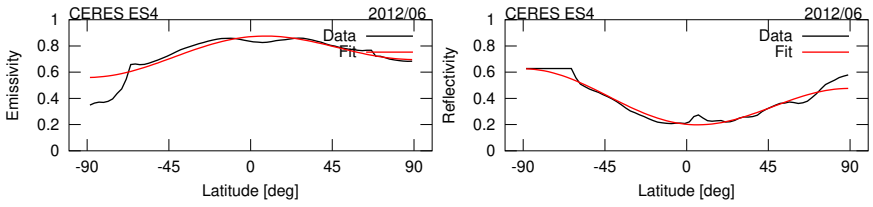

(a) (b)

Fig. 3.7: Model data and polynomial fit of (a) emissivity and (b) reflectivity in June 2012.

In the least-squares adjustment of coefficients $\rho_{0,1,2}$ and $\varepsilon_{0,1,2}$ from the observed CERES values of emissivity and reflectivity, individual grid points are weighted with $\cos\varphi$ to account for the latitude dependence of the corresponding cell areas. The latitude variation of longitude-averaged CERES data for a sample month and the corresponding fit are shown in Figure 3.7. Short scale variations can not be represented properly and are neglected when considering ERP in the orbit computations.

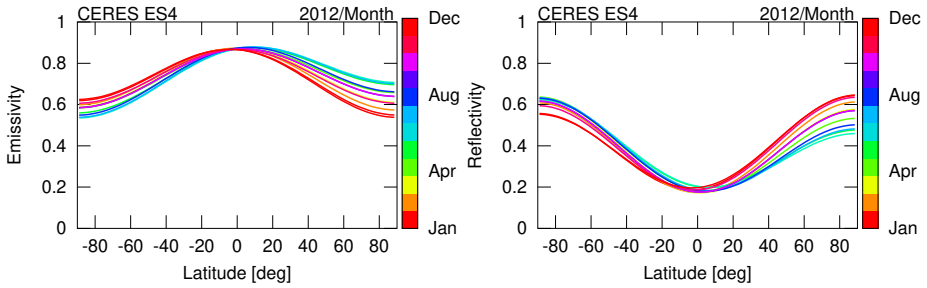

Fig. 3.8: Monthly series of (a) emissivity and (b) reflectivity, obtained from CERES ES4 data.

An overview of latitude dependent values for emissivity and reflectivity is provided by Figure 3.8. Season variations are clearly visible for the northern and southern hemisphere. The difference between model data, and the latitude-dependent polynomial fit is in the order of less than 10 %, assessed based on monthly CERES fields of the year 2012. Seasonal variations are approximated through a harmonic series expression

$$\begin{aligned} \epsilon_i(t) &= \epsilon_{\{i,X\}} + \epsilon_{\{i,c\}} \cdot \cos\left(\varpi(t-t_0)\right) + \epsilon_{\{i,s\}} \cdot \sin\left(\varpi(t-t_0)\right) \quad \text{, and} \\ \rho_i(t) &= \rho_{\{i,X\}} + \rho_{\{i,c\}} \cdot \cos\left(\varpi(t-t_0)\right) + \rho_{\{i,s\}} \cdot \sin\left(\varpi(t-t_0)\right) \end{aligned} \tag{3.20}$$

with

$$\varpi = \frac{2\pi}{365.2425\,\text{days}} \quad . \tag{3.21}$$

Table 3.4 provides the derived coefficients for 2012. To obtain the values of emissivity and reflectivity in a synthesis, first the coefficients at time t have to be derived based upon the values in Table 3.4 and Equations 3.20. Subsequently, the derived coefficients are directly employed in Equations 3.18, which finally delivers the values of emissivity and reflectivity.

Table 3.4: Coefficients for series expansion of CERES ES-4 model in 2012.

	ρ_0	ρ_1	ρ_2
ρ_X	0.319	−0.025	0.266
ρ_c	0.007	0.060	0.023
ρ_s	0.000	−0.012	−0.004
	ϵ_0	ϵ_1	ϵ_2
ϵ_X	0.782	0.024	−0.176
ϵ_c	−0.008	−0.057	−0.011
ϵ_s	0.000	0.001	0.000

3.3 Aerodynamics

The first part of this section gives an introduction to the Earth's atmosphere and related measures, which are required for atmospheric density modeling. In the second part, different aerodynamic acceleration models are introduced and compared.

3.3.1 The Earth's Atmosphere

The thermosphere is the atmospheric layer beginning at about 80 km above ground. Lower layers are the troposphere, stratosphere, mesosphere, the upper layer is called exosphere. There is no definite boundary in outer space, since the number of atmospheric particles exponentially decreases with altitude. In spaceflight, atmospheric effects play a major role, as the aerodynamic friction is the most dominating acceleration for a low Earth orbiting satellite [Jastrow and Pearse, 1957].

The magnitude of the atmosphere is not constant with time since the distribution of atmospheric constituents changes. In an altitude between 500 and 600 km, which is of main importance for the present study, the main atmospheric constituent is oxygen, which is extremely sensitive to the solar activity [Visconti, 2016].

Figure 3.9 shows the temperature and density with increasing altitude above central Europe for two selected days with high and low solar activity, at day and nighttime respectively. The profiles are computed based upon the US Naval Research Laboratory Mass Spectrometer and Incoherent Scatter Radar 2000 (NRLMSISE-00) model, which is introduced later in this section. Above an altitude of 100 km, the temperature in-

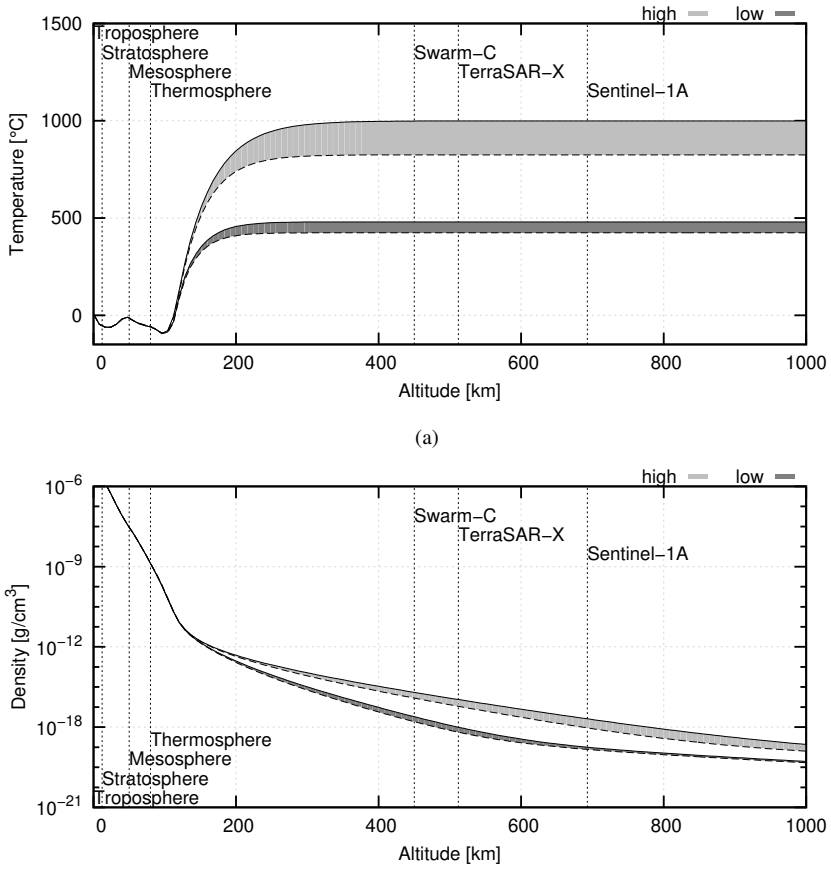

Fig. 3.9: Altitude profiles of temperature (a) and density (b) above central Europe for days with high (2002/02/01) and low (2008/02/01) solar activity at day (13:00 local time; solid lines) and night (1:00 local time; dashed lines), modeled with NRLMSISE-00.

creases monotonically and approaches an almost constant value of 500 °C to 1000°C above 300 km.

Obviously, the temperature profile increases with altitude and shows the definition of the atmospheric layers at that points, where the slope of the temperature profile changes. Contrary, the atmospheric density decreases with altitude, but both the density and temperature show a correlation for days with high and low solar activity.

Both quantities, the density κ and the temperature T of the Earth's atmosphere, are related by the ideal gas law

$$\frac{p}{\kappa} = \frac{RT}{M} \tag{3.22}$$

with p being the pressure, R the universal gas constant (8.3143 J/K/mol) and M the mean molecular mass of the gas [Böhm and Schuh, 2013]. The universal gas constant is related to the Boltzmann constant k and the Avogadro constant N_A via $R = N_A k$. The hydrostatic equilibrium is the balance between the pressure pushing gas into outer space and the gravity g at height above ground z, pulling it towards the Earth and described by the differential equation:

$$\frac{dp}{dz} = -\kappa(z)g(z) \quad . \tag{3.23}$$

Atmospheric pressure can be computed by combining Equation 3.22 and 3.23 as a function of altitude

$$p(z) = p(0)e^{-\int_0^z H(z)^{-1}dz} \quad , \tag{3.24}$$

including the pressure scale height

$$H(z) = \frac{RT(z)}{g(z)M(z)} \quad . \tag{3.25}$$

Simultaneously, the variation of density with altitude reads

$$\kappa(z) = \kappa(0)e^{-\int_0^z H'(r)^{-1}dr} \quad , \tag{3.26}$$

where the density scale height is defined as

$$H'(z)^{-1} = T(z)^{-1}\frac{dT(z)}{dz} + \frac{g(z)M(z)}{RT(z)} \quad . \tag{3.27}$$

In the upper thermosphere, where the temperature is almost constant, the scale height is equal to the pressure height.

Density and temperature profiles are shown in Figure 3.9 for days with high and low solar activity at day and nighttime. The variety of heat sources causes distinct extremes below 100 km altitude, while the variation in the thermosphere, which is of most interests for LEOs, is mostly driven by the absorption of extreme ultraviolet (EUV) radiation. The emission of electromagnetic radiation from the Sun is related to the activity of the Sun's magnetic field, the interaction of this magnetic field with the Sun's surface, and in its atmosphere. Especially at short wavelengths of 170 nm and less, the EUV radiation is mostly responsible for the thermosphere's heating by excitation, dissociation or ionization of atomic oxygen (O), molecular oxygen (O_2), and molecular nitrogen (N_2) [Rees, 1989]. Ionized gas particles in the thermosphere create the Earth's ionosphere. Charged particles in the atmosphere affects the electrical properties, which affect the heating of the atmosphere. Charged particles enter the Earth's magnetic field at the polar cups.

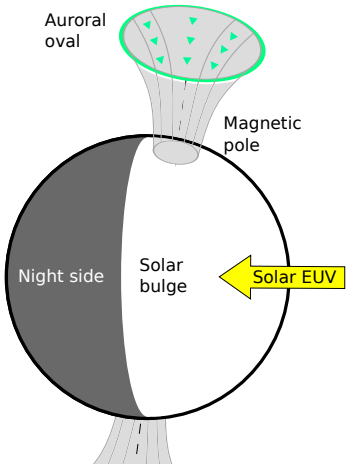

Fig. 3.10: Solar extreme ultraviolet (EUV) radiation and auroral oval at the magnetic poles Doornbos [2011].

According to Knipp et al. [2004], large solar flares and coronal mass ejection at the Sun can lead to a magnified energy deposition in the auroral zone, compared to the incoming EUV radiation. Figure 3.10 shows the incoming charged particles at the auroral oval at the magnetic poles [Brekke, 2013].

Figure 3.11 shows the mass concentrations of the atmospheric constituents modeled with NRLMSISE-00 [Picone et al., 2002]. For low solar activity, atomic oxygen is dominating below 500 km, while other major thermospheric constituents are molecular nitrogen, Helium (He), and Hydrogen (H). For high solar activity, atomic oxygen also dominates the regime above 500 km, which is caused by the atmospheric heating. For

low altitudes, the free gas path is short for the atmospheric constituents, which means that the atmosphere is well mixed.

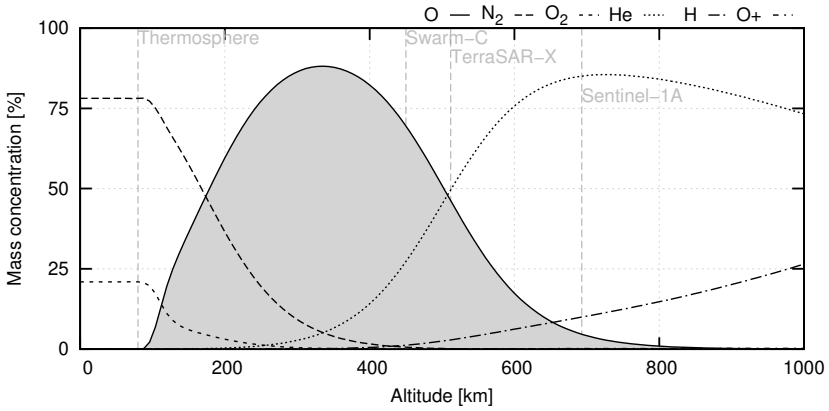

(a)

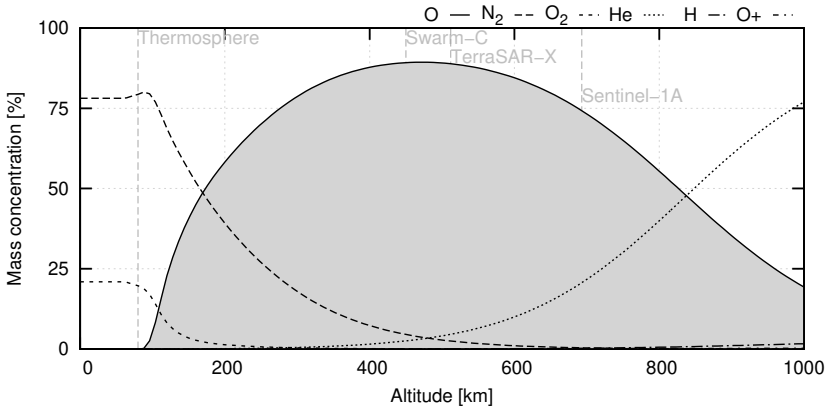

(b)

Fig. 3.11: Altitude profiles of atmospheric mass percent concentrations for days with low (a), (2008/02/01) and high (b), (2002/02/01) solar activity above southern Germany, modeled with NRLMSISE-00. The contributions of Ar and N are negligible at this scale.

3.3.2 Geomagnetic and Solar Activity Indicators

The complex interactions of the solar wind and the geomagnetic effects on the atmosphere indicate the need for a vast amount of parameters to properly model the atmospheric density. Two parameters are directly related to the atmospheric density and serve as input for atmospheric density models: solar flux and geomagnetic activity [Vallado and Finkleman, 2008]. In general, there is a difference between indices and proxies used below. An index is a quantity defined through a pre-determined standard that is directly derived from observations. It is often designed by making use of multiple observations in order to be able to summarize complex phenomena and interactions and simplify the modeling process. Contrary to that, a proxy is defined as an observation or measurement of a quantity that shows a high correlation with the phenomena of interest. Reliance on proxies is sometimes necessary and often preferred when they are easier to obtain or a more complete historical record is available.

Solar Flux The Flux 10.7 cm ($F_{10.7}$) proxy is a measure for the solar EUV radiation at 10.7 cm wavelength. Galileo Galilei first documented the sunspots in 1610, Jacchia [1959] later identified the correlation between the thermospheric density with the number of sunspots. In addition, he also discovered the solar radiation influence from the 27-day Sun rotation period. Satellites are perfectly suited for directly measuring the EUV radiation in the thermosphere [Floyd et al., 2005]. Historically, daily radio telescope measurements, operated by the National Research Council at Ottawa and at Penticton (British Columbia) provide measurements from 1947 onwards. Related data are provided, for example, by the National Oceanic and Atmospheric Administration (NOAA), or CelesTrak [Vallado and Kelso, 2013]. Throughout this thesis, the NOAA/SPace Weather Center (SPWC) solar flux and geomagnetic data are utilized[1].

The $F_{10.7}$ proxy is expressed in solar flux units (SFU), with $1\,\mathrm{SFU} = 10^{-22}\,\mathrm{W/m^2Hz}$ [Tapping, 2013]. The magnitude ranges from 70 SFU during solar minimums to around 300 SFU during extremely active days. The daily value of the index is observed at approximately 20 : 00 universal time (UT) and serves as input to density models. The adjusted value is normalized to a Sun-Earth distance of 1 AU. Jacchia [1959] detected that the EUV heating consists of one component related to active regions on the solar disk and one on the disk itself. Since the latter is only slowly varying, it is well represented by a centered moving average over three or four solar rotations corresponding

[1] `ftp://ftp.swpc.noaa.gov/pub/indices/`

to 81 or 108 days [Jacchia and Slowey, 1973]. As shown in Figure 3.12, there is a correlation between $F_{10.7}$ and the number of sunspots.

Geomagnetic Activity Geomagnetic activity, the frequency and intensity of magnetic disturbance, describe the interaction of charged particles from the solar wind and their interaction with the magnetosphere [Mayaud, 1980]. According to Bartels et al. [1939] the 'Potsdamer erdmagnetische Kennziffer' is known as kp index, whereas the 'p' indicates the planetary average. It is based on observations of the geomagnetic field performed by a global network of geomagnetic observatories. For each station, *k*-index is a quasi-logarithmic measure for the intensity of irregular variations in the horizontal magnetic field. Station-specific *k*-indices are combined into the global planetary *k*-index as a measure of the overall geomagnetic activity Menvielle and Berthelier [1991]; Bartels et al. [1939]. The index ranges from 0 to 9 with steps of one third. The kp index is dimensionless, but it can be converted to the ap index, which gives an approximate amplitude of geomagnetic perturbation. The transformation is simply done by a lookup table, the output values are then given in units of nT [Poole, 2002].

An explanation of the systematic effects shown in Figure 3.12 can be grouped in solar activity and geomagnetic activity variations, which are described in detail below. The variation in the solar activity causes a variation in the heating of the thermosphere, caused by solar radiation. Processes on the Sun are responsible for this variation. The associated EUV radiation is then mainly absorbed by the thermosphere. During the 11-year solar cycle period, the Sun emits less EUV radiation at periods with smaller sunspot numbers, while at the maximum of the 11-year solar cycle, the EUV radiation output is much higher. Furthermore, the 27-days rotation of the Sun causes another variation of the EUV radiation. With increasing altitude in the thermosphere, the caused density variation due to EUV radiation are more pronounced, too.

The geomagnetic activity variation mainly relates to coronal mass ejections and solar flares. During such events, the Sun ejects huge amounts of charged particles, which are mainly shielded by the magnetic field of the Earth. Only at the polar caps, parts the charged particles can enter the Magnetopause and cause geomagnetic storms, which are often visible as auroral displays. These events can lead to density variations on the order of one magnitude. The geomagnetic index allows to consider these effects.

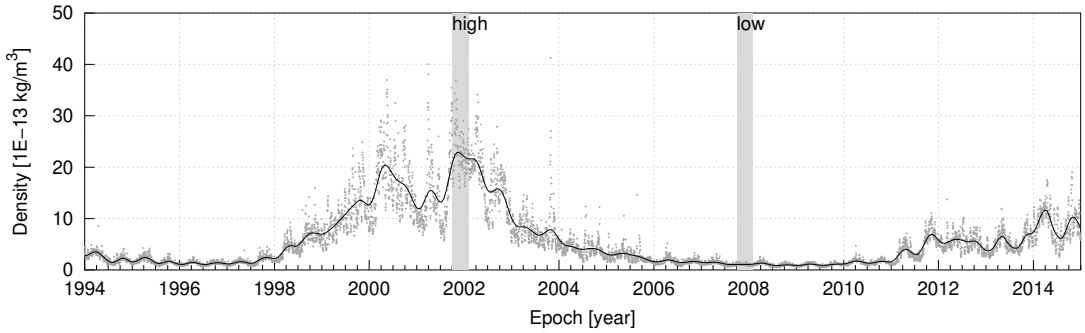

(a)

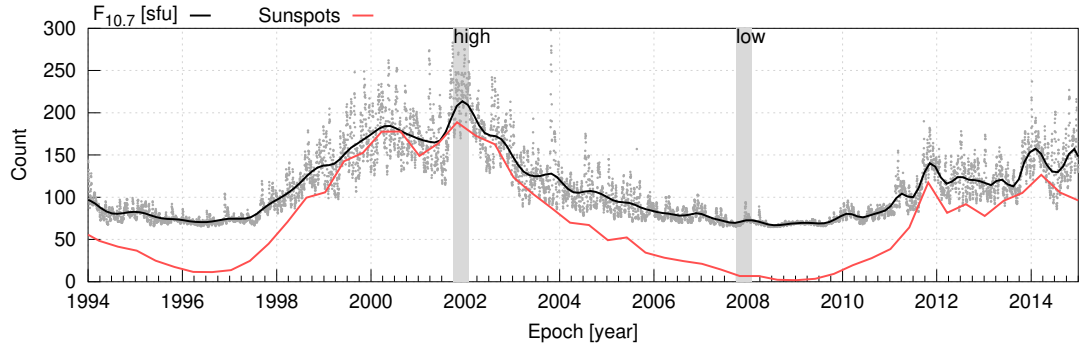

(b)

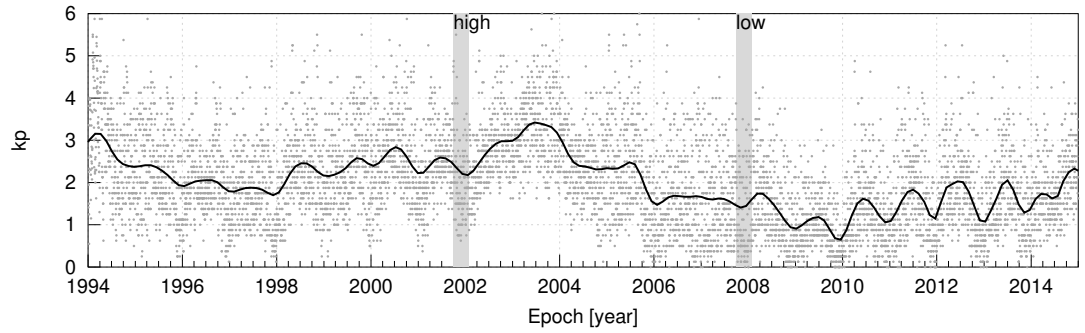

(c)

Fig. 3.12: Series of (a) atmospheric density above central Europe, (b) number of sunspots and solar flux at $10.7\,\mathrm{cm}$, and (c) geomagnetic k_p index. Periods of high and low solar activity are marked separately.

3.3.3 Atmospheric Density Models

Atmospheric density models describe the physical status of the atmosphere based on physical properties, e.g. temperature, pressure, scale height, mean molecular weight, as a function of local time for a defined altitude range. New sources of observation data, e.g. accelerometers on satellites, have largely driven the development of new density models. The models differ widely in the number of observed data, considered atmospheric constituents, and required input parameters. For an overview of existing atmospheric density models is referred to Vallado [2007]. Three well established atmospheric density models, namely Jacchia-71 [Jacchia, 1970], Drag Temperature Model 2012 (DTM 2012) [Bruinsma et al., 2012, updated], and NRLMSISE-00 [Picone et al., 2002] have been selected for the present study and are elaborated briefly in this section. A detailed description of the mentioned, and of many other atmospheric density models is provided by the American Institute of Aeronautics and Astronautics [2004].

Jacchia Series

The availability of observed orbital motions of satellites under the influence of drag paved the way for first empirical density models as published by Harris and Priester [1962], and Jacchia [1965, 1970, 1971]. The Committee On Space Research (COSPAR) adopted the Jacchia-71 model in 1972 as COSPAR International Reference Atmosphere 1972 (CIRA-72), which has been widely used as an atmospheric density model [Jacchia, 1977]. Later on, the Jacchia-71 model established the basis for further atmospheric density models [Owens, 2002; Bowman et al., 2008].

The model is based upon measurements of the acceleration of satellites and includes atmospheric density variations as a function of time [Jacchia, 1971]. Solar activity data, combined with a model of diurnal variation are selected to compute the exospheric temperature, with additional corrections depending on time and altitude. Based upon the exospheric temperature, a temperature profile is computed which is then selected as input for integrating the barometric equation. Finally, time-dependent corrections are applied to the density, which account for the observed density variations. The Jacchia-71G model, which is employed within this study, is consistent to the official model, but slightly enhanced to optimize the computational time [Gill, 1996].

DTM Series

The first Drag Temperature Model (DTM) was published by Owens [2002], which is, like, the Jacchia models, based on satellite drag observations and neutral temperature profiles. With availability of satellite data, several versions of DTM models were released [Berger et al., 1998]. For the present study, the DTM 2012 was selected, which also includes accelerometer data from the CHAMP mission [Bruinsma et al., 2012].

In the DTM 2012 model, the temperature profile with height is a function of the exospheric temperature. Contrary to the Jacchia algorithm, the density is not derived via direct integration with altitude over the temperature profile. The model includes submodels for the thermospheric temperature and number densities of each atmospheric constituent, e.g. H, He, O among others. Based on spheric harmonic terms, the density is computed for each of the atmospheric constituents individually and then finally summed up. The coefficients of these terms have been computed via a least squares approach using large databases of temperature and density measurements.

The latest release of the DTM series is the Drag Temperature Model 2013 (DTM 2013), shortly published after the present study [Bruinsma, 2015]. It basically comprises extended gravity measurements, additionally also from GRACE and GOCE.

NRLMSISE-00

The formulation behind NRLMSISE-00 is largely based on the Mass Spectrometer Incoherent Scatter (MSIS) model updates. The MSIS models, published by Hedin et al. [1977] were based on mass spectrometer and incoherent scatter radar observations. The MSIS-86 realization replaced the Jacchia-71 model as COSPAR standard atmosphere, known as COSPAR International Reference Atmosphere 1986 (CIRA-86) [Hedin, 1987]. The MSIS model development was continued by the US Naval Research Observatory (NRL) in the 1990s. The updates are mainly driven by including drag measurements and accelerometer data from various spacecraft. Including these measurements also compensated a substantial gap of the earlier MSIS models, since they do not include density data based on orbital dynamics [Picone et al., 2002]. Incoherent scatter radar data were included up to 1998 as well as thermospheric temperature measurements from the Millstone Hill mass spectrometer in the range from 100–130 km altitude. NRLMSISE-00 contains also data from National Aeronautics and Space Administration's (NASAs) So-

lar Maximum Mission (SMM), which provides information on the molecular number density over a wide range of solar activity conditions [Bohlin et al., 1980].

3.3.4 Thermospheric Winds

Any density difference in the atmosphere may cause winds – also in the thermosphere. The Horizontal Wind Model 2007 (HWM-07) model was created alongside with the MSIS models and is based upon gradient winds from CIRA-86 plus rocket soundings, incoherent scatter radar, medium frequency radar, and meteor radar. The observational database includes measurements from heights between 0 km and 600 km above ground [Drob et al., 2008].

In order to represent the seasonal and diurnal variations of the general circulation of the atmosphere, the model is based on a set of truncated vector spherical harmonics. Required input are the local time, geographic position, and the ap. The model returns zonal and meridional wind speeds [Drob et al., 2008]. For LEO precise orbit determination, the speed of thermospheric winds ($\boldsymbol{v}_{r,w}$) is considered by the relative velocity term (cf. Eq. 3.29) within the aerodynamic acceleration model.

3.3.5 Aerodynamics Acceleration Models

There exist various ways of modeling the acceleration due to the atmospheric density. Within this section, the aerodynamic accelerations from drag only on a sphere, and on a macro model, as well as the combined drag and lift accelerations on a macro model are introduced and compared.

Acceleration from Drag

According to Montenbruck and Gill [2005], the acceleration due to atmospheric drag for a body of a cross section A can be written as

$$\ddot{\boldsymbol{r}} = -\frac{1}{2}\, C_D\, \frac{A}{m}\, \kappa\, v_r^2\, \boldsymbol{e}_v \tag{3.28}$$

with

C_D	drag coefficient
m	total mass of spacecraft
κ	atmospheric density
$\boldsymbol{v}_r$	velocity relative to atmosphere
$\boldsymbol{e}_v$	relative velocity vector.

The drag coefficient C_D depends on the shape of the body. In POD applications, the parameter is often estimated, since the exact value is not accurately known and may also compensate potential atmospheric density deficits.

The relative velocity of the satellite to the atmosphere consists of the inertial satellite velocity in its orbit $\boldsymbol{v}_{r,I}$, the velocity caused by the co-rotating atmosphere $\boldsymbol{v}_{r,c}$ and, optionally, the velocity of the winds $\boldsymbol{v}_{r,w}$, with respect to an Earth-fixed atmosphere

$$\boldsymbol{v}_r = \boldsymbol{v}_{r,I} + \boldsymbol{v}_{r,c} + \boldsymbol{v}_{r,w} \quad . \tag{3.29}$$

In case of a plate model with i plates, the equation may be re-written as

$$\ddot{\boldsymbol{r}} = -\frac{1}{2}\,\kappa\, C_D \sum_{i=1}^{n} \Big(\gamma_i\, \frac{A_i \cos\theta_i}{m}\Big) v_r^2\, \boldsymbol{e}_v \tag{3.30}$$

with

n	total number of satellite planes
γ_i	plate specific drag coefficient
θ_i	angle between surface normal $\boldsymbol{n}_i$ and $\boldsymbol{e}_v$
A_i	area of satellite plate.

Acceleration from Drag and Lift

The following model describes the influence of air molecules on spacecraft, as formulated by Sentman [1961]. The proposed model is also elaborately discussed by Doornbos [2011].

In principal, the formulation for the aerodynamic acceleration coefficients is similar to the model for the solar radiation pressure. Photons travel at the speed of light, all in the direction from the Sun to the satellite. The gas particles have a random thermal motion that is negligible compared to the satellite velocity. The gas particles exchange

their momentum with the panel surface in two ways: the incident and the reflected or re-emitted particle flux. Both quantities contribute to the drag effect, but the lift acceleration is mainly caused by the reflected particle flux (see Figure 3.13).

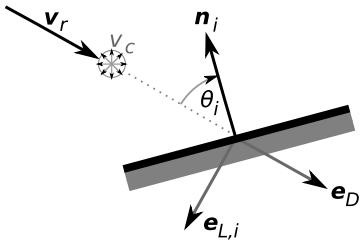

Fig. 3.13: Components of aerodynamics acting on a one-sided panel: unit vectors in direction of drag (e_D) and lift ($e_{L,i}$) with the velocity of the gas particles v_r, the thermal velocity of the gas particles v_c, and the surface unit vector n_i.

The following approach requires knowledge of the density of the single atmospheric constituents and is tested with NRLMSISE-00. For a proper description of the aerodynamic acceleration, the relative velocity vector v_r, the atmospheric temperature T, the relative mass concentrations κ_j/κ of the atmospheric constituents ($j = O_2, N_2, O, He, H, \ldots$) and their molecular masses m_j are required. The latter parameters are required to determine the random thermal velocity of the gas particles $v_{c,j}$, that is superimposed to the relative velocity v_r (see Figure 3.13).

According to Bird [1994], the thermal velocity of the atmospheric constituents j can be computed via

$$v_{c,j} = \sqrt{2\frac{R}{m_j}T} \quad . \tag{3.31}$$

The parameter R is the universal gas constant. The flow characteristics are described by the speed ratio S:

$$S_j = \frac{v_r}{v_{c,j}} \tag{3.32}$$

The aerodynamics, described by Sentman [1961] take into account the random thermal velocity of the atmospheric incident particles and assume a completely diffuse distribution of the reflected particle flux. Orbit gas-surface interaction experiments [Gregory and Peters, 1987; Moe et al., 1998] have shown, that the angular distribution above an altitude of 500 km is characterized by approximately 95 % of diffusely re-emitted particles and that the energy flux accommodation coefficient Γ is high (0.8). The energy flux accommodation coefficient Γ has been introduced by Moe et al. [2004] in Sentman's equation, which is similar to Sutton et al. [2009]. The gas-surface interaction model re-

quires the energy flux accommodation coefficient [Schaaf and Chambré, 1961], which determines whether the particles retain their mean kinetic energy (for $\Gamma = 0$) or acquire the temperature of the spacecraft surface T_w (for $\Gamma = 1$).

The following expressions define the geometry, required for Sentman's equations (cf. Eq. 3.43). The drag-direction unit vector $\boldsymbol{e}_D$ is determined via

$$\boldsymbol{e}_D = \frac{\boldsymbol{v}_r}{|\boldsymbol{v}_r|} \quad . \tag{3.33}$$

The lift- and side-acceleration-direction vector $\boldsymbol{e}_{L,i}$ is perpendicular to $\boldsymbol{e}_D$ and the plane spanned by $\boldsymbol{n}_i$ and $\boldsymbol{e}_D$:

$$\boldsymbol{e}_{L,i} = -\frac{(\boldsymbol{e}_D \times \boldsymbol{n}_i) \times \boldsymbol{e}_D}{|(\boldsymbol{e}_D \times \boldsymbol{n}_i) \times \boldsymbol{e}_D|} \quad . \tag{3.34}$$

Additionally, Sentman employs the angle between the inward normal and the drag vector

$$\theta_i = -\boldsymbol{e}_D \cdot \boldsymbol{n}_i \quad , \tag{3.35}$$

and the angle between the inward normal and the lift vector $\boldsymbol{e}_{L,i}$:

$$l_i = -\boldsymbol{e}_{L,i} \cdot \boldsymbol{n}_i \quad . \tag{3.36}$$

Finally, the drag and combined lift and side force coefficients for the satellite panel i and the atmospheric constituent j are computed following Sutton et al. [2009] and Sentman [1961] as

$$C_{G,i,j} = \left[\frac{P_{i,j}}{\sqrt{\pi}} + \theta_i \, Q_j \, Z_{i,j} + \frac{\theta_i}{2} \frac{v_{\mathrm{re}}}{v_{\mathrm{inc}}} (\theta_i \sqrt{\pi} Z_{i,j} + P_{i,j}) \right] A_i \tag{3.37}$$

$$C_{L,i,j} = \left[l_i \, G_j \, Z_{i,j} + \frac{l_i}{2} \frac{v_{\mathrm{re}}}{v_{\mathrm{inc}}} \left(\theta_i \sqrt{\pi} Z_{i,j} + P_{i,j} \right) \right] A_i \tag{3.38}$$

where

$$G_j = \frac{1}{2S_j^2} \, , \quad P_{i,j} = \frac{1}{S_j} \exp\left(-\theta_i^2 S_j^2\right) , \quad Q_j = 1 + G_j \, , \quad Z_{i,j} = 1 + \mathrm{erf}(\theta_i S_j) \quad . \tag{3.39}$$

The corresponding error function is defined as

$$\mathrm{erf}(x) = \frac{2}{\sqrt{\pi}} \int_0^x \exp(-y^2) \mathrm{d}y \quad . \tag{3.40}$$

The last term of Equations 3.37 and 3.38 is proportional to the ratio of the velocity of the re-emitted particles $\boldsymbol{v}_{\mathrm{re}}$ the incoming particles $\boldsymbol{v}_r$. Koppenwallner [2009] and Llop et al. [2015] modified the expression of Moe and Moe [2005] as a function of the accommodation coefficient Γ and the wall temperature T_w:

$$\frac{v_{\mathrm{re}}}{v_{\mathrm{inc}}} = \sqrt{\frac{1}{2}\left[1+\Gamma\left(\frac{4RT_w}{m_j v_{\mathrm{inc}}^2}-1\right)\right]} \quad . \tag{3.41}$$

Equation 3.41 is dimensionless. The wall temperature introduces another uncertainty in the computations of the gas-surface interaction. Fortunately, the sensitivity to this parameter is quite low. Typically, the accommodation coefficient for satellite surfaces is in the range between 0.90 and 1.00 [Doornbos, 2011]. For the present study, the accommodation coefficient is set to 0.97, ant the wall temperature is set to 300 K.

For a satellite plate model with i plates and the consideration of j atmospheric constituents, the coefficient including drag and lift is computed via

$$\boldsymbol{C}_a = \sum_i \sum_j \frac{\kappa_j}{\kappa}\left(C_{G,i,j}\,\boldsymbol{e}_D + C_{L,i,j}\,\boldsymbol{e}_{L,i}\right) \quad . \tag{3.42}$$

Considering this coefficient in the equation for the aerodynamic acceleration, one ends up with

$$\ddot{\boldsymbol{r}} = C_{\mathrm{D}}\boldsymbol{C}_a \frac{1}{m}\frac{1}{2}\kappa\|\boldsymbol{v}_r\|^2 \quad . \tag{3.43}$$

C_{D} is the dimensionless aerodynamic acceleration coefficient that is estimated freely in the RDOD process.

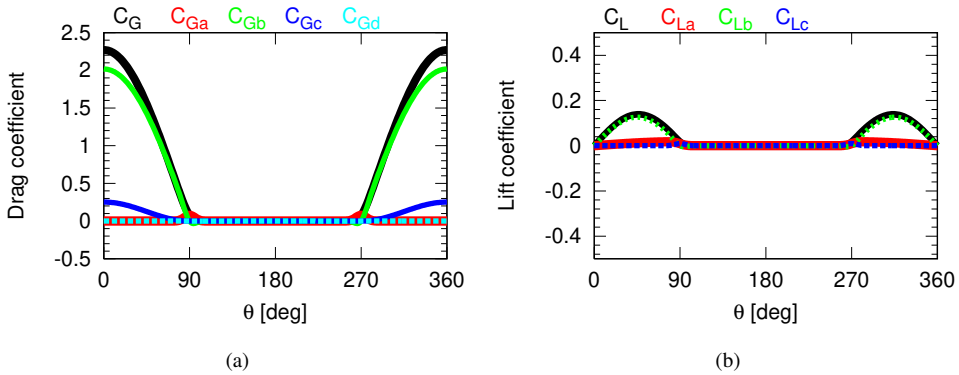

Fig. 3.14: Summands of (a) drag and (b) lift scaling coefficients for different attack angles θ.

The relation between the attack angle θ and the coefficients C_G and C_L is shown in Figure 3.14 for different angles and components of the scaling coefficient in Equation 3.37 for drag

$$C_{Ga} = \frac{P_{i,j}}{\sqrt{\pi}} \tag{3.44}$$

$$C_{Gb} = \theta_i \, Q_j \, Z_{i,j} \tag{3.45}$$

$$C_{Gc} = \frac{\theta_i}{2} \frac{v_{\text{re}}}{v_{\text{inc}}} \theta_i \sqrt{\pi} Z_{i,j} \tag{3.46}$$

$$C_{Gd} = \frac{\theta_i}{2} \frac{v_{\text{re}}}{v_{\text{inc}}} P_{i,j} \quad , \tag{3.47}$$

and Equation 3.38 for lift:

$$C_{La} = l_i \, G_j \, Z_{i,j} \tag{3.48}$$

$$C_{Lb} = \frac{l_i}{2} \frac{v_{\text{re}}}{v_{\text{inc}}} \theta_i \sqrt{\pi} Z_{i,j} \tag{3.49}$$

$$C_{Lc} = \frac{l_i}{2} \frac{v_{\text{re}}}{v_{\text{inc}}} P_{i,j} \quad . \tag{3.50}$$

The figure shows the complete term and the contribution of the single components. Both, the lift and drag coefficient are dominated by the second term ($_b$), which involve the attack angle and the error function are involved. The drag contribution in that term is directly proportional to $2\cos\theta$, whereas the lift component to $0.15\sin(2\theta)$. The first drag term C_{Ga} mainly contributes to edges where θ is close to 90 °.

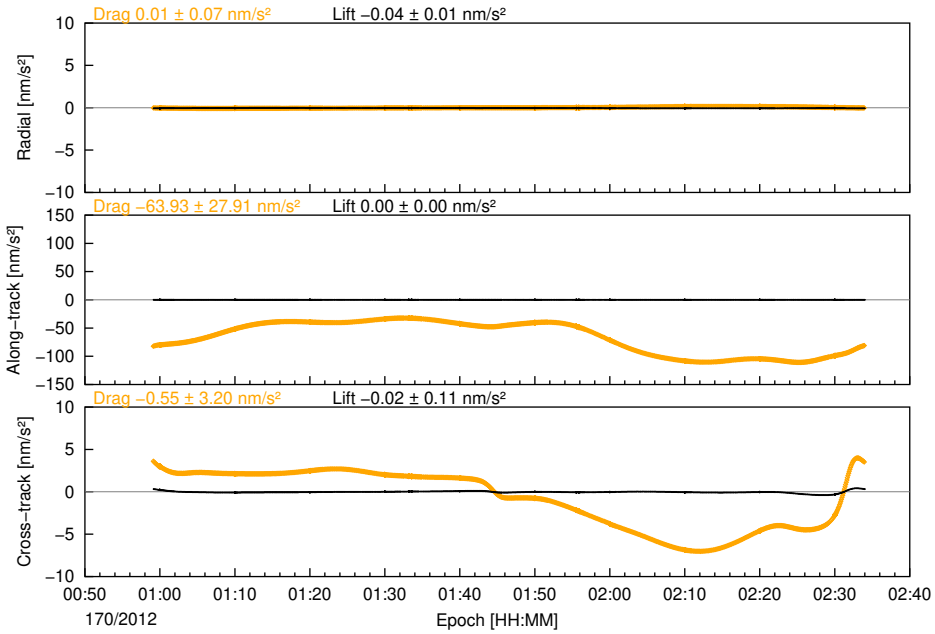

Fig. 3.15: Aerodynamic accelerations due to drag and lift on TerraSAR-X plate model.

Figure 3.15 shows the acceleration on TerraSAR-X due to drag and lift over a single orbit in nominal attitude as computed with the NRLMSISE-00 density model and the Sentmen model for a unit value of the C_D scale factor. Drag is the dominating part, which acts in along-track and, to a much lower extent, in cross-track direction. The effect of lift is almost negligible, only a slight contribution in radial and cross-track direction can be observed.

4

Non-Gravitational Forces – Assessment

4.1 Methodology

Within this chapter, the impact of refined satellite dynamic models on the estimated, reduced-dynamic orbit solutions is assessed. For this purpose, first the model accelerations are analyzed. Subsequently, the models are applied in reduced-dynamic orbit determination. The detailed performance analysis addresses the question how the stepwise dynamic model improvements influence the orbit solutions, and the empirical accelerations. Additional data and models, which are required for reduced-dynamic orbit determination, have been introduced in Section 2.2.2.

All combinations and associated models are shown in Table 4.1. For transparency, an identification (ID) number is introduced. The PSOs correspond to the operationally generated orbit solutions of TSX-1/TDX-1 that were determined employing a cannon-ball model for SRP and drag modeling. The following IDs consider different gravitational and non-gravitational force models in combination with the satellite macro-model in a consistent, upwards-oriented order. The modifications are briefly explained as follows:

Table 4.1: Overview of selected auxiliary, gravitational, and non-gravitational models describing the satellite dynamics.

	PSO	ID1	ID2	ID3	ID4	ID5	ID6	ID7	ID8	ID9
Gravitation										
GGM01S+CSR3.0	✓									
GOCO03s+FES2004		✔	✓	✓	✓	✓	✓	✓	✓	✓
Atm.density										
Jacchia71G	✓	✓								
DTM 2012			✔							
NRLMSISE-00				✔	✓	✓	✓	✓	✓	✓
Aerodynamic										
Drag cannon-ball	✓	✓	✓	✓						
Drag macro					✔					
Sentman macro						✔	✓	✓	✓	✓
Radiation										
SRP cannon-ball	✓	✓	✓	✓	✓	✓				
SRP macro							✔	✓	✓	✓
ERP macro								✔	✓	✓
Wind										
HWM-07									✔	
GPS Ambiguity										*(see Chapter 5)*
Float	✓	✓	✓	✓	✓	✓	✓	✓	✓	
Integer										✔

The red ticks show the updates compared to the previous ID

ID1 corresponds to an updated version of the PSOs. The gravity field Gravity Observation COmbination 03s (GOCO03s) up to degree and order 100 in combination with FES2004 are considered.

ID2/3 consider an updated atmospheric density model, and

ID4/5 an enhanced aerodynamic acceleration model.

ID6/7 compares different solar and Earth radiation models,

ID8 shows the influence of an atmospheric wind model on the RDOD solutions.

ID9 finally evaluates the influence of GPS integer ambiguity fixing, addressed in Chapter 5.

Modeled accelerations are analyzed for TerraSAR-X, TanDEM-X and, in addition, Swarm-C. All resulting orbit solutions are assessed by means of the performance indicators, introduced in Chapter 2.3.

4.2 Accelerations

Within this section, an assessment of the non-gravitational accelerations is given first. Subsequently, scaling parameters and empirical accelerations are analyzed, both of which represent performance indicators obtained within the RDOD process.

4.2.1 Radiation Models

Solar and Earth radiation pressure are two radiation models, which have been introduced in Section 3. Combined with different plate model sophistications, their influence is assessed below.

Solar Radiation Pressure

In order to analyze the accelerations of solar radiation pressure, accelerations from the cannon-ball and plate model are compared for TerraSAR-X and Swarm-C. For TerraSAR-X and TanDEM-X, the cannon-ball SRP area is set to the $13.00\,\mathrm{m}^2$, which is the default value employed in the operational POD. The SWC cannon-ball area is set to $5.00\,\mathrm{m}^2$. The selected macro models are available in Tables 3.1 and 3.3. The applied C_R scale factor is fixed to 1.00 for comparison.

For TSX-1, the SRP model exhibits peak-to-peak amplitudes up to $40\,\mathrm{nm/s}^2$. Figure 4.1 shows corresponding time series, including the umbra/penumbra phase. The cross-track component shows an almost constant acceleration of $40\,\mathrm{nm}/s^2$, which is attributed to the dusk-dawn orbit. For the radial and along-track components, the magnitude of the macro-model accelerations is smaller by about $5\,\mathrm{nm/s}^2$ compared to the cannon-ball model, when the spacecraft is in sunlight. In radial direction, a maximum amplitude is observed when the spacecraft crosses the equator.

Accelerations on Swarm-C are shown in Figure 4.2 based on the cannon-ball and macro models. During the selected period, SWC was orbiting the Earth on a dusk-dawn orbit. The peak-to-peak accelerations exhibit up to $60\,\mathrm{nm/s}^2$ in all RTN components. Due to the dusk-dawn orbit, there is a constant acceleration in cross-track direction with pronounced variations in case of the macro model. The maximum acceleration in cross-

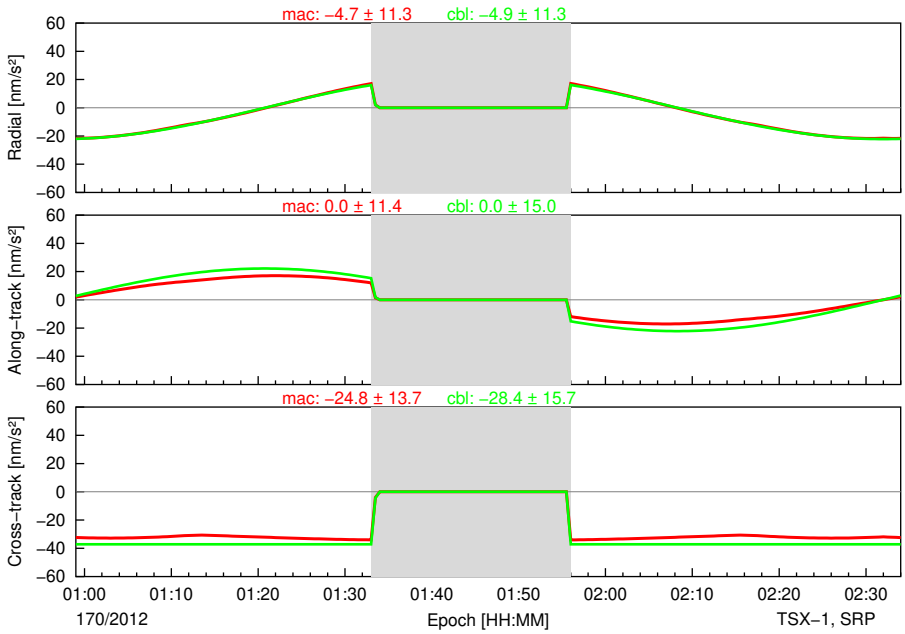

Fig. 4.1: Accelerations due to solar radiation pressure on TerraSAR-X for one revolution. Red and green colors refer to the macro-model (mac) and cannon-ball (cbl) solutions. The umbra/penumbra passage is indicated in gray.

track direction occurs at the equator, the minimum acceleration at the poles (and during eclipses).

In comparison to TerraSAR-X, the increase is explained by the huge solar plates (approx. 16 % larger), and different optical properties. Both missions show non-zero mean values in the cross-track component, which is caused by the dusk-dawn orbit. Specifically for Swarm-C, the macro model shows pronounced variations in cross-track direction. The cannon-ball model shows enlarged accelerations, which is attributable to the constant effective surface. Drops in the series are caused, when the satellite enters the Earth shadow.

The presented approach does not take into account a thermal model of the spacecraft body. Such thermal models require knowledge of the temperature diffusion in the spacecraft's interior, and the way the energy is emitted (active/passive) [Adhya, 2005]. Additional information like the knowledge on the emissivity requires input from the satellite manufacturer, and the thermal venting does not necessarily distribute the radiation symmetrically, which makes a proper model even more complicated [Stefanis et al., 2015;

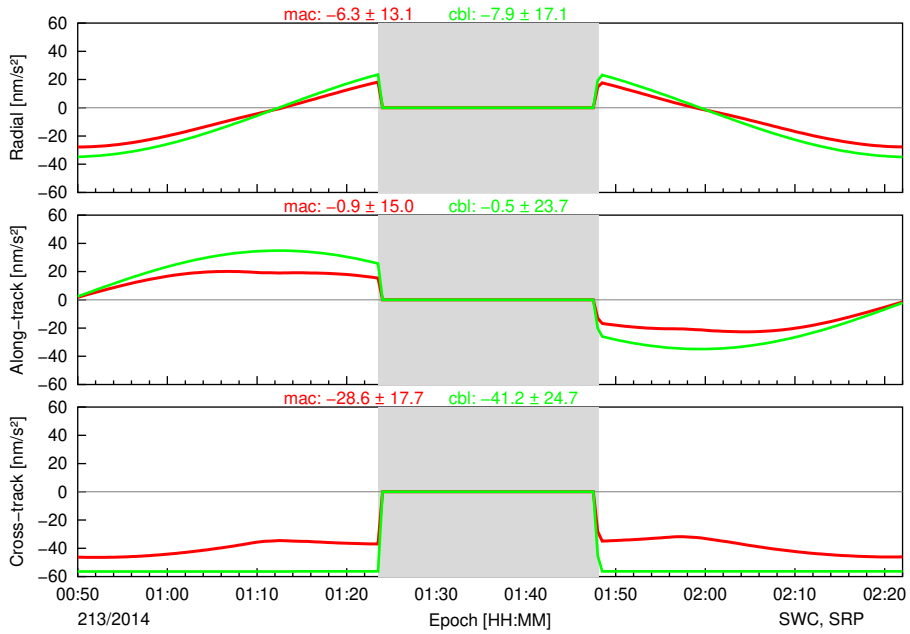

Fig. 4.2: Accelerations due to solar radiation pressure on Swarm-C for one revolution. Red and green colors refer to the macro-model (mac) and cannon-ball (cbl) solutions. The umbra/penumbra passage is indicated in gray.

Ziebart et al., 2005]. For the Jason-1 and Jason-2 spacecraft, Cerri et al. [2010] states a maximum of 100 W due to thermal flux, which is equivalent to $0.4\,\mathrm{nm/s^2}$.

As mentioned in the introduction of this section, the solar irradiance of $1{,}367\,\mathrm{W/m^2}$ at a normed distance of 1 AU, which is the input quantity to radiation forces related to the Sun, is considered as a constant [McCarthy, 1996]. Kopp and Lean [2011] state a value of $1{,}360.8$, is a $0.6\,\%$ difference compared to the value, recommended by McCarthy [1996]. If not normed to the distance of 1 AU, annual variations of that constant amount to $\pm 3.3\,\%$ and are caused by the small eccentricity of the Earth orbit. This effect is compensated, since the power is scaled by the distance spacecraft-Sun. Another variation is caused by the 9–14 years solar cycle (cf. number of Sunspots in Figure 3.12). Kopp and Lean [2011] have shown that the solar electromagnetic radiation is varying over one solar 11-years cycle by roughly $2\,\mathrm{W/m^2}$, which is attributable to changes in the Sun's activity. The values are known from measurements like from the Solar and Helospheric Observatory (SOHO). The scaling factor, which is applied directly to the non-gravitational force models, can directly compensate such changes.

Table 4.2: Comparison of TerraSAR-X orbit solutions with different macro model sophistications (DOY 100/2012). The orbit comparison selects ID6 as basis, the numbers starting with a hash correspond to the plate numbers available in Table 3.1. No Re-emission (NoRe) for all plates is considered in the last case. All values: $\bar{x} \pm \sigma_x$.

ID	Scal. coeff.	Empirical acc. [nm/s^2]			Ephemeris comparison [mm]		
	C_R	radial	along-track	cross-track	radial	along-track	cross-track
ID 6	1.1	0.1 ± 0.2	-0.6 ± 3.9	0.0 ± 7.6	0 ± 0	0 ± 0	0 ± 0
#7	3.2	0.1 ± 0.5	2.5 ± 8.7	-0.3 ± 9.3	0 ± 3	0 ± 4	37 ± 1
#1	3.0	0.0 ± 0.2	-0.1 ± 3.9	0.1 ± 7.2	-1 ± 2	0 ± 3	-18 ± 1
#7+#1	2.5	0.1 ± 0.1	-0.1 ± 3.7	0.1 ± 7.8	-1 ± 2	0 ± 2	-11 ± 1
NoRe	1.4	0.1 ± 0.2	-0.6 ± 3.9	0.0 ± 7.5	0 ± 0	0 ± 0	3 ± 0

Macro Model Sophistication and Solar Radiation Pressure Satellite macro models are composed out of several plates. Which level of sophistication is required to improve the derived orbit solutions? For assessing the impact, TSX-1 is chosen together with different macro model plates, indicated by Table 3.1 (page 35). The considered orbit parameterization corresponds to ID6, only for SRP different combinations of macro model plates are selected: only front plate (#7), only solar array plate (#1), combined (#7+#1), and a macro model without any re-radiation capabilities are considered. All resulting solutions are compared to ID6 and analyzed by means of direct comparison of the orbit solutions, scaling coefficients and empirical accelerations. DOY 100/2012 is selected as basis for this analysis. A comparison of the results is available in Table 4.2, corresponding time series of the ephemeris comparison in Figure 4.3.

Using the presented macro model, a mis-modeled shape clearly increases the corresponding scaling parameter, and the empirical accelerations. In #7, only the front plate is considered for SRP, which causes pronounced empirical accelerations in along-track direction. The a priori force model considers no acceleration in direction of the incident Sun radiation, rectangular to the orbital plane. Compared to the real orbit (with $a_n \approx 25\,\mathrm{nm/s^2}$; cf. Figure 4.1), this causes, according to [Montenbruck et al., 2017]

$$\Delta a_N = \frac{GM_\oplus}{r^2} \cdot \frac{\Delta r_N}{r} \tag{4.1}$$

a lateral offset of 2 cm. In addition, no empirical accelerations are estimated in the present case, which can compensate this effect. The resulting orbit solution is shifted by roughly 4 cm in cross-track direction, which corresponds to the $25\,\mathrm{nm/s^2}$ in cross-track direction. The solar array plate (#1) is oriented in cross-track direction, and provides the dominating SRP contribution of all plates in the given dusk-dawn geometry. The

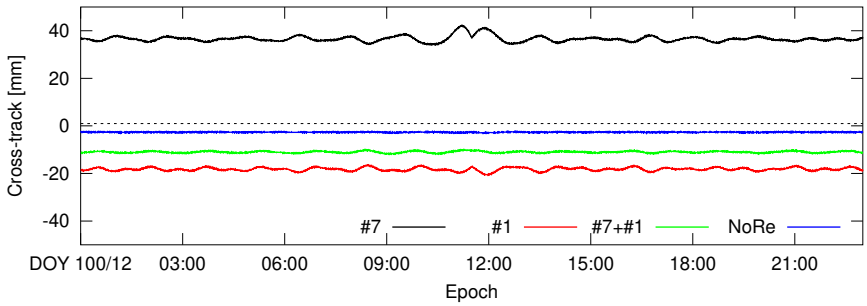

Fig. 4.3: Different TSX-1 macro model plates and cross-track ephemeris comparison of the resulting solutions, all compared to ID 6 as reference.

resulting solution is shifted by −2 cm in cross-track direction. Taking both the front and the solar plate into consideration, the cross-track differences reduces to 1 cm. For all comparisons, the solar radiation scaling parameter C_R is clearly above 1, which corresponds to the mis-modeled shape. The last test disables any re-radiation by the satellite plates. The macro model of TerraSAR-X considers such a re-radiation for all except for the solar array plate. The caused shift of the orbit solutions is at a magnitude of 3 mm in cross-track direction, whereas the empirical accelerations are not affected in a notable matter. The associated C_R coefficient increases by 20 % and, therefore, partly compensates the reduced acceleration caused by the neglected re-emission. For TerraSAR-X, the major part of the SRP acceleration is caused by the solar arrays, whereas the other plates just have minor impact on SRP.

On one hand, the estimation of scaling factors and empirical accelerations largely eliminates wrong assumptions (wrong areas or optical coefficients) in the a priori models. Thus, the associated scaling parameters may become unphysical large. Moreover, specific illumination geometries cause an erroneous modeled acceleration, which can not be compensated by the GPS observations and result in orbit errors of several cm.

Earth Radiation Pressure

The magnitude of accelerations due to Earth radiation pressure on TerraSAR-X and Swarm-C are shown in Figure 4.4, and 4.5, respectively. Earth radiation mainly acts in the spacecraft's radial direction, depends on the reflectivity of the Earth below, and decreases with increasing distance from Earth. For both missions, the impact on along- and cross-track component are small. The accelerations in cross-track direction are

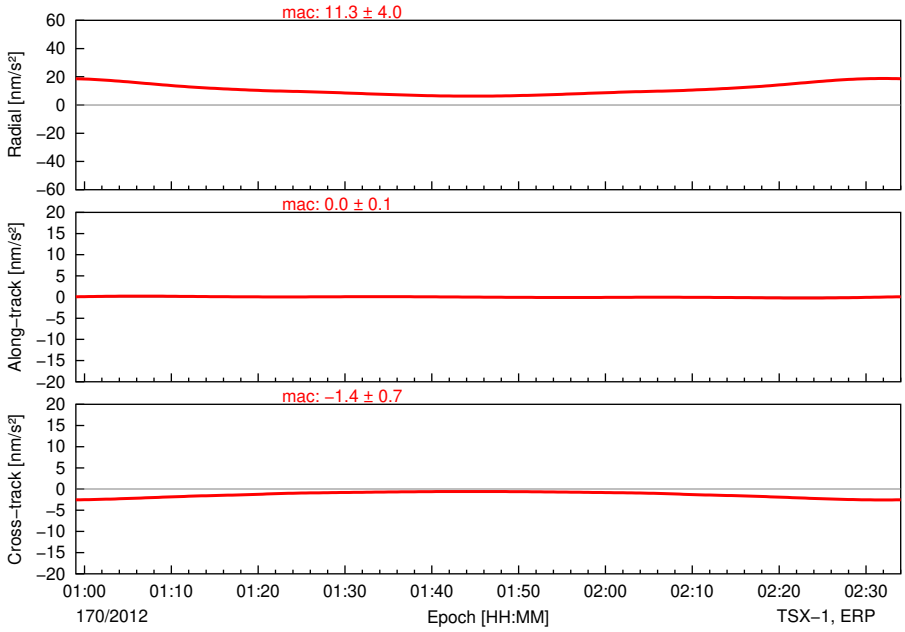

Fig. 4.4: Magnitudes of acceleration due to earth radiation pressure on TerraSAR-X.

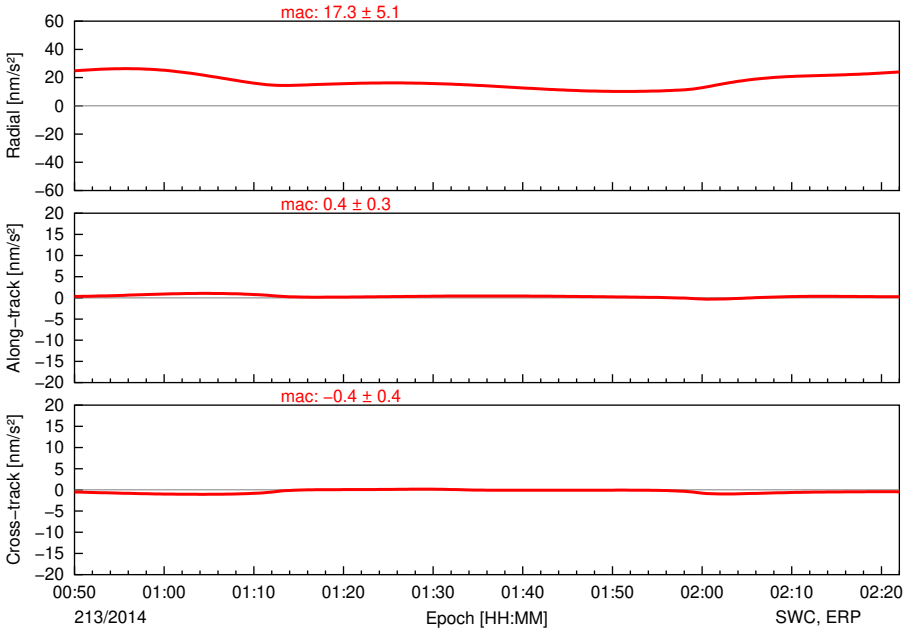

Fig. 4.5: Magnitudes of acceleration due to earth radiation pressure on Swarm-C.

larger than in the along-track component and exhibit a non-zero mean value, which is attributable to the dusk-dawn orbit.

For TerraSAR-X, the mean acceleration of 11 nm/s^2 (altitude 514 km) is slightly smaller than for Swarm-C with 17 nm/s^2 (450 km), which is attributable to the difference in altitude. For the investigated LEO spacecraft, the acceleration of ERP is approximately one third of the direct SRP effect. ERP shows a maximum of acceleration at the poles, where the Earth reflectivity is high.

4.2.2 Aerodynamics

In Section 3.3, different satellite aerodynamic acceleration models, and atmospheric density models have been introduced. An assessment of these atmospheric density models, as well as modeled aerodynamic accelerations is given below.

Density Models

Since the aerodynamic accelerations, and the related atmospheric density plays a major role in orbit determination of LEO spacecraft, a comparison of the model densities is of vital importance. For this purpose, DOY 170/2012 and the altitude of TerraSAR-X have been selected, and the corresponding density values plotted on a global map. Figure 4.6 compares the atmospheric densities from DTM 2012, Jacchia-71G, and NRLMSISE-00 by means of global density maps at an altitude of 514 km. Corresponding, average values are available in Table 4.3.

The density differences between NRLMSISE-00 and Jacchia-71G are in the approximate range of $\pm 1.0 \times 10^{-13}$ kg/m^3, whereas the DTM 2012 to Jacchia-71G differences only show an amplitude of $\pm 0.5 \times 10^{-16}$ g/m^2. The derived magnitudes of density are a bit lower for NRLMSISE-00 compared to the other atmospheric density models. This fact is known from literature since NRLMSISE-00 slightly under-estimates the hydrogen concentration and, therefore, the density [Picone et al., 2002].

The sectoral pattern is an indicator for differences in the coefficients for describing the atmospheric density. In addition, Figure 4.6 shows the day-night terminator. As TerraSAR-X is orbiting on a dusk-dawn orbit, which is close to this terminator, the trajectory does not cross regions with extreme density differences. The pronounced peak

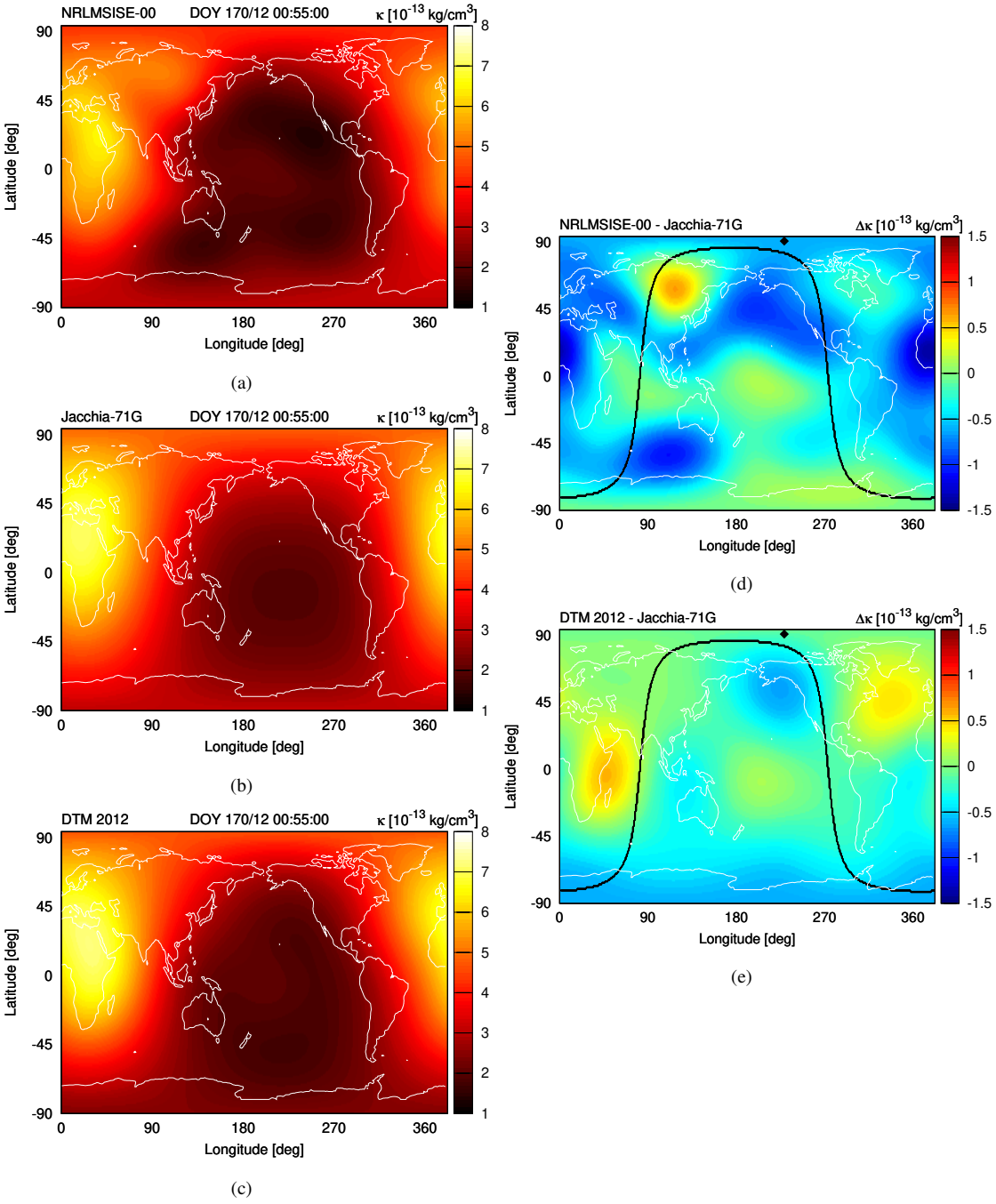

Fig. 4.6: Global density maps (DOY 170/12) in an altitude of 514 km. Position of TerraSAR-X indicated by the black square, the terminator is shown by the black line. (a) NRLMSISE-00 (b) Jacchia-71G (c) DTM 2012 (d) NRLMSISE-00 minus Jacchia-71G (e), and DTM 2012 minus Jacchia-71G.

Table 4.3: Mean densities of several atmospheric density models, and the percentage difference, compared to Jacchia-71G. DOY 170/12, altitude of TerraSAR-X.

Model	$\kappa[10^{-13}\ \mathrm{kg/cm^3}]$	$\Delta\kappa\ [\%]$
Jacchia-71G	3.82	
DTM 2012	3.65	4.5
NRLMSISE-00	3.40	11.0

in the difference map NRLMSISE-00-Jacchia-71G in Figure 4.6 is located on the night side of the Earth. In summer (DOY 170) the north pole is illuminated by the Sun.

Table 4.3 shows the mean densities and percentage density differences of Jacchia-71G to DTM 2012, and NRLMSISE-00. The difference is doubled by utilization of NRLMSISE-00, which is also visible from Figure 4.6, but depends on the chosen reference. In LEO, the comparison of different density models exhibits differences up to 11 %. In addition, comparisons of global density maps show density variations along with the terminator, which is close to the dusk-dawn orbit of TerraSAR-X.

For evaluating a suitable atmospheric density model in terms of RDOD, the estimated scaling parameter of the drag formula is a suited measure. Table 4.4 shows the correlation of the drag scaling coefficient C_D from the RDOD process with the input quantities $\mathrm{F}_{10.7}$ and kp. A small correlation between the drag scaling factor and the $\mathrm{F}_{10.7}$ proxy/kp index indicates a better response of the atmospheric model to changes in that values. According to these findings, the C_D scaling parameter resulting from NRLMSISE-00

Table 4.4: Correlation between drag scaling coefficient C_D of TSX-1 and estimated in the RDOD, daily $\mathrm{F}_{10.7}$, and daily mean geomagnetic kp index. The analysis period covers the year 2012.

Model	$\mathrm{F}_{10.7}$	$\mathrm{k_p}$
NRLMSISE-00	−0.34	−0.01
Jacchia-71G	0.01	−0.36
DTM 2012	−0.24	−0.23

orbit solutions shows the smallest correlation coefficient with the $\mathrm{F}_{10.7}$ proxy, followed by the results obtained with DTM 2012. For the geomagnetic ap index, smallest correlation coefficients are obtained for Jacchia-71G and DTM 2012 solutions.

Acceleration Models

Three models describing aerodynamic accelerations have been introduced. The first, shown in Equation 3.30 considers only the fixed, front plate cannon-ball (cbl). The second model in Equation 3.28 considers the effective cross-section for atmospheric drag as derived from a macro (mac) model, as well as the actual orbit and attitude. The third and last model considers drag and lift, combined with the Sentman equations (cf. Equation 3.43; snt). For all comparisons, the atmospheric density model is NRLMSISE-00. Aerodynamic accelerations on the TerraSAR-X spacecraft are shown in Figure 4.7, for

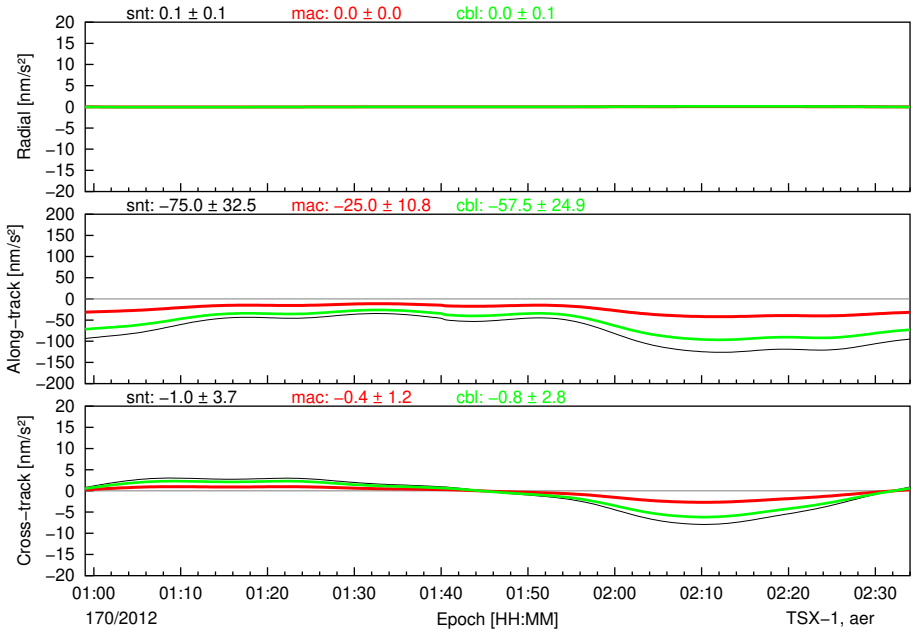

Fig. 4.7: Comparison of aerodynamic accelerations models for TerraSAR-X. Black refers to the Sentman model, red to the macro, and green to the cannon-ball model.

radial, along- and cross-track component separately. The Sentman (snt) model exhibits pronounced amplitudes in all components. A peak amplitude of 100 nm/s^2 is observed in along-track direction. The geometrical macro model shows the smallest contributions. Compared to the cbl approach, the Sentman model produces a similar trend, but the amplitudes are more pronounced. Major differences are visible when the spacecraft crosses polar regions around epochs 01:15, and 02:10 in Figure 4.7. The obvious difference between the snt and both, the mac and cbl model is

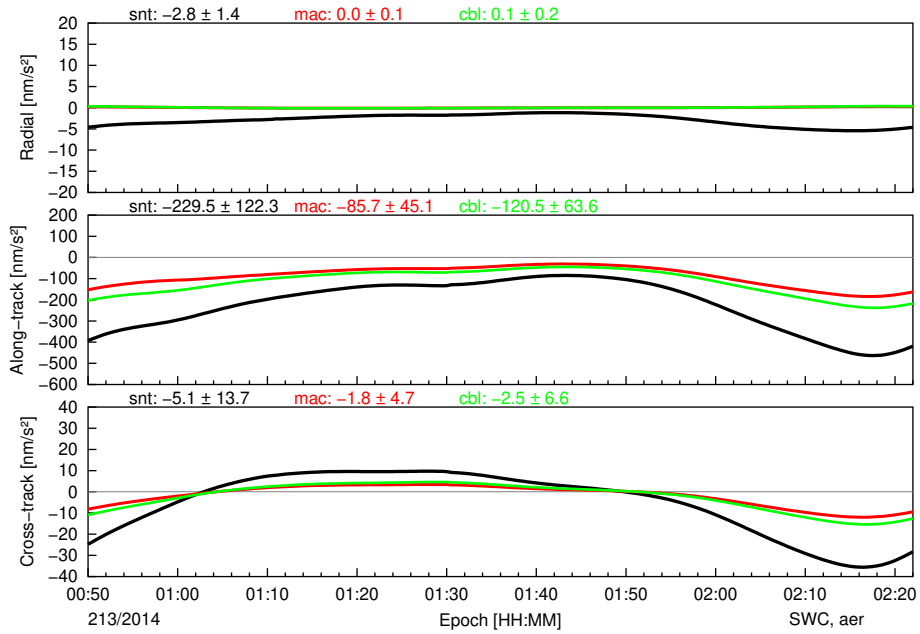

Fig. 4.8: Comparison of accelerations due to aerodynamic accelerations on Swarm-C for different models.

Aerodynamic accelerations on the spacecraft Swarm-C are depicted in Figure 4.8. The cannon-ball and macro model exhibit less amplitudes in all three components. In along-track component, the Sentman acceleration is enlarged by factor 2. In cross-track, the snt model shows peak amplitudes, when the spacecraft passes the polar regions. Within these regions, the snt model exhibits maximum amplitudes up to $-30\,\mathrm{nm/s^2}$.

A comparison between Swarm-C and TerraSAR-X shows different magnitudes of aerodynamic accelerations, which is attributable to the altitude and satellite shape. An explanation of this difference is the typical drag scaling factor of 2.3 for the cannon-ball and macro model. In case of the Sentman model, the corresponding value is set to 1, which results in the difference between the Sentman, and the cbl/mac models. For Swarm-C, the magnitudes of aerodynamic accelerations are larger compared to TSX-1, which is attributable to the satellite shape and the orbit altitude.

Since any of the aerodynamic acceleration models is sensitive to the relative velocity of the spacecraft with respect to the atmosphere $\boldsymbol{v}_r$, and since this vector is aligned in along-track direction, major differences are visible in along-track direction. The mac model as well as the Sentman model consider also plates, which are not considered by

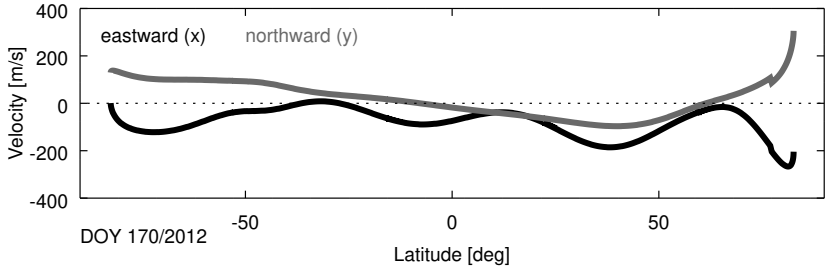

Fig. 4.9: HWM-07 wind velocities at position of TerraSAR-X (DOY 170/12, 1:00 UTC).

the simple cbl model. Moreover, the macro models show a short-scale variability in the magnitudes plot, which is caused by changes in the attitude.

Thermospheric Winds The presence of thermospheric winds is considered by HWM-07 and the resulting accelerations on TerraSAR-X are depicted in Figure 4.9. It clearly shows a pronounced contribution in eastward direction, which relates to the location of the orbit along the terminator, where illumination differences cause temperature gradients and, finally, wind.

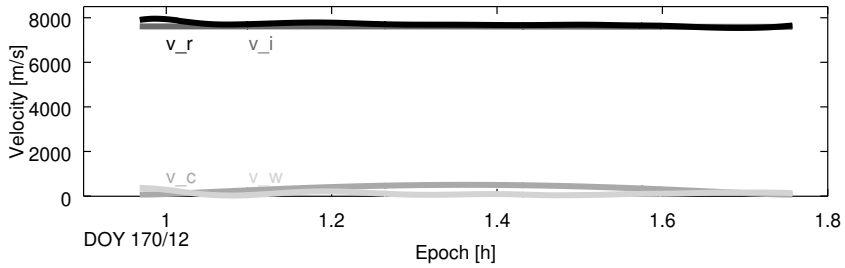

Fig. 4.10: Magnitudes of inertial velocity v_i, velocity due to co-rotation of the atmosphere v_c, and wind velocity v_w, which are to compute the spacecraft velocity relative to the atmosphere v_r.

Wind velocities are considered in the spacecraft velocity, relative to the atmosphere (cf. Equation 3.29). An overview of all components is shown in Figure 4.10. Obviously, the contribution of the wind speeds (v_w = 200 m/s) is rather small compared to the inertial velocity (v_i = 7.7 km/s). Magnitudes of acceleration due atmospheric winds are at 2.5 nm/s^2 for TSX-1 and 10 nm/s^2 for SWC. In accordance with the atmospheric density, the magnitude of acceleration due to atmospheric winds depends on the attitude of the spacecraft.

Finally, the aerodynamic acceleration model is supported by considering the atmospheric winds (cf. Eq. 3.29). As already stated in the corresponding section, the effect of cross-winds is supposed to be very small due to the small magnitude of the modeled wind speeds (see Fig. 4.9). A direct orbit comparison of two solutions with and without wind models shows a mean bias of 0.5 mm in cross-track direction, which corresponds to the wind velocities in eastward direction.

4.2.3 Empirical Accelerations

Empirical accelerations compensate potentially mis- or un-modeled accelerations in a reduced-dynamic approach. To assess the quality of different a priori force models, the statistical properties of estimated empirical accelerations have been analyzed for nine different types of TerraSAR-X POD solutions over a four years period. The force models employed in each solution have previously been described in Table 4.1. Statistics for the resulting estimates of scale factors and empirical accelerations are summarized in Table 4.5.

Table 4.5: TerraSAR-X orbit solutions: RDOD scaling parameters and empirical accelerations (based on series of daily mean and daily RMS values; $\bar{x} \pm \sigma_x$). 2012–2015.

ID	Scal. coeff.			Emp. acc. (daily mean) [nm/s^2]			Emp. acc. (daily RMS) [nm/s^2]		
	C_D	C_E	C_R	R	T	N	R	T	N
PSO	1.29±0.23	–	0.90±0.32	0.3±0.1	0.3±1.2	−0.2±0.4	0.6±0.2	11.6±4.6	13.1±2.6
1	1.28±0.23	–	0.88±0.48	0.1±0.0	0.1±1.1	−0.1±0.2	0.4±0.2	10.3±4.9	8.4±1.5
2	1.29±0.21	–	0.90±0.37	0.1±0.0	0.0±1.2	−0.1±0.2	0.3±0.1	8.4±4.5	8.3±1.4
3	1.30±0.22	–	0.92±0.30	0.1±0.0	0.0±0.8	−0.1±0.1	0.3±0.1	7.2±3.6	8.3±1.4
4	1.19±0.21	–	1.02±0.33	0.1±0.0	−0.1±0.8	−0.1±0.1	0.3±0.1	7.2±3.6	8.3±1.4
5	1.00±0.17	–	0.92±0.30	0.1±0.0	0.0±0.8	−0.1±0.1	0.3±0.1	7.3±3.6	8.4±1.4
6	1.00±0.17	–	1.06±0.32	0.1±0.0	0.0±0.8	−0.1±0.1	0.3±0.1	7.3±3.6	8.4±1.4
7	1.00±0.17	1.00±0.00	1.13±0.32	0.1±0.0	0.1±0.8	0.0±0.1	0.3±0.1	7.3±3.6	8.4±1.4
8	1.00±0.17	1.00±0.00	1.11±0.32	0.1±0.0	0.0±0.8	0.0±0.1	0.3±0.1	7.3±3.7	8.4±1.4

The PSO solutions exhibit no significant *bias* in any component, but a *standard deviation* of 12 nm/s^2, obtained from the 2012–2015 period. In ID1, the gravity field, and the ocean tide model are updated by state-of-the-art models. The daily mean accelerations, as well as daily RMS accelerations show a significant reduction in all components. The cross-track standard deviation is reduced by 5 nm/s^2, the along-track by 1 nm/s^2. The change is mainly induced by the replaced gravity field, the updated ocean model has no significant impact.

Modeling aerodynamic accelerations requires atmospheric density models. Therefore, IDs 2 and 3 correspond to orbit solutions with different atmospheric density model (DTM 2012 and NRLMSISE-00). Replacing the Jacchia-71G model with DTM 2012 leads to a substantial standard deviation decrease of 2 nm/s^2 in along-track.

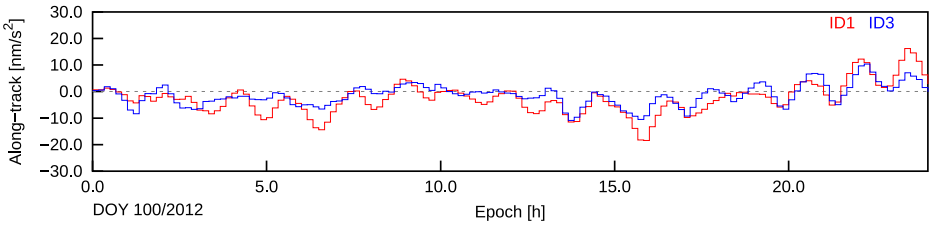

Fig. 4.11: Comparison of along-track empirical accelerations from solutions with Jacchia-71G (ID1) and NRLMSISE-00 (ID3) atmospheric density models.

A further update from DTM 2012 to NRLMSISE-00 in ID3 leads to further 1nm/s^2 reduction in along-track. Compared to the precise science orbits, updating the gravitational and non-gravitational models by state-of-the-art ones reduces the standard deviation of the empirical accelerations by 4 nm/s^2 in along, and 5 nm/s^2 in cross-track. Aside from the long-term statistics, the benefit of improved density models can also be recognized from reduced sub-daily variations of the estimated empirical accelerations as shown in Figure 4.11. However, any further model updates do not significantly influence the empirical accelerations.

4.2.4 Estimated Scale Factors

Within the applied RDOD approach, the scaling factors are separately estimated for aerodynamic, Earth, and solar radiation pressure. However, the C_E scaling factor needs to be constrained to 1. This is due to the fact that ERP acts mainly in radial direction and therefore modifies the relation between orbital period T and orbital radius r imposed by Kepler's 3rd law. As a consequence, a radial PCO error Δr can be fully compensated by an empirical acceleration

$$\Delta a_R = 3\left(\frac{2\pi}{T}\right)^2 \Delta r \tag{4.2}$$

in radial direction (see Montenbruck et al. [2017]), or, equivalently, a mean radial ERP contribution. At LEO altitudes, a 1 cm PCO uncertainty thus translates into a 30 nm/s^2 uncertainty of the radial acceleration, which is of the same order of magnitude as the

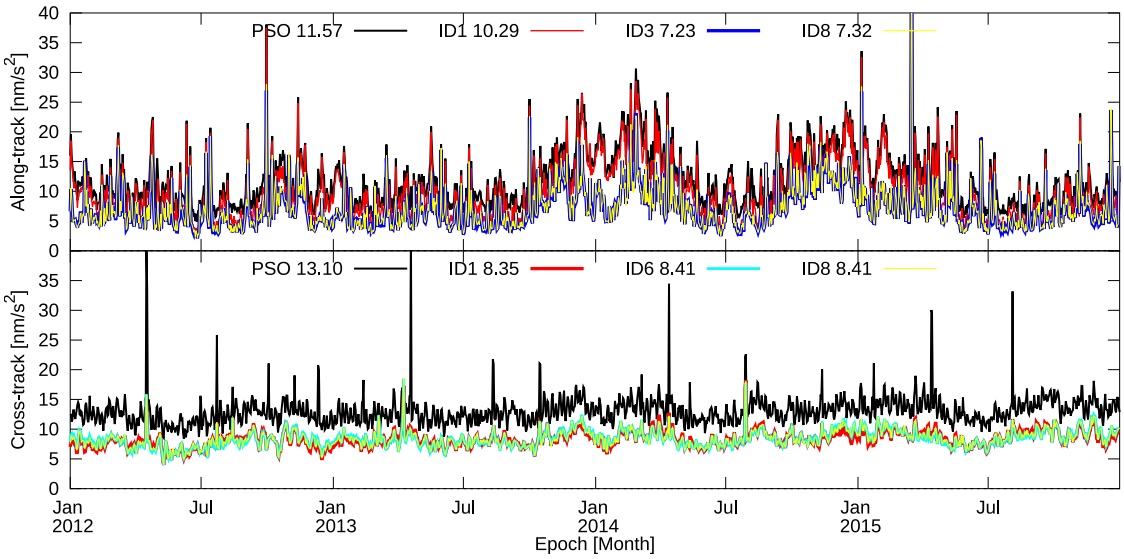

Fig. 4.12: Selected series of empirical accelerations (daily RMS) for TerraSAR-X. For each solution, the mean RMS value of the estimated empirical accelerations (in nm/s^2) is given next to the corresponding label.

ERP itself. In view of prevailing uncertainties in the PCO knowledge, both C_E and radial empirical accelerations are therefore tightly constrained in the POD process to avoid unrealistic estimates of these quantities.

Contrary to the empirical accelerations where an atmospheric density model update causes significant changes in the empirical accelerations, the scaling parameters are not affected in a notable way. However, model changes of the area, which is exposed to air molecules, affect the corresponding scaling parameter C_D. In an ideal case, the scaling parameter is expected to be one. The single front plate, geometrical macro model, or complex gas-surface interactions are represented by IDs 4, 5, and 8. The PSO and solutions <4 consider a fixed cross-sectional area as front plate, which is supposed to air molecules and, therefore, contributes to the aerodynamic acceleration. In solution ID4, this front plate model is replaced by the variable size macro model formulation, stated in Equation 3.30. Triggered by this replacement, the mean C_D values are reduced by 10 % to 1.2 (see Fig. 4.13). The reduction indicates that the variable cross-sectional area better represents the real shape, since it considers the spacecraft's attitude. The estimated empirical accelerations are not affected by the model replacement, which means that the updated model does not reduce any systematics. It simply causes a shift in the acceleration scaling.

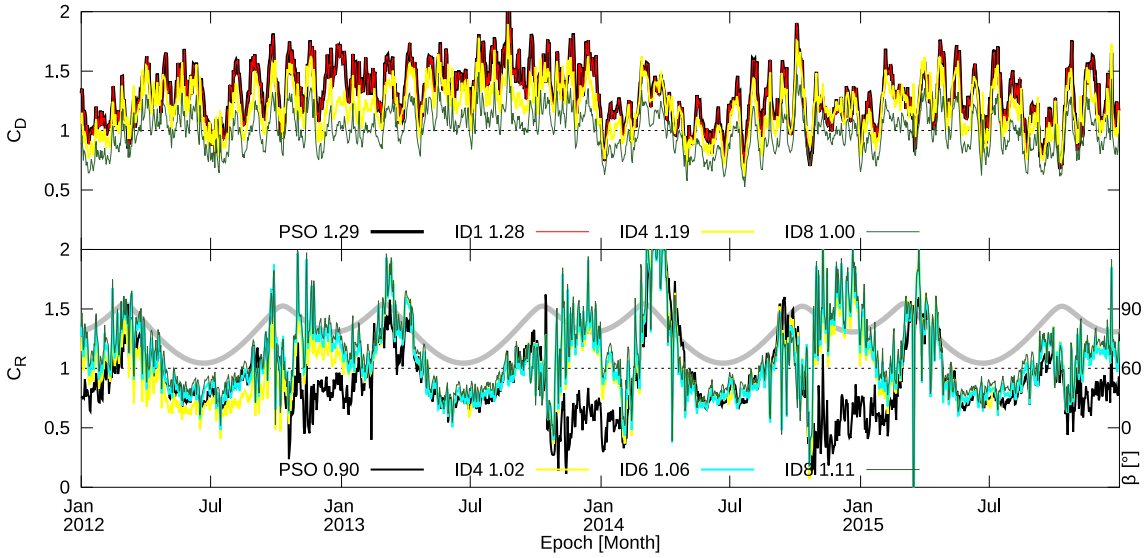

Fig. 4.13: Selected series of the aerodynamic acceleration scaling factor C_D (top), and the solar radiation pressure scaling factor C_R (bottom) of TerraSAR-X. The beta angle (Sun elevation above the orbital plane) is illustrated in gray. For each solution, the mean value of the estimated C_D/C_R coefficient is given next to the corresponding label.

As described in Equation 3.43, the aerodynamic acceleration model proposed by Sentman [1961] considers the influence of drag and lift. This effect is considered by ID5. The scaling factor C_D improves from 1.19 in case of ID4 to 1.00. Like for the previous plate model introduction, the empirical accelerations are not affected significantly. Compared to the simple cross-sectional approach, the Sentman formulation causes a 30 % reduction of the C_D coefficient. The orbit solutions themselves are not significantly impacted by this update, since the estimated C_D parameter compensates most of the effect.

C_R is the solar radiation pressure scaling parameter. An update of the cannon-ball sphere with a complex macro model in ID 6 leads to a C_R change from 0.92 to 1.06 (cf. Table 4.6). It is obvious that the corresponding time series in Fig. 4.13 shows a correlation of the C_R stemming from the PSOs with the β angle, i.e. the Sun elevation above the orbital plane. When introducing the macro model formulation, the β-angle dependency slightly reduces but is still present for low β-angles. The time series of the C_R coefficient in Figure 4.13 does not show any significant linear trend over the 4-years period, which could hint to aging effects and changed optical properties.

Table 4.6: TerraSAR-X orbit solutions: orbit solutions performance metrices in the lower table; 2012–2015. $\bar{x} \pm \sigma_x$

ID	SLR res.	SLR pos. est. [mm]			Day-bnd	Ephemeris comparison [mm]		
	[mm]	R	T	N	[mm]	R	T	N
PSO	-1.8 ± 17.5	-1.8 ± 2.6	3.2 ± 4.2	-12.2 ± 9.7	4.5	0 ± 0	0 ± 0	0 ± 0
1	-1.3 ± 19.0	-1.0 ± 2.4	-0.1 ± 4.5	-13.5 ± 14.9	4.6	0 ± 12	-1 ± 17	-1 ± 12
2	-1.4 ± 17.8	-1.1 ± 2.5	-0.4 ± 4.4	-12.6 ± 11.0	4.6	0 ± 12	-1 ± 17	0 ± 11
3	-1.6 ± 16.7	-1.4 ± 2.6	-0.9 ± 4.4	-11.8 ± 5.9	5.4	0 ± 12	-1 ± 17	1 ± 14
4	-1.6 ± 16.7	-1.4 ± 2.6	-1.0 ± 4.4	-11.1 ± 6.3	5.1	0 ± 12	-1 ± 17	2 ± 13
5	-1.6 ± 16.7	-1.3 ± 2.6	-1.0 ± 4.4	-11.8 ± 5.7	5.3	0 ± 12	-1 ± 17	1 ± 15
6	-1.6 ± 16.6	-1.4 ± 2.6	-0.9 ± 4.3	-10.8 ± 6.0	5.3	0 ± 12	-1 ± 17	2 ± 14
7	0.2 ± 16.0	1.4 ± 2.7	-0.8 ± 4.3	-8.0 ± 6.2	5.3	3 ± 12	0 ± 17	5 ± 14
8	0.2 ± 16.1	1.5 ± 2.7	-0.8 ± 4.3	-8.5 ± 6.1	5.1	3 ± 12	0 ± 17	5 ± 14

4.3 Orbit Analysis

Similar to the RDOD performance indicators assessed in the previous section, the quality of the resulting orbit solutions is analyzed for TerraSAR-X within the 2012–2015 period. Daily orbit solutions are estimated for each ID, listed in Table 4.1. Applied validation techniques are explained in Section 2.3, which also includes the selected setup of satellite laser ranging. In addition, SLR measurements are employed to identify systematic orbit errors in the RTN components. Ephemeris comparisons to the PSO solutions further help to identify offsets. As measure of the internal orbit consistency, day-boundary discontinuities are computed for each solution.

The updated gravity field and ocean tide models in ID 1 show slightly reduced SLR-based offset estimates of −1 mm in radial and −3 mm in along-track. The cross-track component shows a +1 mm increase compared to the PSOs.

Switching from Jacchia-71G (ID 1) to DTM 2012 (ID 2) does not significantly influence the resulting orbit solutions, as shown by SLR. Contrary, the switch from DTM 2012 to NRLMSISE-00 (ID 3) significantly reduces the SLR-based cross-track standard deviation from −11 mm to −5.9 mm. This change is also clearly outlined by the corresponding time series, available in Figure 4.14. In radial and tangential direction, the changes are not significant, which might be attributed to the small density differences along the day-night boundary (cf. Fig. 4.6). According to Bruinsma et al. [2012], NRLMSISE-00 is expected to perform slightly better than DTM 2012 for altitudes above 500 km, which

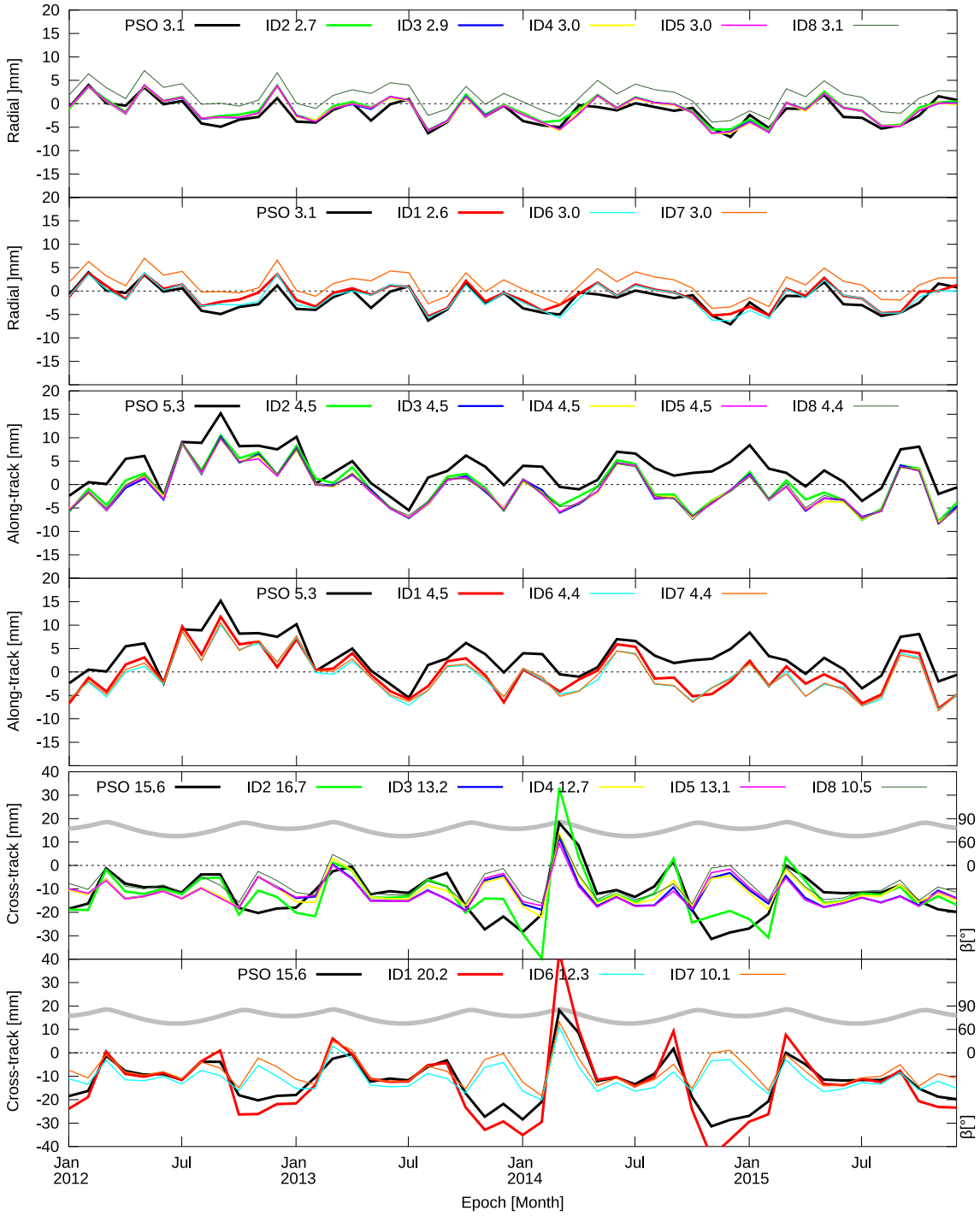

Fig. 4.14: SLR-derived monthly position offset estimates of TerraSAR-X; the Sun elevation β above the orbital plane is illustrated in gray. The numerical value in the legend is the corresponding RMS in mm.

is underlined by the SLR-based position offsets. The SLR residuals, however, are not affected significantly. The orbit discontinuities show a slight 1 mm degradation when introducing NRLMSISE-00. In case of low Earth orbiters like TerraSAR-X, the proper choice of the atmospheric density model is important, since the atmospheric density models show different results in the corresponding altitude. Replacement of the Jacchia-71G atmospheric density model by NRLMSISE-00 shows reduced empirical accelerations as well as the improved SLR residuals.

For assessment of the aerodynamic acceleration models, a direct ephemeris comparison of the cbl (ID 3; serves as reference), mac (ID 4) and snt (ID 5) orbit solutions from the 2012–2015 period is available in Table 4.7. Compared to the cannon-ball

Table 4.7: Ephemeris comparison of TSX-1 orbit solutions with ID 4 and ID 5 aerodynamic acceleration models (ID 3 serves as reference). Period 2012–2015; $\bar{x} \pm \sigma_x$.

ID	R [mm]	T [mm]	N [mm]
4 (mac)	0 ± 7	-1 ± 8	-1 ± 5
5 (snt)	0 ± 7	0 ± 8	0 ± 5

model, the macro solution is shifted by -1 mm in along- and cross-track. This shift vanishes when Sentman is selected as aerodynamic acceleration model. However, both the macro and Sentman solutions show a standard deviation of up to 8 mm in the along-track component. The SLR-based position offset estimates exhibit a slightly decreased mean (-0.7 mm) and increased cross-track standard deviation ($+0.4$ mm) when switching from ID 3 to ID 4. The solution based on Sentman does not show any significant change compared to the cannon-ball model. The aerodynamic acceleration models do not significantly change the resulting orbit solutions, since the empirical accelerations largely compensate deficits of the employed models.

These findings coincide with using the macro model for solar radiation pressure in ID6. A one-mm cross-track shift is induced by the SLR-based position estimates. The SLR residuals are kept at -1.6 ± 16.7 mm.

The radiation reflected and emitted from the Earth's surface (ERP) significantly influences the orbit solutions of TSX-1 (ID7). Introducing ERP, which mainly acts in radial direction, decreases the mean SLR residuals by 1.8 mm from -1.6 mm to 0.2 mm over the analyzed period. According to [Montenbruck et al., 2017]

$$\Delta a_{\mathrm{R}} = -3 \frac{GM_{\oplus}}{r^2} \cdot \frac{\Delta r_{\mathrm{R}}}{r} \quad , \tag{4.3}$$

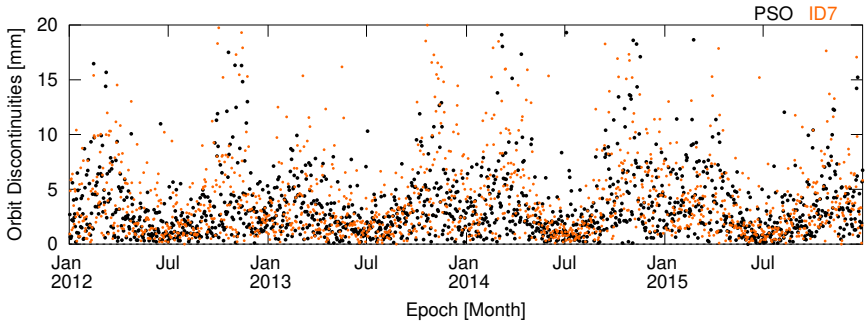

Fig. 4.15: Orbit discontinuities at day boundaries, for TerraSAR-X PSO, and ID7 solutions.

the radial shift of 1.8 mm translates to 7 nm/s^2, which largely corresponds to the ERP acceleration. According to Figure 4.4, the magnitude of ERP acceleration is 11 nm/s^2 in radial direction. In addition, the cross-track component of the SLR-based monthly position offset estimates shows a 2 mm reduction.

Considering the impact of wind (ID 8) does not significantly change the orbits. The reason is simply that the magnitude of the resulting accelerations is too small to have any impact on the orbit solutions.

The 3-D-RMS at day boundaries is illustrated by Figure 4.15. For all stated comparisons, the overall mean discontinuities are in the range between 4 and 6 mm. However, peak amplitudes are at 20 mm for both solutions. Obviously, the orbits solutions exhibit a better internal consistency during the months of July, which is in accordance with the SLR-based cross-track estimates, and the SLR residuals, which show reduced standard deviation during these months. The dependency of the angle β (cf. Figure 4.14) hints to the strong dependency of the dusk-dawn orbit of TerraSAR-X and the elevation of the Sun.

The updated gravity field, the NRLMSISE-00 density model, and consideration of ERP significantly improve the orbit solutions of TerraSAR-X. Selecting the macro model for SRP or within the aerodynamic acceleration model does not lead to any substantial improvements, since the empirical accelerations compensate any deficit in the employed models, which may be related to the dusk-dawn orbit geometry.

5

Ambiguity Fixing

5.1 Methodology

Several studies demonstrate the potential of fixing double-difference carrier phase ambiguities for determining accurate orbit solutions of low Earth orbiters [Jäggi et al., 2007; Laurichesse et al., 2014; Bertiger et al., 2010]. Within this section, the selected method for ambiguity fixing is briefly introduced, and the resulting orbit solutions are thoroughly assessed in Section 5.2.

The carrier phase (CP) range obtained from the geodetic receivers on Sentinel-1A, Swarm-C, TanDEM-X or TerraSAR-X is an ambiguous measurement with a constant offset from the pseudorange (PR). In this case, between-receiver and between-satellite double differences of the carrier phase range exhibit a double-difference (DD) ambiguity which is an integer multiple of the wavelength.

Pseudorange and carrier phase observations between a receiver in low Earth orbit (subscript $_{\mathrm{r}}$) and a spacecraft (superscript $^{\mathrm{s}}$) on GPS L_1 (index $_1$) and GPS L_2 (index $_2$) are described by the generic observation model for the pseudorange (p)

$$\begin{aligned} p^s_{\mathrm{r},1} &= (\varrho + \xi^s_{\mathrm{r},1}) + c(dt_r - dt^s) + I^s_{\mathrm{r},1} + c(d_{\mathrm{r},1} - d^s_1) \\ p^s_{\mathrm{r},2} &= (\varrho + \xi^s_{\mathrm{r},2}) + c(dt_r - dt^s) + I^s_{\mathrm{r},2} + c(d_{\mathrm{r},2} - d^s_2) \end{aligned} \tag{5.1}$$

and the carrier phase range (φ)

$$\begin{aligned} \varphi^s_{\mathrm{r},1} &= (\varrho + \zeta^s_{\mathrm{r},1}) + c(dt_r - dt^s) - I^s_{\mathrm{r},1} + c(\delta_{\mathrm{r},1} - \delta^s_1) + \lambda_1 N^s_{\mathrm{r},1} + \lambda_1 \omega^s_r \\ \varphi^s_{\mathrm{r},2} &= (\varrho + \zeta^s_{\mathrm{r},2}) + c(dt_r - dt^s) - I^s_{\mathrm{r},2} + c(\delta_{\mathrm{r},2} - \delta^s_2) + \lambda_2 N^s_{\mathrm{r},2} + \lambda_2 \omega^s_r \quad . \end{aligned} \tag{5.2}$$

Within this equations, ϱ corresponds to the geometric range between the GPS satellite's antenna reference point at the time of signal transmission, and the receiver (time of signal reception), whereas λ_1 and λ_2 denote the wavelength of the L_1 and L_2 frequency. Pseudorange corrections of the PCOs are denoted by ξ, and carrier phase PCO and PCV corrections are denoted by ζ. Note that equations 5.1 and 5.2 are exclusively for satellites in low Earth orbit, since any tropospheric corrections are neglected. Time offsets of the receiver and satellite clock from the reference time scale are denoted by the receiver and satellite clock offsets (dt_r, dt^s,). Code delay and phase advance due to ionospheric propagation effects are expressed by I. Any signal-specific range biases, induced by the receiver and transmitter signal processing, are expressed for pseudorange by $cd_{\mathrm{r,i}}$ and cd^s_i, and for carrier phase by $c\delta_{\mathrm{r,i}}$ and $c\delta^s_i$. Specific for the carrier phase range, the ambiguities $N^{\mathrm{s}}_{\mathrm{r,i}}$ are introduced, which correspond to the arbitrary initial value of the carrier phase measurement process. Phase wind-up effects related to a time-varying orientation of the receiver and transmitter antennas are modeled according to Wu et al. [1993], and indicated by ω.

5.1.1 Linear Combinations

Ionosphere-free Linear Combination The ionosphere-free (IF) linear combination eliminates first order ionospheric effects. The corresponding IF observations for pseudorange and carrier phase are formed via

$$\begin{aligned} p^s_{\mathrm{r,IF}} &= (\varrho + \xi^s_{\mathrm{r,IF}}) + c(dt_r - dt^s) + c(d_{\mathrm{r,IF}} - d^s_{\mathrm{IF}}) \\ \varphi^s_{\mathrm{r,IF}} &= (\varrho + \zeta^s_{\mathrm{r,IF}}) + c(dt_r - dt^s) + c(\delta_{\mathrm{r,IF}} - \delta^s_{\mathrm{IF}}) \\ &\quad + \mathrm{IF}(\lambda_1 N^s_{\mathrm{r},1}, \lambda_2 N^s_{\mathrm{r},2}) + \mathrm{IF}(\lambda_1, \lambda_2)\omega^s_r \quad . \end{aligned} \tag{5.3}$$

The IF-term corresponds to

$$IF(x_1, x_2) := (\Lambda + 1)x_1 - \Lambda x_2 \quad \text{with} \tag{5.4}$$

$$\Lambda = \frac{f_2^2}{f_1^2 - f_2^2} \quad . \tag{5.5}$$

Within the RDOD process, the IF combinations of code-and carrier phase observations are processed to adjust orbit and clock parameters as well as the IF combination of L_1 and L_2 ambiguities based on the measurement model (Equation 5.3).

Melbourne-Wübbena Linear Combination Melbourne [1985] and Wübbena [1985] proposed a geometry- and ionosphere-free linear combination, which is widely employed for cycle-slip detection and ambiguity resolution [Hofmann-Wellenhof et al., 2008]. The Melbourne-Wübbena (MW) combination is formed from dual-frequency code and phase observations:

$$\begin{aligned} \mathrm{MW}(\varphi_1, \varphi_2, p_1, p_2) &= \left(\frac{f_1\varphi_1 - f_2\varphi_2}{f_1 - f_2}\right) - \left(\frac{f_1 p_1 - f_2 p_2}{f_1 - f_2}\right) \\ &= \left(\frac{c}{f_1 - f_2}\right) \cdot \left[\left(\frac{\varphi_1}{\lambda_1} - \frac{\varphi_2}{\lambda_2}\right) - \frac{f_1 - f_2}{f_1 + f_2}\left(\frac{p_1}{\lambda_1} + \frac{p_2}{\lambda_2}\right)\right] \quad . \end{aligned} \tag{5.6}$$

Obviously, the derived combination is free from the geometric range ϱ, the clock offsets dt_r, dt^s, the both ionospheric delays $I^s_{\mathrm{r,i}}$, and the phase wind up (PWU) term $\omega^s_{\mathrm{r,i}}$. However, the combination is still affected by transmit antenna code and phase variations and biases.

5.1.2 Wide- and Narrow-lanes

Introducing the wide-lane (WL) and narrow-lane (NL) wavelenghts

$$\lambda_{\mathrm{WL}} = \frac{c}{f_1 - f_2} \quad \text{and} \quad \lambda_{\mathrm{NL}} = \frac{c}{f_1 + f_2} \quad , \tag{5.7}$$

and the WL ambiguity, the carrier phase Equation 5.3 can be re-written as

$$\begin{aligned} \varphi^s_{\mathrm{r,IF}} = &(\rho + \zeta^s_{\mathrm{r,IF}}) + c(dt_r - dt^s) + c(\delta_{\mathrm{r,IF}} - \delta^s_{\mathrm{IF}}) \\ &+ \lambda_{\mathrm{NL}}(N^s_{\mathrm{r},1} + \frac{\lambda_{\mathrm{WL}}}{\lambda_2} N^s_{\mathrm{r,WL}}) + \lambda_{\mathrm{NL}}\omega^s_r \quad . \end{aligned} \tag{5.8}$$

The term

$$N^s_{\mathrm{r,WL}} = N^s_{\mathrm{r},1} - N^s_{\mathrm{r},2} \tag{5.9}$$

denotes the WL ambiguity. Equation 5.8 describes the dependence of the ionosphere-free linear combination, used throughout the RDOD, and the phase ambiguities.

Inserting Equations 5.1 and 5.2 into 5.6, one obtains the MW observation model:

$$\begin{aligned} \mathrm{MW}(\varphi^s_{\mathrm{r},1}, \varphi^s_{\mathrm{r},2}, p^s_{\mathrm{r},1}, p^s_{\mathrm{r},2}) = &\lambda_{\mathrm{WL}} N^s_{\mathrm{r,WL}} + \mathrm{MW}(\xi^s_{\mathrm{r},1}, \xi^s_{\mathrm{r},2}, \zeta^s_{\mathrm{r},1}, \zeta^s_{\mathrm{r},2}) \\ &+ c\mathrm{MW}(\delta^s_{\mathrm{r},1}, \delta^s_{\mathrm{r},2}, d^s_{\mathrm{r},1}, d^s_{\mathrm{r},2}) \\ &- c\mathrm{MW}(\delta^s_1, \delta^s_2, d^s_1, d^s_2) \quad . \end{aligned} \tag{5.10}$$

According to Laurichesse et al. [2014], this equation can be re-written as

$$MW(\varphi^s_{\mathrm{r},1}, \varphi^s_{\mathrm{r},2}, p^s_{\mathrm{r},1}, p^s_{\mathrm{r},2}) \approx \lambda_{\mathrm{WL}} N^s_{\mathrm{r,WL}} + \lambda_{\mathrm{WL}}(\mu_{\mathrm{r,WL}} - \mu^s_{\mathrm{WL}}) \tag{5.11}$$

with the WL biases

$$\begin{aligned} \mu_{\mathrm{r,WL}} &= c\mathrm{MW}(\delta_{\mathrm{r},1}, \delta_{\mathrm{r,s}}, d_{\mathrm{r},1}, d_{\mathrm{r},2}) / \lambda_{\mathrm{WL}} \\ \mu^s_{\mathrm{WL}} &= c\mathrm{MW}(\delta^s_1, \delta^s_2, d^s_1, d^s_2) / \lambda_{\mathrm{WL}} \quad . \end{aligned} \tag{5.12}$$

Equation 5.11 neglects the effect of phase variations to the small magnitude compared to the measurement errors, or the WL wavelength of 86 cm for GPS L_1/L_2 observables [Laurichesse et al., 2014]. The fractional wide-lane satellite biases (WSBs) $\hat{\mu}^s_{\mathrm{wl}}$ are provided by Centre National d'Etudes Spatiales (CNES) on a daily basis derived from a global station network [Loyer et al., 2012]. In addition, CNES also provides high-rate

values of the satellite phase offset, denoted as $c\hat{dt}^s$. Figure 5.1 illustrates the WSBs of two selected GPS satellites. Jumps in the WSB series of G03 in December 2014, and for G04 on November 2, 2015, are caused by reassignment of the pseudo-random noise (PRN) codes to a different spacecraft [Joint Space Operations Center, 2014, 2015b].

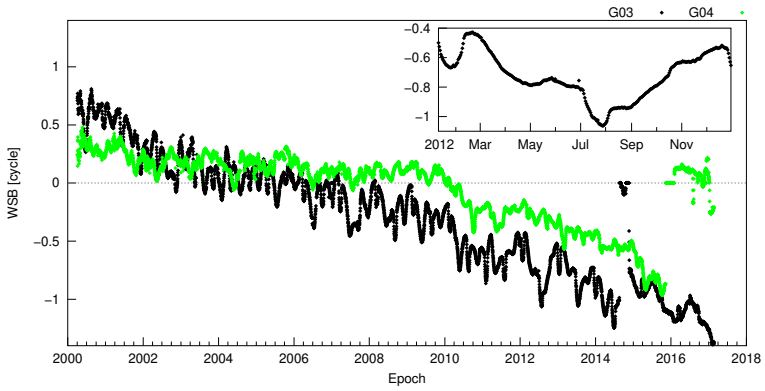

Fig. 5.1: CNES widelane satellite biases (WSBs) of two GPS satellites.

Finally, the ionosphere-free observation model can be formed by

$$\begin{aligned} p^s_{\mathrm{r,IF}} &= (\rho + \xi^s_{\mathrm{r,IF}}) + c(\hat{dt}_r - \hat{dt}^s) + c(d_{\mathrm{r,IF}} - d^s_{\mathrm{IF}}) + e^s_{\mathrm{r,IF}} \\ \varphi^s_{\mathrm{r,IF}} &= (\rho + \zeta^s_{\mathrm{r,IF}} + \lambda_{\mathrm{NL}}\omega^s_r) + c(\hat{dt}_r - \hat{dt}^s) + \lambda_{\mathrm{NL}}(\hat{N}^s_{\mathrm{r,1}} + \frac{\lambda_{\mathrm{WL}}}{\lambda_2}\hat{N}^s_{\mathrm{r,WL}}) \quad . \end{aligned} \tag{5.13}$$

The term $e^s_{\mathrm{r,IF}}$ aggregates combinations of the fractional phase biases and corresponds to the difference of code and phase clocks. Since this correction is not provided by the utilized CNES products it is neglected, which may result in slightly increased pseudorange residuals. The term

$$\hat{N}^s_{\mathrm{r,WL}} = \mathrm{MW}/\lambda_{\mathrm{WL}} - \mu_{\mathrm{r,WL}} + \hat{\mu}^s_{\mathrm{WL}} \tag{5.14}$$

can be determined from the MW combination of the code and phase observations and given fractional satellite wide-lane ambiguities $\hat{\mu}^s_{\mathrm{WL}}$. Following Equation 5.13, the next steps are pass-wise fixing of the wide-lane $\hat{N}^s_{\mathrm{r,WL}}$ and $\hat{N}^s_{\mathrm{r,1}}$ ambiguities.

5.1.3 Pass-Wise Ambiguity Fixing

Practically, the process of ambiguity estimation requires several steps based upon a pass-wise fixing strategy. Being P the number of passes, first the pass-wise averaged Melbourne-Wübbena combinations are computed

$$m_P = ((\bar{\mathrm{MW}}_r^s)_P / \lambda_{\mathrm{WL}} + \hat{\mu}_{\mathrm{WL}}^s) \tag{5.15}$$

where the vector

$$(m_P) = (\hat{N}_{\mathrm{r,WL}}^s)_P + \hat{\mu}_{\mathrm{r,WL}} + \epsilon_{\mathrm{m,I}} \tag{5.16}$$

is split up into pass-wise integer values, denoted by $(\hat{N}_{\mathrm{r,WL}}^s)_P$, and fractional wide-lane biases of the receiver $\hat{\mu}_{\mathrm{r,WL}}$. The term ϵ additionally considers residual errors, caused e.g. by receiver noise or multipath. Next, the pass-wise values of $(\hat{N}_{\mathrm{r,WL}}^s)_P$ and $\hat{\mu}_{\mathrm{r,WL}}$ are estimated using a rounding approach, relative to a selected reference pass [Montenbruck et al., 2017].

The estimated values form the basis of pass-wise $\hat{N}_{\mathrm{r,1}}^s$ ambiguity estimation. For this purpose, float-valued carrier-phase range biases B_P have to be estimated, which are based on the observation model

$$\begin{aligned} p_{\mathrm{r,IF}}^s &= (\rho + \xi_{\mathrm{r,IF}}^s) + c(\tilde{dt}_r - \hat{dt}^s) + c(d_{\mathrm{r,IF}} - d_{\mathrm{IF}}^s) \\ \varphi_{\mathrm{r,IF}}^s &= (\rho + \zeta_{\mathrm{r,IF}}^s + \lambda_{\mathrm{WL}}\omega_r^s) + c(\tilde{dt}_r - \hat{dt}^s) - B_P \quad . \end{aligned} \tag{5.17}$$

They correspond to the average difference between the ionosphere-free pseudorange and carrier phase observations, whereas $\tilde{dt}_r$ denotes the receiver clock, estimated in the float-ambiguity orbit determination.

Based on comparison with Equation 5.13, the bias B_P of pass P and the ambiguities are related via

$$-B_P = \lambda_{\mathrm{NL}}(\hat{N}_{\mathrm{r,1}}^s + \frac{\lambda_{\mathrm{WL}}}{\lambda_2}\hat{N}_{\mathrm{r,WL}}^s) + c(\hat{dt}_r - \tilde{dt}_r) \quad . \tag{5.18}$$

Estimating the pass-specific N_1 ambiguities in

$$b_P = (\hat{N}_{\mathrm{r,1}}^s)_P + \tau \quad , \tag{5.19}$$

with the scaled clock difference

$$\tau = c(\hat{dt}_r - \tilde{dt}_r)/\lambda_{\mathrm{WL}} \tag{5.20}$$

requires knowledge of the previously determined values of the float ambiguity B_P and the integer-constrained wide-lane ambiguity N_{WL}

$$b_P = -B_P/\lambda_{\mathrm{NL}} - \frac{\lambda_{\mathrm{WL}}}{\lambda_2}(\hat{N}^s_{\mathrm{r,WL}})_P \quad . \tag{5.21}$$

There is only a slight variation of τ between adjacent passes B and J, and equation

$$\Delta b_{PJ} = \Delta(\hat{N}^s_{\mathrm{r,1}})_{PJ} + \Delta\epsilon_{b,PJ} \tag{5.22}$$

is solved via simple integer rounding [Montenbruck et al., 2017; Freeden et al., 2010]. The residual errors in the differenced biases $\Delta\epsilon_{b,PJ}$ require a conservative threshold of ≤ 0.15 cy as used throughout the present study for accepting relative ambiguities between two passes. Estimating the $\hat{N}^s_{\mathrm{r,1}}$ ambiguities can now be performed. Details of the ambiguity fixing strategy are published in Montenbruck et al. [2017].

To summarize the integer ambiguity estimation, the following pre-conditions and steps are required: (1) availability of L_1 and L_2 GPS code and phase observations, as well as wide-lane satellite biases and clock offset solutions including the fractional phase biases. (2) Next, pass-wise Melbourne-Wübbena linear combinations are formed, and wide-lane ambiguities fixed. (3) N_1 ambiguity fixing is performed, based upon estimated float ambiguities of the ionosphere-free carrier phase combination and the previously determined wide-lane ambiguities.

5.2 Results

Results of GPS integer ambiguity-fixed reduced-dynamic orbit solutions of S-1A (2016), SWC (2014–2016), and TSX-1/TDX-1 (2012–2015) are discussed. Required wide-lane satellite biases and consistent satellite clock and orbit products are provided by CNES as high-rate (30 s) products. The applied reduced-dynamic orbit parameterization is identical to ID7, which considers enhanced dynamical models.

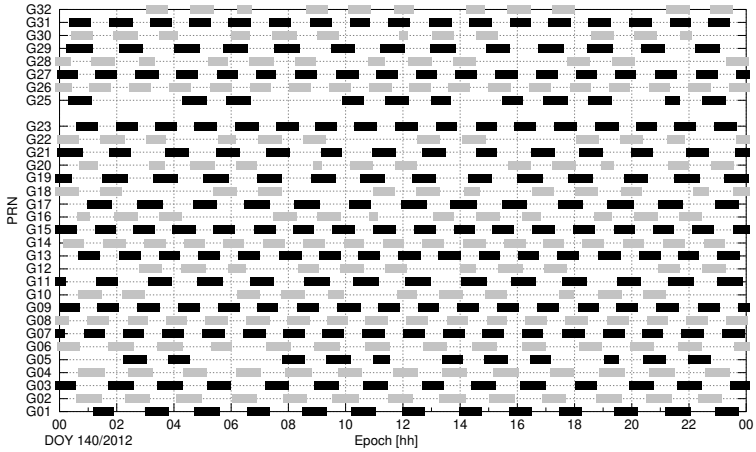

Fig. 5.2: GPS satellite passes tracked by the IGOR on TerraSAR-X (DOY 140/2012). For clarity, black and gray colors are used for odd and even PRN numbers, respectively.

5.2.1 Performance Assessment

Figure 5.2 shows a GPS tracking statistic of the IGOR on TerraSAR-X. In total, all 31 operational GPS satellites are tracked during 24 hours with an average tracking pass length of 17 minutes. G24 is not transmitting signals, therefore no tracking data is available for that particular satellite [Joint Space Operations Center, 2015a].

The distribution of WL and N_1 residuals, i.e. of the differences between float and fixed wide-lane and N_1 ambiguities, is shown in Figure 5.3. For TSX-1, 99% of the wide-lane residuals are confined to less than $3\sigma = 0.19$ cy by magnitude, which enables a robust WL ambiguity fixing through integer rounding. Only two out of 659 passes exhibit wide-lane ambiguities outside ± 0.4 cy. For Sentinel-1A, all of the available 403 passes exhibit wide-lane residuals of less than $3\sigma = 0.21$ cy by magnitude, which attests also the high applicability of integer rounding for wide-lane ambiguities. In total 500 passes are available at DOY 344/16 for Swarm-C, where all passes are below 3σ of 0.28 cy.

Corresponding N_1 fixing statistics are available in Figure 5.3, too. Out of 569 passes, approximately 86% of the $\Delta N^s_{r,1}$ ambiguities passed the threshold of 0.15 cy for the relative ambiguity between two passes in case of TerraSAR-X. For S-1A, 84 % out of 403 passes passed the threshold, for SWC, N_1 ambiguities were successfully fixed in 499 passes (out of 500).

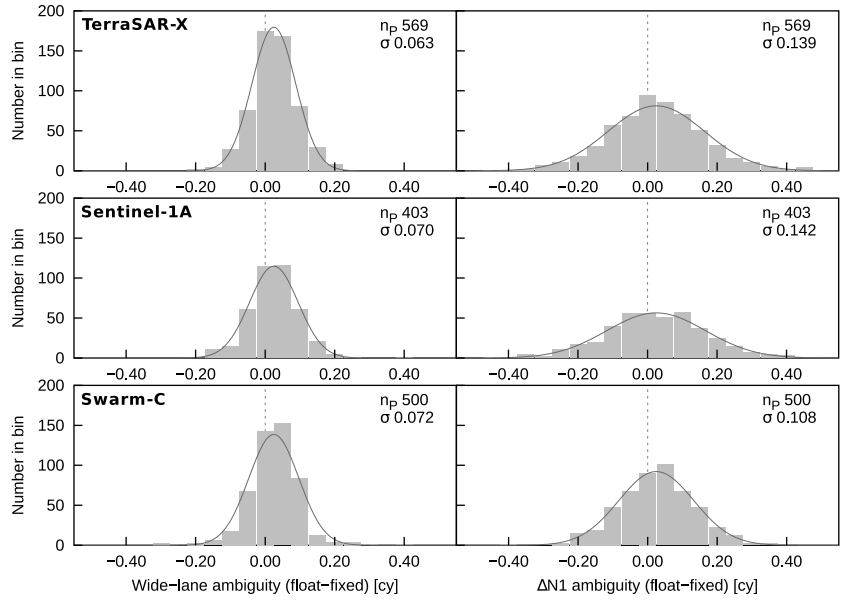

Fig. 5.3: Distribution of relative wide-lane (WL) and N_1 ambiguity residuals of TerraSAR-X (102/2015), Sentinel-1A (115/2016), and Swarm-C (344/2016). Gaussian distribution with the corresponding standard deviation is shown by the gray curve.

Time series of daily WL and N_1 ambiguity fixing rates are shown in Figure 5.4. The WL fixing rate is constantly at a high level of better than 98% for all three missions (cf. Table 5.1). The N_1 ambiguities are successfully resolved to 98 % for TSX-1 and TSX-1, whereas the rate of SWC is slightly degraded with 96 %. S-1A holds a fixing success rate of 99 %. Performance differences in the resolving statistics are related to the tracking performance of the employed GPS receivers.

Resulting mean values of daily CP and PR residuals, as well as mean and standard deviation of empirical accelerations based on daily RMS values are available in Table 5.1. Compared to the float solutions ID7, the ambiguity-fixed solutions systematically exhibit slightly larger residuals. Except for TDX-1, the PR residuals are increased by about 1 cm (2 %, float compared to integer), whereas the CP residuals exhibit a 1 mm increase, corresponding to 20 %. These changes are induced by the fact that the ambiguity fixed solutions have less degree of freedom compared to the float solutions. In the float solutions, remaining modeling deficits can be compensated by the ambiguities. In addition, the applied PCV residual maps are identical, which applies 'wrong' corrections to the measurements (cf. Section 5.2.2).

Table 5.1: RDOD quality indicators and ambiguity fixing statistic. S-1A: 2016; SWC: 2014–2016; TSX/TDX-1: 2012 – 2015 (ID7), 2012–2017 (ID9). $\bar{x} \pm \sigma_{\bar{x}}$.

SC	ID	Pass fix. [%]		CP res.	PR res.	Emp. acc. [nm/s^2]		
		WL	N1	[mm]	[m]	R	T	N
TSX-1	PSO			4.42 ± 0.64	0.59 ± 0.01	0.6 ± 0.2	11.6 ± 4.6	13.1 ± 2.5
TSX-1	7			4.11 ± 0.82	0.58 ± 0.01	0.3 ± 0.1	7.3 ± 3.6	7.3 ± 3.6
TSX-1	9	99.5	98.1	6.09 ± 0.84	0.59 ± 0.02	0.2 ± 0.1	5.9 ± 3.4	7.5 ± 1.1
TDX-1	PSO			5.26 ± 0.77	0.64 ± 0.04	0.9 ± 0.4	12.0 ± 4.6	12.0 ± 4.6
TDX-1	7			4.77 ± 1.04	0.63 ± 0.05	0.3 ± 0.1	7.3 ± 3.6	7.3 ± 3.6
TDX-1	9	99.5	98.1	6.35 ± 0.91	0.62 ± 0.04	0.3 ± 0.1	5.8 ± 3.2	7.4 ± 1.8
S-1A	7			6.02 ± 8.22	0.54 ± 0.11	0.9 ± 0.2	9.7 ± 3.3	15.7 ± 3.8
S-1A	9	99.9	99.3	6.51 ± 0.41	0.55 ± 0.01	0.9 ± 0.2	10.3 ± 3.3	16.1 ± 3.8
SWC	9	99.1	96.8	6.08 ± 0.96	0.79 ± 0.22	4.7 ± 1.0	15.9 ± 7.6	18.4 ± 2.6

The empirical accelerations are not significantly impacted in radial direction, which corresponds to the strong contribution of the dynamic leveling. In addition, also the cross-track component does not show any significant reduction, meaning that the dynamical models already properly cover the effects in that direction. Only the along-track component shows a reduction of up to 2 nm/s^2 reduction, when applying ambiguity-fixed solutions.

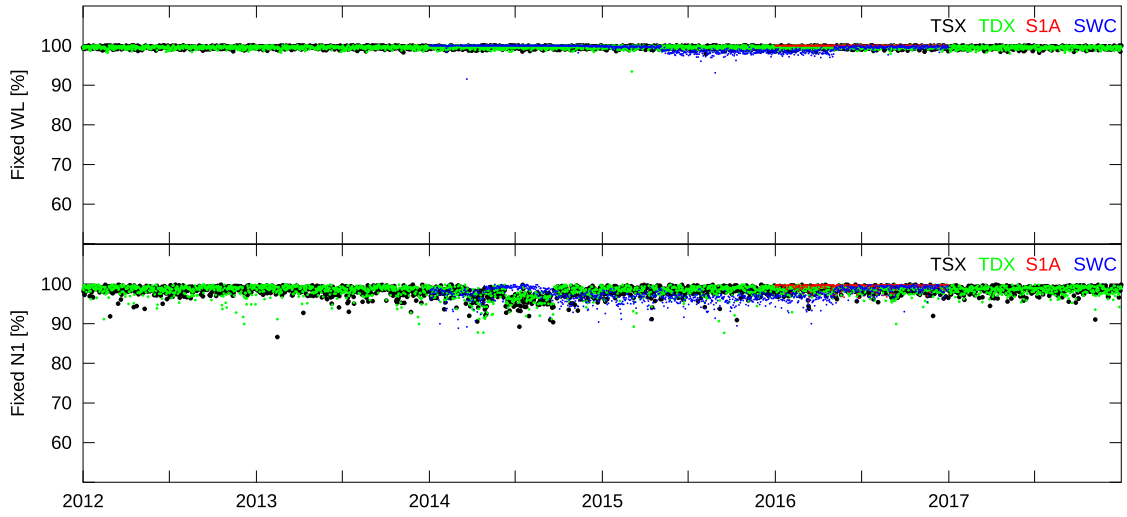

Fig. 5.4: Rate of fixed wide-lane (WL) and final (N1) ambiguities.

For TDX-1, the changes in the empirical accelerations are in the same order of magnitude. For S-1A, there is a minor increase of +1 nm/s^2 in the along- and cross-track component.

5.2.2 GPS Phase Center Variations

As shown in the previous section, GPS integer ambiguities change the empirical accelerations in along-track direction and lead to increased CP residuals, when applying default (float) PCVs. To assess the impact on the orbit solutions, the antenna phase patterns of TerraSAR-X are re-calibrated, using ID9 carrier phase residuals (2015 complete) as input for estimating the phase center variations. Estimating phase patterns is a step-wise approach where phase patterns are estimated from RDOD carrier phase residuals in an iterative loop (cf. Section 2.2.3). The standard phase patterns, which basically have

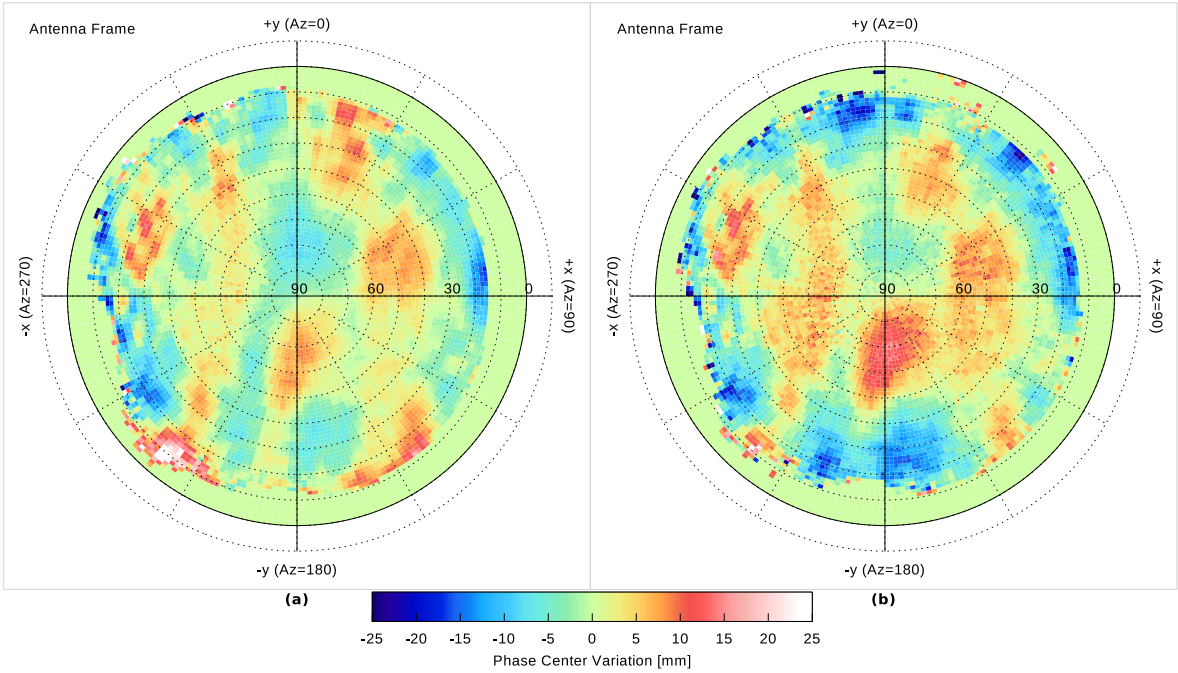

Fig. 5.5: Comparison of a priori PSO (a) and estimated (b) phase patterns of the GPS antenna on TerraSAR-X.

been employed for all PSOs of the TerraSAR-X spacecraft and are based on CP residuals from 30 days in January 2011, serve as basis for the calibration, and the fixed ID9 solutions. Based upon that solution, 12 daily CP residual files (with 30 days spacing,

Table 5.2: TerraSAR-X orbit solutions with different iterations of satellite's GPS antenna phase pattern estimation. Carrier phase and code residuals, empirical accelerations, SLR-derived monthly position estimates, and SLR residuals. All values as $\bar{x} \pm \sigma_x$. Time span: 2015.

ID	CP res.	PR res.	Emp. acc. [nm/s^2]			SLR res.	SLR-based position offsets [mm]			
	[mm]	[m]	R	T	N	[mm]	R	T	N	RMS
ID9	6.01 ± 1.09	0.58 ± 0.00	0.27	8.02	7.81	0.9 ± 11.8	1.8 ± 2.3	-0.2 ± 2.7	-0.5 ± 1.7	4.4
it1	5.68 ± 0.89	0.58 ± 0.01	0.28	8.05	7.91	0.8 ± 12.0	1.6 ± 2.1	0.4 ± 2.6	-0.7 ± 1.7	4.2
it2	5.39 ± 0.60	0.58 ± 0.01	0.26	8.01	7.80	0.8 ± 11.8	1.7 ± 2.2	0.1 ± 2.7	-0.8 ± 1.6	4.3
it3	5.36 ± 0.56	0.58 ± 0.01	0.26	8.01	7.79	0.8 ± 11.8	1.6 ± 2.2	0.3 ± 2.7	-1.1 ± 1.6	4.3

observation step size 30 s) are introduced for phase pattern estimation. The derived pattern is then again used for estimating daily orbit solutions and carrier phase residuals in 2015. After in total 4 iterations, the carrier phase maps do not change significantly, and the iteration stops.

The introduced a priori (float), and the resulting (fixed) phase patterns are shown in Figure 5.5. The pattern on the left is the operational pattern, which has been estimated with the operational PSO models and without ambiguity fixing. The right pattern results from RDOD ID9 with updated models/applied integer ambiguity fixing. Both maps show similar characteristics with more pronounced amplitudes in case of the re-calibrated pattern. The pattern exhibits corrections up to 20 mm in nadir direction, and up to −20 mm for low elevations. Table 5.2 shows CP/PR residuals, empirical accelerations, and the orbit quality. The latter is assessed by SLR (the setup is kept constant during this thesis). The carrier phase residuals are reduced by 12 % by estimating the phase patterns. The empirical accelerations do not show a significant change. The SLR residuals are kept at the level of 1 ± 12 mm. Of special interest are the SLR-based position offsets. They exhibit a mean shift of −0.5 mm in tangential direction, and +0.6 mm in cross-track, which coincides with the PCV pattern. Changes in the PCV pattern due to updated models and applied ambiguity fixing slightly shift the lateral components of the orbit solutions.

5.3 Detailed Validation and Comparison

Within this section, the previously introduced ambiguity-fixed orbit solutions are evaluated by SLR. For this purpose, TSX-1 and TDX-1 orbit solutions obtained from the 2012–2017 period are selection. In addition, ambiguity-fixed solutions of SWC (2014–2016) and S-1A (2016) are compared to the floating PSO solutions. The S-1A orbit

Table 5.3: Satellite laser ranging residuals ($\bar{x} \pm \sigma_x$ [mm]) and amount of normal points (N_{np}) for selected ILRS stations of the TSX-1 and TDX-1 orbit validation obtained from the 2012–2017 period.

	TSX-1			TDX-1		
Station	N_{np}	PSO	ID9	N_{np}	PSO	ID9
Graz	9,966	-2.7 ± 13.6	-0.7 ± 7.3	9,299	-3.9 ± 14.0	-0.9 ± 7.9
Greenbelt	27,060	-11.8 ± 17.2	-7.5 ± 11.0	26,413	-10.4 ± 16.6	-6.8 ± 12.3
Haleakala	2,994	0.1 ± 13.5	2.3 ± 10.4	3,507	0.6 ± 14.4	3.1 ± 11.0
Hartebeesthoek	11,425	3.5 ± 20.0	6.8 ± 17.5	11,460	1.9 ± 21.0	5.4 ± 18.6
Herstmonceux	9,865	-9.1 ± 12.0	-5.7 ± 6.8	8,127	-9.7 ± 13.5	-6.2 ± 7.9
Matera	3,658	-3.7 ± 14.2	-3.7 ± 9.2	4,743	-8.5 ± 14.1	-5.1 ± 11.1
Mount Stromlo	26,925	8.0 ± 16.8	9.6 ± 12.0	30,216	7.7 ± 16.6	8.6 ± 12.7
Potsdam	14,780	-6.1 ± 14.3	-3.2 ± 9.5	12,106	-7.6 ± 14.4	-4.8 ± 10.0
Wettzell	636	4.0 ± 12.9	7.4 ± 10.1	516	-0.6 ± 13.0	3.1 ± 12.3
Yarragadee	74,533	0.8 ± 16.3	4.9 ± 8.3	64,889	1.2 ± 17.4	4.4 ± 9.7
Zimmerwald	22,825	-4.0 ± 12.9	-2.4 ± 8.2	24,230	-5.1 ± 14.2	-2.9 ± 10.7
Total	204,667	-1.5 ± 16.9	1.6 ± 11.4	195,506	-1.6 ± 17.5	1.2 ± 12.5

solutions are further employed for radar-based orbit validation. The strategy, selected networks, and applied models are available in Section 2.3.

5.3.1 Satellite Laser Ranging and Orbit Comparison

Individual series of SLR residuals obtained from TSX-1 and TDX-1 float (PSO) and GPS ambiguity-fixed (ID9) solutions are available in Table 5.3. By example, the ILRS station Graz, Austria, exhibits no bias and a standard deviation of only 8 mm, whereas Mount Stromlo, Australia, shows a bias of 10 mm, along with a standard deviation of 12 mm for both orbit solutions. Offsets in station-wise SLR residuals hint to potential deficiencies in the knowledge of the SLR station coordinates and biases, as demonstrated in Arnold et al. [2018a].

Figure 5.6 shows SLR residuals obtained from the 2012–2017 period. The associated SLR results listed in Table 5.3 demonstrate a 17.5 mm to 11.4 mm consistency across the selected stations. Basically, the SLR residuals constitute a measure of the one-dimensional orbit error.

However, a simplified correlation to the associated 3-D position error is given by $\sigma_{\text{pos}} = \sqrt{3}\sigma_{\text{SLR}}$ [Arnold et al., 2018a]. Given the standard deviations of 17.5 mm and 11.4 mm, they translate to a 3-D position error of 30 mm and 20 mm for the mentioned solutions.

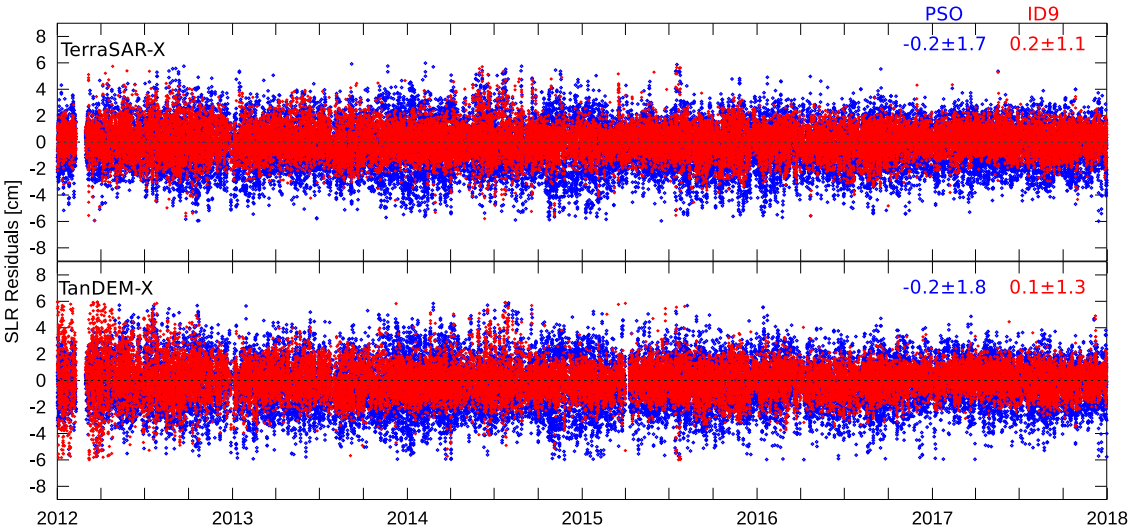

Fig. 5.6: Satellite laser ranging residuals obtained for TerraSAR-X and TanDEM-X PSO (blue) and the ID9 solutions (red).

Overall, the satellite laser ranging residuals obtained from ID9 result in a mean value of 1.6 mm and a standard deviation of 11.4 mm for TSX-1, which is similar to the TDX-1 solutions of 1.2 ± 12.5 mm. Compared to the results obtained with the precise science orbit products, the enhanced solutions show a 33% reduction of the standard deviation, which is clear evidence for the improvements achieved with this solution.

The impact of the ambiguity-fixed solutions (ID9) can be assessed by comparison to the float solutions (ID7). Satellite laser ranging residuals obtained from the aforementioned solutions and the PSOs are available in Table 5.4. While the ambiguity fixing causes a 5 mm decrease of the SLR residuals standard deviation, the mean is slightly increased by 1 mm. Overall, SLR residuals of 1.6 ± 11.4 mm, obtained from the 2012–2017 period for TSX-1, are the smallest ones. The obtained results are pretty similar for TDX-1, where the ambiguity-fixed solutions exhibit 1.2 ± 12.4 mm.

SLR residual time series are shown in Figure 5.6 for both the PSO and the ambiguity-fixed solutions. Except for short tracking outages due to certain mission campaigns, the series clearly reflect the reduced scatter in case of the ambiguity-fixed solutions. Whereas the PSO products show an increase in the standard deviation around the 2014 and 2015 winter seasons, the ambiguity-fixed solutions are free of any seasonal variations.

Table 5.4: Satellite laser ranging validation and ephemeris comparison. S-1A: 2016, CPOD as reference; SWC: 2014–2016, official precise science orbits (PSOs) as reference; TSX/TDX-1: 2012–2015 (ID7), 2012–2017 (ID9), PSOs as reference. $\bar{x} \pm \sigma_x$

SC	ID	SLR res.	SLR pos. est. [mm]			Ephemeris comparison [mm]		
		[mm]	R	T	N	R	T	N
TSX-1	PSO	-1.5 ± 16.9	-1.6 ± 2.8	2.1 ± 4.1	-11.9 ± 8.1	–	–	–
TSX-1	7	0.2 ± 16.0	1.4 ± 2.7	-0.8 ± 4.3	-8.0 ± 6.2	3.0 ± 12.0	0.0 ± 16.0	5.0 ± 14.0
TSX-1	9	1.6 ± 11.4	2.4 ± 2.7	0.4 ± 3.2	0.5 ± 1.9	3.0 ± 18.0	1.0 ± 23.0	13.0 ± 14.0
TDX-1	PSO	-1.6 ± 17.5	-2.3 ± 3.4	2.7 ± 3.4	-10.0 ± 8.0	–	–	–
TDX-1	7	-0.3 ± 16.6	1.2 ± 2.9	-0.2 ± 3.6	-7.8 ± 6.5	2.0 ± 14.0	1.0 ± 17.0	5.0 ± 15.0
TDX-1	9	1.2 ± 12.5	1.5 ± 3.1	1.8 ± 2.7	-0.1 ± 1.9	2.0 ± 21.0	1.0 ± 28.0	9.0 ± 16.0
S-1A	7	–	–	–	–	0.0 ± 12.0	-1.0 ± 20.0	-11.0 ± 13.0
S-1A	9	–	–	–	–	-2.0 ± 11.0	-2.0 ± 19.0	3.0 ± 13.0
SWC	PSO	-1.2 ± 13.3	-2.2 ± 3.0	1.0 ± 3.4	-1.6 ± 4.7	–	–	–
SWC	9	0.5 ± 11.1	0.3 ± 2.5	2.0 ± 2.6	-2.3 ± 2.1	2.0 ± 11.0	0.0 ± 16.0	-1.0 ± 14.0

For TSX-1 ambiguity fixed solutions in ID 9, the SLR-based monthly position offsets show a 1 mm shift in radial direction, compared to the float solutions in ID 7, whereas empirical accelerations are not affected (cf. Table 5.1). In along-track direction, the shift is in the same order of magnitude, whereas the cross-track component shows a 8.5 mm reduction to 0.5 ± 1.9 mm (ID7 vs. ID9). Figure 5.7 shows time series of the SLR-based monthly position offsets. It clearly shows the reduced biases and systematics when introducing integer ambiguity fixing. According to Equation 4.1 the 8.5 mm cross-track offset correspond to an acceleration of $-10.3\,\mathrm{nm/s^2}$ in cross-track direction, which is more then twice the difference between cannon-ball and macro-model for SRP (cf. Figure 4.1). The orbit solution is clearly shifted (improved) in cross-track direction, but the corresponding empirical accelerations do not show any significant reduction. The weight of the observations is kept but the solutions profit from strong geometrical/kinematic constraints. Modeling deficits can not be compensated by the float ambiguities. Similar considerations hold for TDX-1, where the ambiguity-fixed solutions exhibit cross-track offsets of -0.1 ± 1.9 mm. Compared to the float RDOD solutions, the ambiguity-fixed RDOD solutions strongly constrain the estimated trajectory of the GPS antenna. Therefore, deficiencies in the assumed GPS antenna offset from the spacecraft's COM might be the reason for the cross-track shift in ID7. A direct orbit comparison over 7 years shows mean differences of 8 mm in cross-track direction, which corresponds well to the satellite laser ranging results.

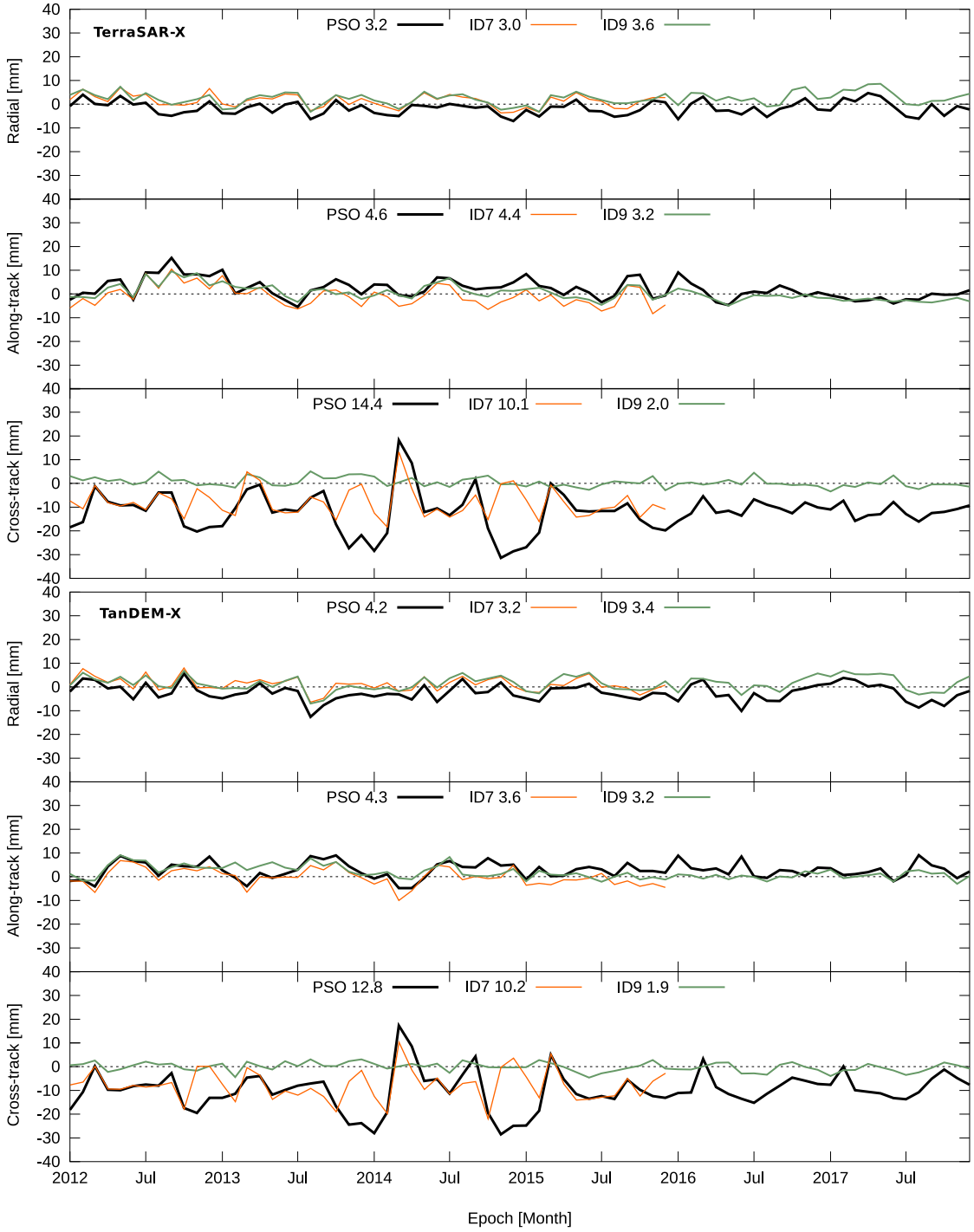

Fig. 5.7: SLR-derived monthly position estimates of TerraSAR-X and TanDEM-X; the numerical legend corresponds to the root-mean-square in mm.

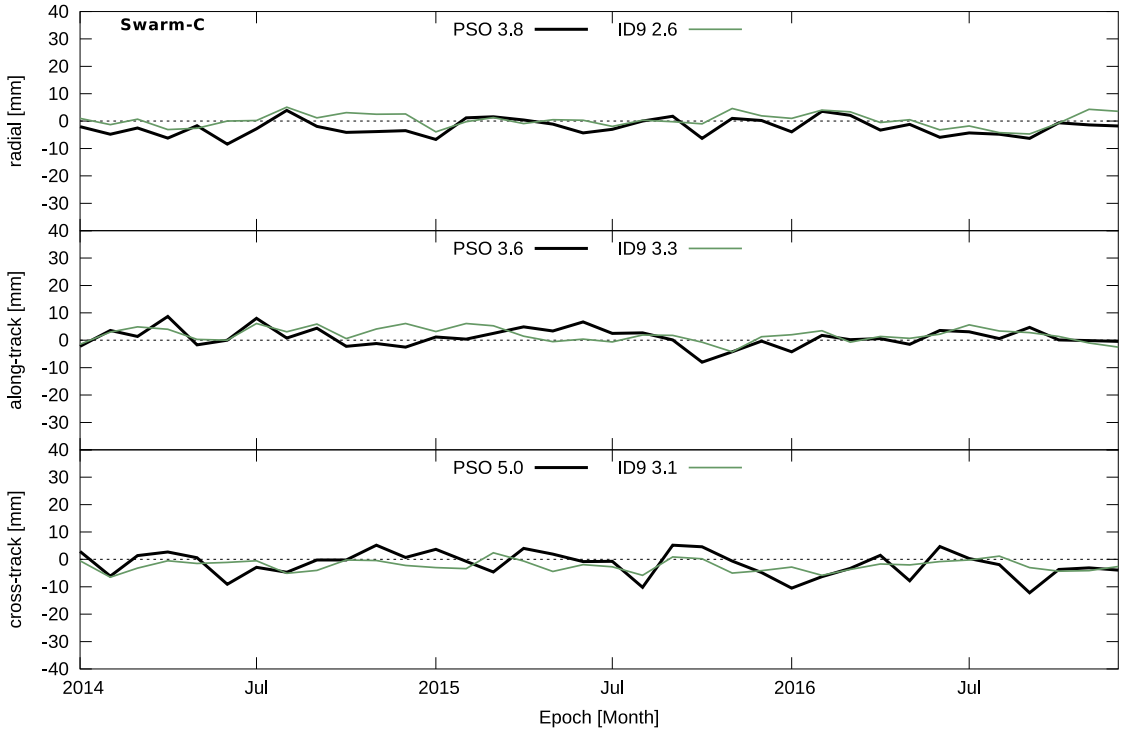

Fig. 5.8: SLR-derived monthly position estimates of Swarm-C obtained for PSOs and ambiguity-fixed solutions; the numerical legend corresponds to the root-mean-square in mm.

Differences of orbit solutions are an important performance indicator for S-1A. Obtained from the 2016 period, the orbit differences of GPS integer vs. float solutions exhibit a mean value of +8 mm in cross-track direction, which is pretty similar to the TSX-1 change. In radial and along-track direction, the mean differences are below 2 mm and, therefore, not significant. The RMS is below 20 mm for all three components, whereas the largest standard deviation is in along-tack direction with 19 mm.

SLR-based position offsets of Swarm-C are available in Figure 5.8. The induced changes by applied integer ambiguity fixing are below 3 mm and no systematics are observable in any component. According to the obtained SLR residuals, the ambiguity-fixed solutions exhibit 0.5 ± 11.1 mm, obtained from the 2014–2016 period. Compared to the official PSOs, this is an improvement of 2 mm in standard deviation, and 1.7 mm in mean.

GPS integer ambiguity fixing substantially improves the SLR-based offset estimation in cross-track direction of TSX-1/TDX-1. The dynamic model improvements in ID 7

Table 5.5: SAR residuals ($\bar{x} \pm \sigma_x$ [mm]) and underlying number of data takes (N_{dt}) for the stations with corner reflectors of the TSX-1 and TDX-1 orbit validation, obtained from the 2012–2017 period.

Station	TSX-1			TDX-1		
	N_{dt}	PSO	ID9	N_{dt}	PSO	ID9
Wettzell Range	235	-13.7 ± 13.1	-9.4 ± 10.3	66	-11.5 ± 12.9	-7.4 ± 8.1
O'Higgins Range	135	1.3 ± 16.3	1.9 ± 14.6	305	9.3 ± 15.7	7.6 ± 15.2
Metsähovi Range	178	-0.1 ± 11.2	0.3 ± 10.0	36	-0.4 ± 12.8	-0.3 ± 10.1
Wettzell Azimuth	235	10.7 ± 23.9	9.2 ± 21.9	66	5.2 ± 29.2	8.6 ± 24.6
O'Higgins Azimuth	135	18.0 ± 25.9	10.0 ± 23.7	305	-7.6 ± 28.2	0.1 ± 25.1
Metsähovi Azimuth	178	0.0 ± 17.6	0.0 ± 15.2	36	0.0 ± 18.2	0.0 ± 14.8
Total Range	548	-5.6 ± 15.1	-3.5 ± 12.5	407	5.1 ± 16.9	4.5 ± 14.9
Total Azimuth	548	9.0 ± 23.6	6.4 ± 20.9	407	-4.8 ± 28.0	1.4 ± 24.4

only cause a slight decrease of 4 mm compared to the PSOs, the fixed solutions are show a 11 mm reduction. This result is valid for TSX-1, and TDX-1, too. Whereas the science orbit solutions clearly show time-dependent systematics, the enhanced dynamical models reduce the systematics. They almost totally vanish when fixing the GPS integer ambiguities. For SWC, and obtained from three years, the SLR residuals of the ambiguity-fixed solutions amount to 0.5 ± 11 mm, which is a 17 % improvement compared to the PSOs. Again, the benefit is most pronounced for the cross-track component, which shows a 38 % reduction of the RMS position offsets.

Due to the notably high quality of the ambiguity-fixed solutions, they can even be employed for identifying systematics in the SLR observations, as indicated in Montenbruck et al. [2017]. The only pre-conditions for this technique are GPS observations, which allow integer ambiguity resolution, the WSBs, and the availability of suitable GPS satellite clocks, and associated orbit products.

5.3.2 Radar Ranging

Measurements to corner cube reflectors are provided for the spacecraft TSX-1, TDX-1, and S-1A. For TSX-1 and TDX-1, the subsequent analysis comprises measurements to three, for Sentinel to six corner cube reflectors on ground. Generally, the residuals in azimuth and range as well as the corresponding timing information are provided by the Remote Sensing Technology Institute at the DLR.

TerraSAR-X and TanDEM-X For the SAR-based orbit validation, two independent sets of residuals can be analyzed, namely a set of residuals for the range and a set of residuals for the azimuth. Table 5.5 lists the results for both types of observations as well as for TSX-1 and TDX-1. The findings show a very good agreement regarding the standard deviations across the stations and the two orbit solutions tested. With the PSOs, the standard deviation of the SAR ranging is in the order of 15 mm, while for the ID9 solution, an improvement to 10 mm is obvious. Note that the standard deviations of the GARS O'Higgins range results are larger when compared to standard deviations obtained at the other station. Part of the explanation may be found in the different CCR sizes, i.e. 0.7 m versus 1.5 m. Small reflectors cause a drop in the range localization precision by approximately 5 mm [Hackel et al., 2018]. Moreover, there is a slight tendency towards the positive range for the TDX-1 range data of GARS O'Higgins between mid 2016 to mid 2017, which is present in both orbit solutions. The effect also has an impact on the mean and standard deviations computed for this site. The much sparser data of TSX-1 for OHG indicate a similar behavior; thus it might be related to the CCR installations at GARS O'Higgins, and it is also the reason why there is less improvement in the overall TDX-1 results and the improved orbit solution, because the data is dominated by the acquisitions at OHG. Note that the CCR at MET is selected for calibration of the SAR measurements [Hackel et al., 2018], which is the reason for small residuals.

Figure 5.9 provides a comprehensive view of all the SAR ranging residuals for the ambiguity-fixed (ID9) and the PSO orbit solutions. The reason for the small number of TSX-1 data and the lack of data for TDX-1 in the first year lies in the setup of the CCR sites. During the first year, only one reflector was available at Wettzell, Germany, which was covered solely by the TDX-1 spacecraft. In spite of the details discussed for the solutions of the individual CCR sites, these combined plots confirm the very good overall consistency of both TSX-1 and TDX-1, across the sites as well as the high quality of the improved ID9 orbit solution.

As stated in the previous section, SLR enables the estimation of monthly position offsets of the spacecraft. In principle, the SAR residuals in range and azimuth allow for the same position offset analysis. However, the permanently right-looking nature of the SAR instruments yields radar ranges that basically cover only one cross-direction of the orbit, for which the ranges have an angular separation of approximately 15 to 20 degrees. The advantage of measuring all the pass geometries and the considerably larger amount of tracking data enables the SLR to reliably determine the monthly position offsets for

Fig. 5.9: Series of SAR range residuals obtained for TerraSAR-X and TanDEM-X.

all three directions with an estimated precision at the sub-millimeter level. In contrast, SAR residuals showed estimated precision for the cross-track and radial position offsets at the centimeter level, and a precision at the millimeter level for the along-track position offsets. Therefore, the SAR data is kept in the geometry of range and azimuth, but monthly averaging is applied to preserve the comparison with the SLR-based position offsets. Table 5.6 comprises the averaged values that are associated with the time series visualized in Figure 5.10. The corresponding SLR residuals are available in Table 5.4 and Figure 5.7.

Due to the observation geometry, the monthly SAR azimuth results are comparable to the monthly SLR-based position offsets in along-track direction. The comparison of both results indicate that the SLR along-track offsets are approximately $2-3$ times more reliable than the $5-7$ mm offsets found for SAR azimuth, but one should also take into account the large differences in the underlying data, namely about 2,000 NPs per month for the SLR versus the 5 to 10 SAR acquisitions per month at the CCR sites. Nevertheless, the improvement of the enhanced ambiguity-fixed orbit solutions is also clearly visible in the SAR azimuth offsets, especially in the mean value of TDX-1 that is reduced from -7.2 mm to 1.4 mm. The monthly SAR range offsets confirm the findings for the ID9 solutions. Both, mean and standard deviation are at the level of 10 mm. Note

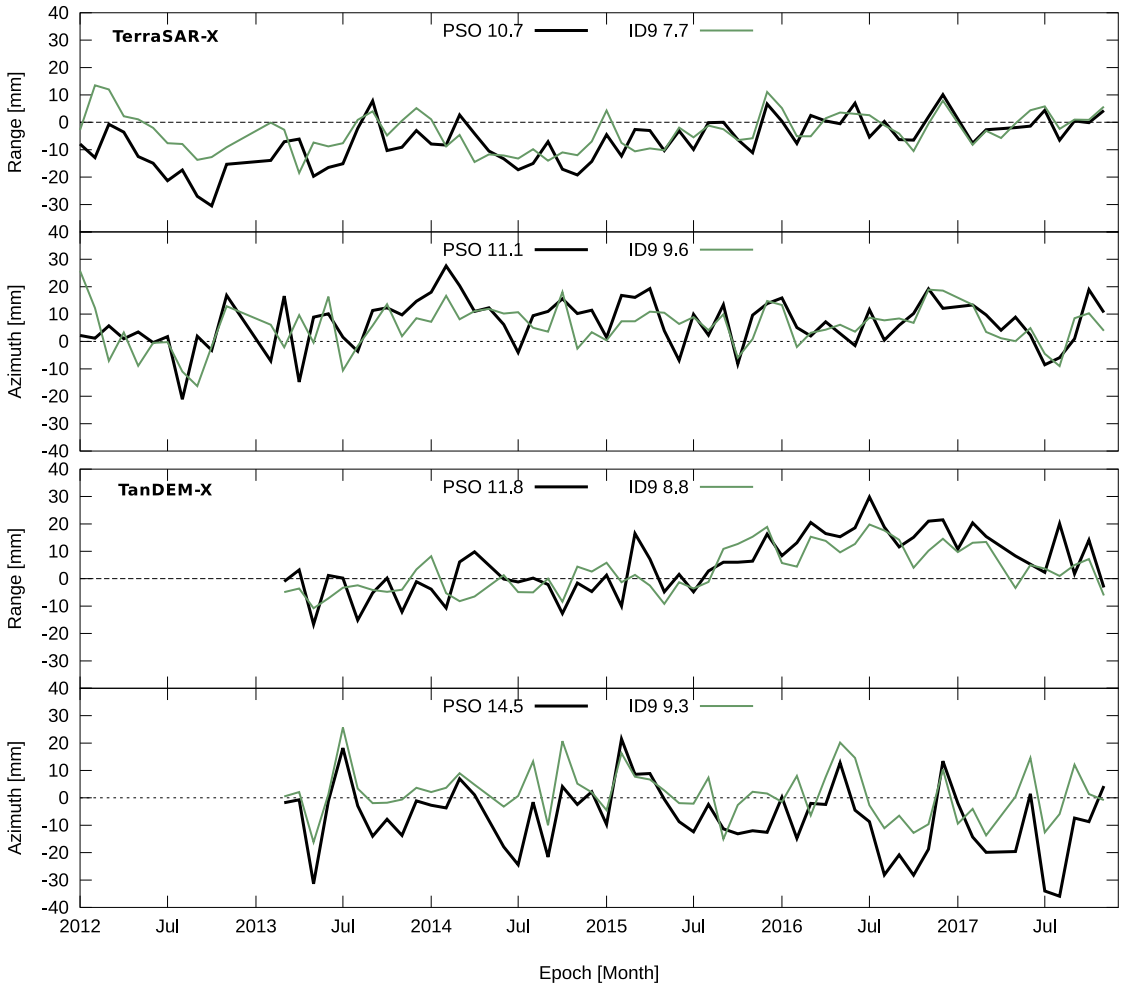

Fig. 5.10: Series of monthly SAR residuals in range and azimuth for TerraSAR-X and TanDEM-X.

Table 5.6: Orbit validation using syhthetic aperture radar measurements. TSX/TDX-1: 2012 – 2017; S-1A: 2016. $\bar{x} \pm \sigma_x$.

SC	ID	Range [mm]	Azimuth [mm]	Range offsets monthly [mm]	Azimuth offsets monthly [mm]
TSX-1	PSO	-5.6 ± 15.1	9.0 ± 23.6	-6.8 ± 8.2	6.7 ± 8.9
TSX-1	9	-3.5 ± 12.5	6.4 ± 20.9	-3.4 ± 6.9	5.4 ± 7.9
TDX-1	PSO	5.1 ± 16.9	4.5 ± 14.9	5.1 ± 10.6	-7.2 ± 12.6
TDX-1	9	-4.8 ± 28.0	1.4 ± 24.4	3.1 ± 8.3	1.4 ± 9.2
S-1A	PSO	–	–	-0.4 ± 22.4	-5.8 ± 152.6
S-1A	9	–	–	0.0 ± 23.6	4.7 ± 151.0

that the slightly larger numbers for TDX-1 are due to the systematics in the OHG data during the years 2016 and 2017, which was already discussed in the previous section and can be seen once more in the Figure 5.10. In summary, both techniques agree in their monthly assessment of the TerraSAR-X orbit solutions.

Sentinel-1A For Sentinel-1A, a couple of constraints limit the capabilities of the SAR analysis. First, only the interferometric wide swath (250 km swath with 5 m×20 m resolution) standard products in Terrain Observation with Progressive scans SAR (TOPSAR) [Kubica et al., 2015] are available for this analysis which require relatively large corner cube reflectors to gain a high level of precision. Secondly, the radar image generation processing chain is currently under development and not in operational mode. The selected, largest corner cubes of Geoscience Australia have a corner length of 2 m, and 2.5 m. These conditions cause an increased standard deviation of range and azimuth, which basically makes a proper analysis difficult. Typically, all corner cubes of the Australian network are visible in one data take. Since the precision of the measurements is rather limited, Figure 5.11 illustrates the scatter of individual measurements by the error bars. Compared to TSX-1 and TDX-1, the level of range and azimuth residuals are one magnitude worse and it is not possible to clearly see any improvement through the orbit solutions.

Exploiting the SAR measurements for validating the satellite orbits offers a new, independent technique. Especially the relative easy setup of the corner cubes and their compact size theoretically allows a high density of reflectors which could also be employed for e.g. detecting plate tectonics. The only limitation is that the corner cubes fit to the SAR observation mode and wavelength and that the corner cubes require some maintenance (e.g. snow).

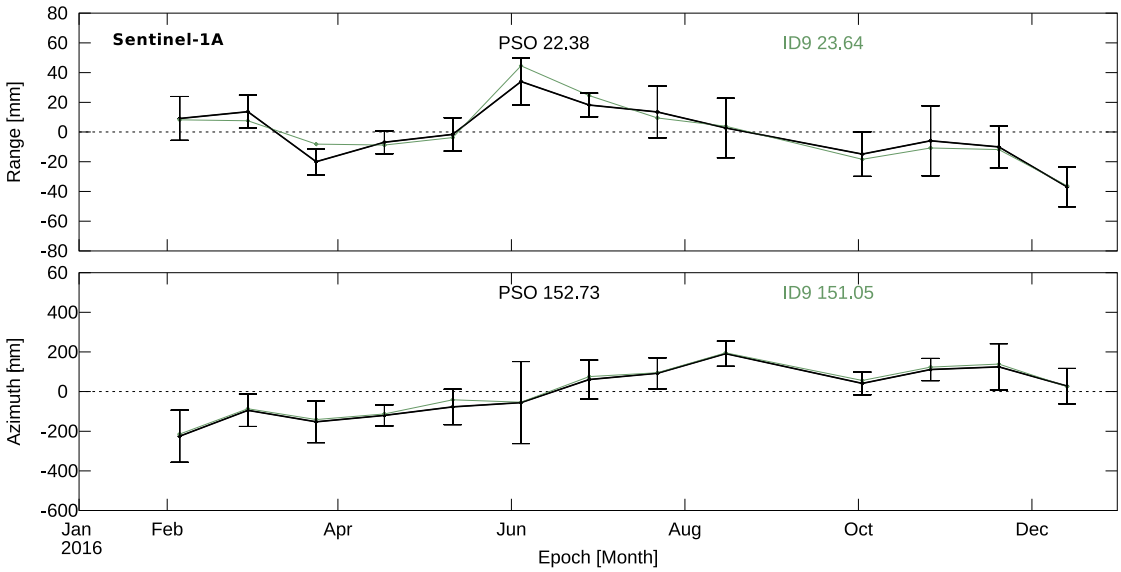

Fig. 5.11: Series of monthly SAR residuals in range and azimuth for Sentinel-1A.

In summary, the combination of corner reflectors with reference coordinates and the orbit solution allows for the computation of residuals in range and azimuth using the radar measurements. The correction of the atmospheric path delay in the measurements and the modeling of the reference coordinates according to the geodetic conventions ensure accurate SAR-based residuals, which are also useful when testing different orbit solutions. Like in the case of SLR, the SAR residuals may be interpreted as orbital errors and can in principle be decomposed into radial, along-track and cross-track residuals. However, it has to be emphasized that the SAR provides only one range per pass, i.e. the range at the instant of zero-Doppler, and the corresponding azimuth is basically the along-track error, whereas the SLR enables the tracking of the entire pass.

6

Conclusions and Recommendations

6.1 Conclusions

The present study assesses the impact of refining the employed dynamical models and GPS processing techniques, aiming at a trade off between precise orbit solutions and the need of empirical accelerations. The benefit of using such models and techniques is assessed through different performance metrics including self-consistency tests, SLR, and radar ranging as an external validation technique.

For assessing the orbit solutions, and besides reduced-dynamic 'internal' quality indicators like scaling parameters or empirical accelerations, SLR serves as independent validation technique. SLR observations are also utilized to derive SLR-based position offsets of the spacecraft. In addition, radar measurements are used as independent validation technique. Model improvements basically include satellite macro models combined with improved solar/Earth radiation pressure and aerodynamic acceleration models. Integer ambiguity fixing is introduced to fully exploit the potential of the involved GPS measurements. The study comprises the missions Sentinel-1A, Swarm-C, and TerraSAR-X/TanDEM-X with an altitude of 450 km to 693 km.

Use of advanced atmospheric density models and the spacecraft macro model for atmospheric forces is found to slightly reduce the associated empirical accelerations but does not allow to entirely waive the estimation of such parameters. Updating the atmospheric density model from Jacchia-71G to NRLMSISE-00 led to a 1 nm/s^2 empirical acceleration reduction in along-track direction and slightly shifts the orbit solution in lateral direction by 2 mm, as assessed through the SLR-based monthly position offset estimates.

The present study makes use of a satellite macro model, which decomposes the real spacecraft shape in several plates, each with it's own geometry and optical properties. Herein, the required information is provided by the spacecraft's manufacturer. The derived model is then applied to compute radiation pressure accelerations in the reduced-dynamic approach.

With respect to radiation pressure, the macro model appears vital for a realistic description of ERP. In particular, it benefits the modeling of the radial ERP acceleration, which directly impacts the height leveling of the resulting orbit, and is such of key relevance for altimetry missions. The resulting orbit solutions of TerraSAR-X show a significantly reduced SLR bias from -1.6 mm to 0.2 mm. This largely corresponds to an acceleration of 10 nm/s^2, which is the pure contribution of Earth radiation pressure. In addition, also the SLR-based position offsets show a shift of 2 mm in radial, and cross-track direction.

The quality of involved GPS microwave observations heavily depends on the ionosphere, and associated effects. Generally, first-order ionospheric effects are eliminated by the ionosphere-free linear combination. Assessing higher-order ionospheric effects and their impact on the orbit solutions showed, that they do not influence the solutions in a significant matter.

The full potential of the GPS phase observations is exploited by estimating carrier phase ambiguities as float parameters and discarding their integer nature. It is shown that resolving the float ambiguities and fixing them to integers notably improves the resulting orbit solutions. Compared to the operational science orbits of TerraSAR-X, the ambiguity-fixed solutions exhibit a significantly improved cross-track offset, which decreases from -12.2 mm in case of the standard orbits, down to 0.8 mm in terms of SLR-based position offsets. Especially the cross-track component appears to be totally free of any systematical effects. The SLR residuals itself are reduced from 17.6 mm to 12.1 mm (RMS), which is 4 mm better then the best refined dynamical solution with floating ambiguities. Moreover, the ambiguity-fixed solutions also exhibit a much better

internal consistency in terms of SLR standard deviation, which is decreased by 5.5 mm. The results of TerraSAR-X are similar to those derived from TanDEM-X. The results are also underlined by orbit solutions of Swarm-C and Sentinel-1A. The Swarm-C PSO solutions exhibit SLR residuals of 13.4 mm (RMS), whereas the ambiguity-fixed solutions show significantly reduced residuals of 11.0 mm (RMS). For Sentinel-1A, which is not equipped with a SLR retroreflector, ephemeris comparisons show a radial difference between float and fixed solutions of −2 mm. With respect to GPS observation modeling, the use of ambiguity fixing is shown as a key technique to achieve improved orbit determination accuracy for all orbit geometries. Its benefit largely outweigh that of non-gravitational force models and contribute to major improvements in the horizontal (along-track/cross-track) position knowledge. On the other hand, the reduced vertical dilution of precision still makes the resulting orbit solutions sensitive to geometric orbit modeling errors in radial direction and justifies the use of refined radial acceleration models.

Based on the updated orbit solutions, also the derived SAR residuals underline the statement that ambiguity-fixing significantly improves the quality of the derived orbit solutions. As an example, the SAR range residuals of TerraSAR-X are at 10.1 mm RMS in case of the operational products, and decrease to 7.8 mm (28 %) in case of the ambiguity-fixed solutions. Simultaneously to the range residuals, also the SAR residuals in azimuth show a decrease of 14 %. The derived results correspond well to the SLR-based results, although both validation technique are totally independent. However, it is not yet fully competitive with SLR in terms of both accuracy and coverage.

6.2 Recommendations for Precise Orbit Determination

As assessed through the present study for low Earth orbiters and combined with the chosen reduced-dynamic orbit determination approach, utilization of modern gravity and ocean tide models improves the orbit solutions. The satellite macro model in combination with the Earth radiation pressure modeling further improves the radial leveling of the resulting solutions.

However, getting reliable information for macro model generation is of vital importance for the macro model generation. Especially the required optical properties in infrared and visual spectra, which are individual for each satellite plate, are hard to obtain and

depend on input from the satellite manufacturer. The assumed 10 % uncertainty in the derived optical coefficients can be well absorbed by the associated scaling parameters.

A significantly improved lateral leveling can be achieved by GPS integer ambiguity fixing, which fully exploits the potential of GPS carrier phase measurements in the reduced-dynamic approach. Due to less degrees of freedom, it is recommended to combine the ambiguity fixing with enhanced non-gravitational force models.

6.3 Outlook for Further Research

With respect to the macro model, an assessment of shadowing effects, thermal effects, and aging of optical properties would be of interest. For shadow, the macro model builds the basis for vector line-of-sight computations, also known as ray-tracing. Studies have already demonstrated the effect of such models, especially for spacecraft with huge solar arrays [Ziebart, 2001].

The thermal effects are pretty complex and require thermal models. As an example, the solar arrays collect energy up to several kW, which needs to be emitted in any form of radiation. Simple considerations are also available in the present study (thermal re-radiation of absorbed radiation), but complex thermal models are not considered since they require knowledge of heat dissipation and thermal control in the satellite's interior. In addition, an assessment of aging effects of the materials on the satellite surface, might be interesting. Wernham [2013] demonstrates that coated surfaces change their reflectivity up to 50 % during their life (BOL to EOL). Detailed studies on estimating the optical coefficients would be an interesting continuation of the present study.

Next, the focus is on the ambiguity-fixed orbit solutions. In the presented approach, required satellite clocks and wide-lane biases are published by CNES. However, also other agencies like the Jet Propulsion Laboratory (JPL) or the CODE [Arnold et al., 2018b] distribute such auxiliary data. An inter-agency comparison of the products and derived ambiguity-fixed orbit solutions would help to validate the products and to understand the remaining empirical accelerations.

Acknowledgements

The present study was possible through support of Munich Aerospace, embedded in the project Hochauflösende Geodätische Erdbeobachtung at the TUM and the DLR. In addition, I would like to thank Spaceflight Technology and Flight Dynamics at the GSOC/DLR for their profound and widespread support. Special thanks to Peter Steigenberger for proofreading the present thesis. Many thanks also to my colleagues at the Institute of Remote Sensing, for all the fruitful discussions. Special thanks to Christoph Gisinger for his cooperation and the the radar-based analysis. Moreover, I would also like to thank the Astronomisches Institut at the University of Bern and the Astrodynamics and Space Missions Department at TU Delft, who greatly supported verifying the implemented models. Many thanks also to the Sentinel Working Group, who kindly provided the required data for Sentinel POD. Last but not least I would thank my family, who supported me all the way to reach this level of education.

There are no adjectives describing your support, Oliver – thank you.

List of Acronyms

Airbus DS Airbus Defence and Space
ANTEX antenna exchange
ARP antenna reference point
ATCS active thermal control system
AU astronomical unit

BOL begin of lifetime

CAD computer-aided design
cbl cannon-ball
CCR corner cube reflector
CERES Clouds and Earth's Radiant Energy System
CESS coarse Earth Sun sensors
CHAMP CHAllenging Minisatellite Payload
CIRA-72 COSPAR International Reference Atmosphere 1972
CIRA-86 COSPAR International Reference Atmosphere 1986
CNES Centre National d'Etudes Spatiales
CODE Center for Orbit Determination in Europe
COM center of mass
COSPAR Committee On Space Research
CP carrier phase
CPOD Copernicus POD
CSR Center for Space Research

DD double-difference
DEM digital elevation model
DLR Deutsches Zentrum für Luft- und Raumfahrt
DOY day of year
DTM Drag Temperature Model
DTM 2012 Drag Temperature Model 2012
DTM 2013 Drag Temperature Model 2013

EOL end of lifetime
EOP Earth orientation parameter
ERP Earth radiation pressure
ERS-1 European Remote Sensing Satellite 1
ESA European Space Agency
EUV extreme ultraviolet

$F_{10.7}$ Flux 10.7 cm
FES2004 Finite Element Solution 2004

GARS German Antarctic Receiving Station
GFZ Deutsches GeoForschungsZentrum
GHOST GNSS High Precision Orbit Determination Software Tools
GMES Global Monitoring for Environment and Security
GMV Grupo Mecánica del Vuelo
GNSS Global Navigation Satellite System
GOCE Gravity field and steady-state Ocean Circulation Explorer
GOCO03s Gravity Observation COmbination 03s
GPS Global Positioning System
GRACE Gravity Recovery And Climate Experiment
GSOC German Space Operations Center

H Hydrogen
He Helium
HWM-07 Horizontal Wind Model 2007

ID identification
IERS International Earth Rotation and Reference Systems Service
IF ionosphere-free
IGOR integrated geodetic and occultation receiver
IGRF-12 International Geomagnetic Reference Field 12
IGS International GNSS Service
ILRS International Laser Ranging Service
IR infrared

JPL Jet Propulsion Laboratory

LCT laser communication terminal
LEO low Earth orbit
LEOP launch and early orbit phase
LRR laser retro reflector

mac macro
MagSat Magnetic Field Satellite
MET Metsähovi
MetOp Meteorological Operational Satellite
MLI multilayer insulation
MSIS Mass Spectrometer Incoherent Scatter

MW Melbourne-Wübbena

N normal/cross-track
N_2 molecular nitrogen
NASA National Aeronautics and Space Administration
NL narrow-lane
NOAA National Oceanic and Atmospheric Administration
NP normal point
NRL US Naval Research Observatory
NRLMSISE-00 US Naval Research Laboratory Mass Spectrometer and Incoherent Scatter Radar 2000

O atomic oxygen
O_2 molecular oxygen
OHG O'Higgins
OSR optical solar reflector

PCO phase center offset
PCV phase center variation
PEC patch excited cup
POD precise orbit determination
PR pseudorange
PRIMA Piattaforma Riconfigurabile Italiana Multi-Applicativa
PRN pseudo-random noise
PSO precise science orbit
PTCS passive thermal control system
PWU phase wind up

R radial
RDOD reduced-dynamic orbit determination
RMS root mean square
RTN radial, tangential, and normal
RUAG RüstungsUnternehmen-AktienGesellschaft

S-1A Sentinel-1A
SAC-C Satélite de Aplicaciones Científicas-C
SAR Synthetic Aperture Radar
SCR signal-to-clutter ratio
SFU solar flux units
SLR satellite laser ranging
SMM Solar Maximum Mission
snt Sentman
SOHO Solar and Helospheric Observatory
SPWC SPace Weather Center
SRP solar radiation pressure
SRTM Shuttle Radar Topography Mission
SWC Swarm-C

T tangential/along-track

T/P Topex/Poseidon
TDX-1 TanDEM-X
TEC total electron content
TOA top of atmosphere
TOPSAR Terrain Observation with Progressive scans SAR
TOR tracking, occultation, and ranging
TSX-1 TerraSAR-X
TUM Technische Universität München

UT universal time
UTC universal time coordinated

VIS visual

WL wide-lane
WSB wide-lane satellite bias
WTZ Wettzell

List of Symbols

Greek letters

α	absorption
δ	diffusive reflection
ϵ	emissivity
Γ	accommodation coefficient
γ	scaling factor
κ	density
λ	wavelength
μ	specularity
ν	reflectivity
ω	phase wind-up
φ	carrier phase
ϖ	angular speed
ρ	specular reflection
ϱ	geometric range
θ	angle btw. normal and incident
ξ	pseudorange PCO/PCV correction
ζ	carrier phase PCO/PCV correction

Roman letters

A	area (size)
ap	geomagnetic index
c	speed of light
C_{D}	aerodynamic scaling coefficient
C_{E}	ERP scaling coefficient

C_R	SRP scaling coefficient
$\boldsymbol{e}$	unit vector
I	code delay and phase advance
i	counter
j	atmospheric constituents
k	Boltzmann constant
kp	geomagnetic index
L_1	carrier phase 1
L_2	carrier phase 2
M	molecular weight
m	mass
N_A	Avogadro constant
$\boldsymbol{n}$	normal vector
N_1	L_1 ambiguities
P	pass number
p	pseudorange
$\boldsymbol{r}$	position vector
S	speed ratio
g	gravitational acceleration
t	time
$\boldsymbol{v}$	velocity vector

Symbols

$\oplus$	Earth
$\odot$	Sun

Bibliography

Adhya S (2005) Thermal re-radiation modelling for the precise prediction and determination of spacecraft orbits. PhD thesis, University College of London

Airbus DS (2014) MosaicGNSS Receiver. Airbus DS, URL http://spaceequipment.airbusdefenceandspace.com/avionics/gnss-receivers/mosaic/, online accessed on 2016/01/21

American Institute of Aeronautics and Astronautics (2004) American national standard – guide to reference and standard atmosphere models. Tech. rep., American National Standards Institute, ANSI/AIAA G-003B-2004

Arnold D, Montenbruck O, Hackel S, Sośnica K (2018a) Satellite laser ranging to low earth orbiters – orbit and network validation. Journal of Geodesy submitted on Sept. 25, 2017, DOI 10.1007/s00190-018-1140-4

Arnold D, Schaer S, Villiger A, Dach R, Jäggi A (2018b) Undifferenced ambiguity resolution for GPS-based precise orbit determination of low Earth orbiters using the new CODE clock and phase products. In: International GNSS Workshop, Wiuhan, China

Aschbacher J, Milagro-Perez MP (2012) The European Earth monitoring GMES programme: status and perspectives. Remote Sensing of Environment 120:3–8, DOI 10.1016/j.rse.2011.08.028

Attema E, Bertoni R, Bibby D, Carbone A, di Cosimo G, Geudtner D, Giulicchi L, Loyerkas S, Navas-Traver I, Ostergaard A, Snoeij P, Torres R (2012) Sentinel-1: ESA's Radar Observatory Mission for GMES Operational Services. ESA SP-1322/1, ESA Communications, ISBN 978-92-9221-418-0

Balss U, Cong XY, Brcic R, Rexer M, Minet C, Breit H, Eineder M, Fritz T (2012) High precision measurement on the absolute localization accuracy of TerraSAR-X. In: 2012 IEEE International Geoscience and Remote Sensing Symposium, Munich, Germany, pp 1625–1628, DOI 10.1109/IGARSS.2012.6351217

Balss U, Gisinger C, Cong XY, Eineder M, Brcic R (2013) Precise 2-D and 3-D ground target localization with TerraSAR-X. International Archives of the Photogrammetry, Remote Sensing and Spatial Information Science (ISPRS) XL-1(W1):23–28, DOI 10.5194/isprsarchives-XL-1-W1-23-2013

Bamler R, Hartl P (1998) Synthetic aperture radar interferometry. Inverse Problems 14(4):R1–R54, DOI 10.1088/0266-5611/14/4/001

Barkstrom BR (1984) The Earth Radiation Budget Experiment (ERBE). Bull Am Meteorol Soc 65(11):1170–1185, DOI 10.1175/1520-0477

Bartels J, Heck N, Johnston H (1939) The three-hour-range index measuring geomagnetic activity. Journal of Geophysical Research 44(4):411–454, DOI 10.1029/TE044i004p00411

Bassiri S, Hajj GA (1993) Higher-order ionospheric effects on the GPS observable and means of modeling them. NASA STI/Recon Technical Report A 95:1071–1086

Berger C, Biancale R, Ill M, Barlier F (1998) Improvement of the empirical thermospheric model DTM: DTM94 – a comparative review of various temporal variations and prospects in space geodesy applications. Journal of Geodesy 72(3):161–178, DOI 10.1007/s001900050158

Bertiger W, Desai SD, Haines B, Harvey N, Moore AW, Owen S, Weiss JP (2010) Single receiver phase ambiguity resolution with GPS data. Journal of Geodesy 84(5):327–337, DOI 10.1007/s00190-010-0371-9

Beutler G, Jäggi A, Mervart L, Meyer U (2010) The celestial mechanics approach: theoretical foundations. Journal of Geodesy 84(10):605–624, DOI 10.1007/s00190-010-0401-7

Bird GA (1994) Molecular gas dynamics and the direct simulation of gas flows. In: Oxford Engineering Science Series, vol 42, Clarendon Press, pp 476–495

Bock H, Dach R, Jäggi A, Beutler G (2009) High-rate GPS clock corrections from CODE: support of 1 Hz applications. Journal of Geodesy 83(11):1083–1094, DOI 10.1007/s00190-009-0326-1

Bock H, Jäggi A, Meyer U, Visser P, van den IJssel J, van Helleputte T, Heinze M, Hugentobler U (2011) GPS-derived orbits for the GOCE satellite. Journal of Geodesy 85(11):807–818, DOI 10.1007/s00190-011-0484-9

Bohlin JD, Frost KJ, Burr PT, Guha AK, Withbroe GL (1980) Solar Maximum Mission. Solar Physics 65(1):5–14, DOI 10.1007/BF00151380

Böhm J, Schuh H (eds) (2013) Atmospheric Effects in Space Geodesy. Springer Atmospheric Sciences, Springer International Publishing

Bowman BR, Tobiska WK, Marcos FA, Valladares C (2008) The JB2006 empirical thermospheric density model. Journal of Atmospheric and Solar-Terrestrial Physics 70(5):774–793, DOI 10.1016/j.jastp.2007.10.002

Brekke A (2013) Physics of the Upper Polar Atmosphere. Springer Berlin Heidelberg, DOI 10.1007/978-3-642-27401-5, ISBN 978-3-642-27400-8

Bronstein IN, Semendjajew KA, Musiol G, Muehlig H (2008) Taschenbuch der Mathematik. 7, Harri Deutsch

Bruinsma S (2015) The DTM-2013 thermosphere model. Journal of Space Weather and Space Climate 5(A1):1–8, DOI 10.1051/swsc/2015001

Bruinsma SL, Sánchez-Ortiz N, Olmedo E, Guijarro N (2012) Evaluation of the DTM-2009 thermosphere model for benchmarking purposes. Journal of Space Weather and Space Climate 2(A04):1–14, DOI 10.1051/swsc/2012005

Buckreuss S, Balzer W, Mühlbauer P, Werninghaus R, Pitz W (2003) The TerraSAR-X satellite project. In: IEEE IGARSS, vol 5, pp 3096–3098, DOI 10.1109/IGARSS.2003.1294694

Budden KG (1985) The propagation of radio waves: the theory of radio waves of low power in the ionosphere and magnetosphere. Cambridge University Press, ISBN 978-0521369527

Bychkov VL, Golubkov GV, Nikitin AI (2014) The Atmosphere and Ionosphere – Elementary Processes, Monitoring, and Ball Lightning. Springer Berlin Heidelberg, DOI 10.1007/978-3-319-05239-7, ISBN 978-3-319-05238-0

Capderou M (2014) Handbook of Satellite Orbits. Springer International Publishing, DOI 10.1007/978-3-319-03416-4, ISBN 978-3-319-03415-7

Cerri L, Berthias JP, Bertiger WI, Haines BJ, Lemoine FG, Mercier F, Ries JC, Willis P, Zelensky NP, Ziebart M (2010) Precision orbit determination standards for the Jason series of altimeter missions. Marine Geodesy 33(S1):379–418, DOI 10.1080/01490419.2010.488966

Colombo OL (1989) The dynamics of global positioning system orbits and the determination of precise ephemerides. Journal of Geophysical Research 94(B7):9167–9182, DOI 10.1029/JB094iB07p09167

Couhert A, Cerri L, Legeais JF, Ablain M, Zelensky NP, Haines BJ, Lemoine FG, Bertiger WI, Desai SD, Otten M (2015) Towards the 1 mm/y stability of the radial orbit error at regional scales. Advances in Space Research 55(1):2–23, DOI 10.1016/j.asr.2014.06.041

Cumming IG, Wong FH (2005) Digital Processing of Synthetic Aperture Radar Data. Artech House

Dach R, Brockmann E, Schaer S, Beutler G, Meindl M, Prange L, Bock H, Jäggi A, Ostini L (2009) GNSS processing at CODE: status report. Journal of Geodesy 83(3-4):353–365, DOI 10.1007/s00190-008-0281-2

Dach R, Lutz S, Walser P, Fridez P, Andritsch F, Arnold D, Bertone S, Jäggi A, Jean Y, Maier A, Mervart L, Meyer U, Orliac E, Ortiz–Geist E, Prange L, Scaramuzza S, Schaer S, Sidorov D, Sušnik A, Villiger A, Baumann C, Beutler G, Bock H, Gäde A, Meindl M, Ostini L, Sośnica K, Steinbach A, Thaller D, Brockmann E, Ineichen D, Hugentobler U, Rodriguez-Solano C, Steigenberger P, Fritsche M, Rülke A (2015) Bernese GNSS Software Version 5.2. Astronomical Institute, University of Bern, Bern, DOI 10.7892/boris.72297

Doornbos E (2011) Thermospheric density and wind determination from satellite dynamics. PhD thesis, Technical University Delft

Drob DP, Emmert JT, Crowley G, Picone M, Shepherd GG, Skinner W, Hays P, Niciejewski RJ, Larsen M, She CY, Meriwether JW, Hernandez G, Jarvis MJ, Sipler DP, Tepley CA, O'Brien MS, Bowman JR, Wu Q, Murayama Y, Kawamura S, Reid IM, Vincent RA (2008) An empirical model of the Earth's horizontal wind fields: HWM07. Journal of Geophysical Research 113(A12):123–139, DOI 10.1029/2008JA013668

Duchossois G, Fea M (1993) ERS-1 one year after! status and perspectives of the ERS programme. Advances in Space Research 5(5):5–18, DOI 10.1016/0273-1177(93)90522-D

Eanes RJ, Bettadpur S (1995) The CSR 3.0 global ocean tide model: Diurnal and semi-diurnal ocean tides from TOPEX/Poseidon altimetry. Tech. Rep. 6, Center for Space Research, University of Texas at Austin

Eineder M, Runge H, Boerner E, Bamler R, Adam N, Schättler B, Breit H, Suchandt S (2003) SAR interferometry with TerraSAR-X. In: Proceedings of Fringe Workshop, Frascati, Italy

Farr TG, Rosen PA, Caro E, Crippen R, Duren R, Hensley S, Kobrick M, Paller M, Rodriguez E, Roth L, Seal D, Shaffer S, Shimada J, Umland J, Werner M, Oskin M, Burbank D, Alsdorf D (2007) The Shuttle Radar Topography Mission. Reviews of Geophysics 45(2):1–33, DOI 10.1029/2005RG000183

Fernandez J, Femenias P (2014) Sentinels POD service operations. In: SpaceOps 2014 Conference, SpaceOps Conferences, AIAA, DOI 10.2514/6.2014-1929

Fiedler H, Krieger G (2004) Close formation flight of passive receiving micro-satellites. In: Proceedings of 18th International Symposium on Space Flight Dynamic, Munich, Germany

Fiedler H, Boerner E, Mittermayer J, Krieger G (2005) Total zero Doppler steering – a new method for minimizing the Doppler centroid. IEEE Geoscience and Remote Sensing Letters 2(2):141–145, DOI 10.1109/LGRS.2005.844591

Fliegel HF, Gallini TE, Swift ER (1992) Global positioning system radiation force model for geodetic applications. Journal of Geophysical Research 97(B1):559–568, DOI 10.1029/91JB02564

Flohrer C, Otten M, Springer T, Dow J (2011) Generating precise and homogeneous orbits for Jason-1 and Jason-2. Advances in Space Research 48(1):152–172, DOI 10.1016/j.asr.2011.02.017

Floyd L, Newmark J, Cook J, Herring L, McMullin D (2005) Solar EUV and UV spectral irradiances and solar indices. Journal of Atmospheric and Solar-Terrestrial Physics 67(1–2):3–15, DOI 10.1016/j.jastp.2004.07.013

Freeden W, Rummel R (2017) Erdmessung und Satellitengeodäsie. Springer Berlin Heidelberg, DOI 10.1007/978-3-662-47100-5, ISBN 978-3-662-47099-2

Freeden W, Nashed MZ, Sonar T (2010) Handbook of Geomathematics. Springer International Publishing, DOI 10.1007/978-3-642-01546-5, ISBN 978-3-642-01545-8

Friis-Christensen E, Lühr H, Knudsen D, Haagmans R (2008) Swarm – an earth observation mission investigating geospace. Advances in Space Research 41(1):210–216, DOI 10.1016/j.asr.2006.10.008

Fritsche M, Dietrich R, Knöfel C, Rülke A, Vey S, Rothacher M, Steigenberger P (2005) Impact of higher-order ionospheric terms on GPS estimates. Geophysical Research Letters 32(23):1–5, DOI 10.1029/2005GL024342

Fritz T, Eineder M (2013) TerraSAR-X ground segment basic product specification document. TX-GS-DD-3302, v1.9, 09.10.2014, `https://sss.terrasar-x.dlr.de/docs/TX-GS-DD-3302.pdf`. Online accessed on 2018/03/26.

Garthwaite MC (2017) On the design of radar corner reflectors for deformation monitoring in multi-frequency InSAR. Remote Sensing 9(7):648–672, DOI 10.3390/rs9070648

Garthwaite MC, Hazelwood M, Nancarrow S, Hislop A, Dawson JH (2015) A regional geodetic network to monitor ground surface response to resource extraction in the northern Surat Basin, Queensland. Australian Journal of Earth Sciences 62(4):469–477, DOI 10.1080/08120099.2015.1040073

Gerlach C, Földvary L, Švehla D, Gruber T, Wermuth M, Sneeuw N, Frommknecht B, Oberndorfer H, Peters T, Rothacher M, Rummel R, Steigenberger P (2003) A CHAMP-only gravity field model from kinematic orbits using the energy integral. Geophysical Research Letters 30(20):1–14, DOI 10.1029/2003GL018025

Gill E (1996) Smooth bi-polynominal interpolation of Jacchia 1971 atmospheric densities for efficient satellite drag computation. DLR-GSOC IB 96-1, German Aerospace Center

Gill E, Montenbruck O (2004) Comparison of GPS-based orbit determination concepts. In: Proceedings of the 18th International Symposium on Space Flight Dynamics

Gilmore DG (2002) Appendix a: Surface optical property data. In: Gilmore DG (ed) Spacecraft Thermal Control Handbook, The Aerospace Press

Gilmore DG, Stuckey WK, Fong M (2002) Chapter 5: Thermal surface finishes. In: Gilmore DG (ed) Spacecraft Thermal Control Handbook, The Aerospace Press

Gisinger C, Gernhard S, Auer S, Balss U, Hackel S, Pail R, Eineder M (2015) Absolute 4-D positioning of persistent scatterers with TerraSAR-X by applying geodetic stereo SAR. In: Geoscience and Remote Sensing Symposium (IGARSS), 2015 IEEE International, DOI 10.1109/IGARSS.2015.7326444

GMES Sentinel-1-Team (2012) GMES Sentinel-1 System Requirements Document, ES-RS-ESA-SY-0001. http://emits.sso.esa.int/emits-doc/ESTEC/4782-annex-a.pdf, online accessed on 2017/08/24

Gregory JC, Peters PN (1987) A measurement of the angular distribution of 5 eV atomic oxygen scattered off a solid surface in earth orbit. In: Boffi V, Cercignan C (eds) Proceedings of the 15th international symposium on rarefied gas dynamics, B.G. Teubner, Stuttgart, pp 644–656

Grunwaldt L, Flechtner F, Rothacher M (2006) GRACE Laser Retro Reflector user manual. Tech. Rep. 1.1, GFZ Potsdam

Hackel S, Montenbruck O, Steigenberger P, Balss U, Gisinger C, Eineder M (2017) Model improvements and validation of TerraSAR-X precise orbit determination. Journal of Geodesy 91(5):547—-562, DOI 10.1007/s00190-016-0982-x

Hackel S, Gisinger C, Balss U, Wermuth M, Montenbruck O (2018) Long-term validation of TerraSAR-X and TanDEM-X orbit solutions with laser and radar measurements. Remote Sensing 10(762):1–20, DOI 10.3390/rs10050762

Haines BJ, Armatys MJ, Bar-Sever YE, Bertiger WI, Desai SD, Dorsey AR, Lane CM, Weiss JP (2011) One-centimeter orbits in near-real time: The GPS experience on OSTM/Jason-2. Journal of Astronautical Sciences 58(3):445–459, DOI 10.1007/BF03321179

Harris I, Priester W (1962) Time-dependent structure of the upper atmosphere. Journal of Atmospheric Sciences 19(4):286–301, DOI 10.1175/1520-0469(1962)019<0286:TDSOTU>2.0.CO;2

Hedin A, Salah J, Evans J, Reber C, Newton G, Spencer N, Kayser D, Alcaydé D, Bauer P, Cogger L, McClure J (1977) A global thermospheric model based on mass spectrometer and incoherent scatter data MSIS, N2 density and temperature. Journal of Geophysical Research 82(16):2139–2147, DOI 10.1029/JA082i016p02139

Hedin AE (1987) MSIS-86 thermospheric model. Journal of Geophysical Research 92(A5):4649–4662, DOI 10.1029/JA092iA05p04649

Heipke C (2017) Photogrammetrie und Fernerkundung – eine Einführung. Springer Spektrum, Berlin, Heidelberg, DOI 10.1007/978-3-662-47094-7, ISBN 978-3-662-47093-0

Henninger JH (1984) Solar absorptance and thermal emittance of some common spacecraft thermal-control coatings. In: NASA Reference Publication, 1121, NASA

Hofmann-Wellenhof B, Lichtenegger H, Wasle E (2008) GNSS – Global Navigation Satellite Systems. Springer New York, DOI 10.1007/978-3-211-73017-1

Hoque MM, Jakowski N (2007) Higher order ionospheric effects in precise GNSS positioning. Journal of Geodesy 81(4):259–268, DOI 10.1007/s00190-006-0106-0

van den IJssel J, Encarnação J, Doornbos E, Visser P (2015) Precise science orbits for the Swarm satellite constellation. Advances in Space Research 56(6):1024–1055, DOI 10.1016/j.asr.2015.06.002

International Laser Ranging Service (2015) TerraSAR-X. https://ilrs.cddis.eosdis.nasa.gov/missions/satellite_missions/current_missions/tsar_general.html. Online accessed on 2015/01/15.

International Laser Ranging Service (2017a) International Laser Ranging Service mission priorities as of December 25, 2017. https://ilrs.cddis.eosdis.nasa.gov/missions/mission_operations/priorities/index.html. Online accessed on 2017/12/25.

International Laser Ranging Service (2017b) SLRF2014 station coordinates. ftp://ftp.cddis.eosdis.nasa.gov/pub/slr/products/resource/SLRF2014_POS+VEL_2030.0_170605.snx

Jacchia LG (1959) Two atmospheric effects in the orbital acceleration of artificial satellites. Nature 183:526–527, DOI 10.1038/183526a0

Jacchia LG (1965) Static diffusion models of the upper atmosphere with empirical temperature profiles. Smithsonian Contributions to Astrophysics 8:215–258

Jacchia LG (1970) New static models of the thermosphere and exosphere with empirical temperature profiles. Smithsonian Astrophysical Special Report 313:1–79

Jacchia LG (1971) Revised static models of the thermosphere and exosphere with empirical temperature profiles. Smithsonian Astrophysical Special Report 332:1–104

Jacchia LG (1977) Thermospheric temperature, density, and composition: New models. Smithsonian Astrophysical Special Report 375:1–97

Jacchia LG, Slowey J (1973) A study of the variations in the thermosphere related to solar activity. Space Research 1(13):343–348

Jäggi A, Hugentobler U, Beutler G (2006) Pseudo-stochastic orbit modeling techniques for low-Earth orbiters. Journal of Geodesy 80(1):47–60, DOI 10.1007/s00190-006-0029-9

Jäggi A, Hugentobler U, Bock H, Beutler G (2007) Precise orbit determination for GRACE using undifferenced or doubly differenced GPS data. Advances in Space Research 39(10):1612–1619, DOI 10.1016/j.asr.2007.03.012

Jäggi A, Dach R, Montenbruck O, Hugentobler U, Bock H, Beutler G (2009) Phase center modeling for LEO GPS receiver antennas and its impact on precise orbit determination. Journal of Geodesy 83(12):1145–1162, DOI 10.1007/s00190-009-0333-2

Jäggi A, Bock H, Prange L, Meyer U, Beutler G (2011) GPS-only gravity field recovery with GOCE, CHAMP, and GRACE. Advances in Space Research 47(6):1020–1028, DOI 10.1016/j.asr.2010.11.008

Jastrow R, Pearse CA (1957) Atmospheric drag on the satellite. Journal of Geophysical Research 62(3):413–423, DOI 10.1029/JZ062i003p00413

Joint Space Operations Center (2014) Notice advisory to NAVSTAR users (NANU) 2014090. `http://celestrak.com/GPS/NANU/2014/nanu.2014090.txt`, online accessed on 2018/11/25

Joint Space Operations Center (2015a) Notice advisory to NAVSTAR users (NANU) 2011083. `http://celestrak.com/GPS/NANU/2011/nanu.2011083.txt`, online accessed on 2018/11/25

Joint Space Operations Center (2015b) Notice advisory to NAVSTAR users (NANU) 2015091. `http://celestrak.com/GPS/NANU/2015/nanu.2015091.txt`, online accessed on 2018/11/25

Kahle R, Kazeminejad B, Kirschner M, Yoon Y, Kiehling R, D'Amico S (2007) First in-orbit experience of TerraSAR-X flight dynamic operations. In: International Symposium on Space Flight Dynamics

Kedar S, Hajj GA, Wilson BD, Heflin MB (2003) The effect of the second order GPS ionospheric correction on receiver positions. Geophysical Research Letters 30(16):1–4, DOI 10.1029/2003GL017639

Klinkrad H, Fritsche B (1998) Orbit and attitude perturbations due to aerodynamics and radiation pressure. In: ESA Workshop on Space Weather

Knipp D, Tobiska W, Emery B (2004) Direct and indirect thermospheric heating sources for solar cycles 21–23. Solar Physics 224(1):495–505, DOI 10.1007/s11207-005-6393-4

Knocke PC (1989) Earth radiation presure effects on satellites. PhD thesis, The University of Texas at Austin

Knocke PC, Ries JC, Tapley BD (1988) Earth radiation pressure effects on satellites. In: AIAA/AAS Astrodynamics Conference, pp 577–587

Kopp G, Lean JL (2011) A new, lower value of total solar irradiance: Evidence and climate significance. Geophysical Research Letters 38(1):1–7, DOI 10.1029/2010GL045777

Koppenwallner G (2009) Energy accommodation coefficient and momentum transfer modeling. Tech. Rep. TN-08-11, Hyperschall Technologie Göttingen GmbH, Katlenburg Lindau, Germany

Kouba J, Héroux P (2001) Precise point positioning using IGS orbit and clock products. GPS Solutions 5(2):12–28, DOI 10.1007/PL00012883

Kouba J, Mireault Y (1998) IGS orbit, clock and EOP combined products: an update. In: Brunner F (ed) Advances in Positioning and Reference Frames, International Association of Geodesy Symposia, vol 118, Springer, pp 245–251, DOI 10.1007/978-3-662-03714-0_39

Krieger G, Moreira A, Fiedler H, Hajnsek I, Werner M, Younis M, Zink M (2007) TanDEM-X: A satellite formation for high-resolution SAR interferometry. IEEE Transactions on Geoscience and Remote Sensing 45:3317–3340, DOI 10.1109/TGRS.2007.900693

Kubica V, Neyt X, Griffiths H (2015) Improved cross-range resolution in TOPSAR imaging using Sentinel-1A in bistatic operation. In: Radar Conference (RadarCon) 2015, Arlington, VA, USA, DOI 10.1109/RADAR.2015.7130981

Kutschera M, Zajiczek W (2010) Shapiro effect for relativistic particles – testest general relativity in a new window. Acta Physica Polonica B 41(6):1237 – 1246

Lange R, Smutny B (2007) Homodyne BPSK-based optical inter-satellite communication links. In: Mecherle S, Korotkova O (eds) Proceedings of SPIE, vol 6457, DOI 10.1117/12.698646

Langley RB (1999) Dilution of precision. GPS World 10(5):52–59

Laurichesse D, Mercier F, Berthias JP, Broca P, Cerri L (2014) Integer ambiguity resolution on undifferenced GPS phase measurements and its application to PPP and satellite precise orbit determination. Navigation 56(2):135–149, DOI 10.1002/j.2161-4296.2009.tb01750.x

Lichten S (2005) Gipsy-Oasis II: A high precision GPS data processing system and general satellite orbit analysis tool. Tech. rep., Jet Propulsion Laboratory (JPL), Pasadena, California

Llop JV, Roberts PCE, Palmer K, Hobbs S, Kingston J (2015) Descending Sun-synchronous orbits with aerodynamic inclination correction. Journal of Guidance, Control, and Dynamics 38(5):831–842, DOI 10.2514/1.G000183

Loyer S, Perosanz F, Mercier F, Capdeville H, Marty JC (2012) Zero-difference GPS ambiguity resolution at CNES-CLS IGS analysis center. Journal of Geodesy 86(11):991–1003, DOI 10.1007/s00190-012-0559-2

Lyard F, Lefevre F, Letellier T, Francis O (2006) Modelling the global ocean tides: modern insights from FES2004. Ocean Dynamics 56(5–6):394–415, DOI 10.1007/s10236-006-0086-x

Marshall JA, Luthcke SB (1994) Modeling radiation forces acting on TOPEX/Poseidon for precision orbit determination. Journal of Spacecraft and Rockets 31(1):99–105, DOI 10.2514/3.26408

Mayaud PN (1980) Derivation, meaning, and use of geomagnetic indices. In: Geophysical Monograph Series 22, American Geophysical Union, DOI 10.1029/GM022

Mayer-Gürr T, Pail R, Schuh WD, Kusche J, Baur O, Jäggi A (2012) The new combined satellite only model GOCO03s. In: International Symposium on Gravity, Geoid and Height Systems GGHS2012, Venice, Italy

McCarthy DD (1996) IERS Technical Note 21. Tech. rep., U.S. Naval Observatory

McCarthy DD, Petit G (2003) IERS conventions (2003). IERS Technical Note 32, U.S. Naval Observatory and Bureau International des Poids et Mesures

Melbourne W (1985) The case for ranging in GPS based geodetic systems. In: Proceedings 1st Interntaional Symposium on Precise Positioning with the Global Positioning System, NOAA, pp 373–386

Menvielle M, Berthelier A (1991) The K-derived planetary indices: Description and availability. Review of Geophysics 29(3):415–432, DOI 10.1029/91RG00994

Milani A, Nobili AM, Farinella P (1987) Non-gravitational perturbations and satellite geodesy. Adam Hilger Ltd. Bristol

Moe K, Moe MM (2005) Gas-surface interactions and satellite drag coefficients. Planetary and Space Science 53(8):793–801, DOI 10.1016/j.pss.2005.03.005

Moe K, Moe MM, Wallace SD (1998) Improved satellite drag coeffcient calculations from orbital measurements of energy accommodation. Journal of Spacecraft and Rockets 35(3):266–272, DOI 10.2514/2.3350

Moe K, Moe MM, Rice CJ (2004) Simultaneous analysis of multi-instrument satellite measurements of atmospheric density. Journal of Spacecraft and Rockets 41(5):849–853, DOI 10.2514/1.2090

Montenbruck O, Gill E (2005) Satellite Orbits. Springer Berlin Heidelberg

Montenbruck O, Kroes R (2003) In-flight performance analysis of the CHAMP BlackJack GPS receiver. GPS Solutions 7(2):74–86, DOI 10.1007/s10291-003-0055-5

Montenbruck O, Neubert R (2011) Range correction for the Cryosat and GOCE laser retroreflector arrays. In: DLR/GSOC TN 11-01, URL `https://ilrs.cddis.eosdis.nasa.gov/docs/TN_1101_IPIE_LRA_v1.0.pdf`

Montenbruck O, van Helleputte T, Kroes R, Gill E (2005) Reduced dynamic orbit determination using GPS code and carrier measurements. Aerospace Science and Technology 9(3):261–271, DOI 10.1016/j.ast.2005.01.003

Montenbruck O, Andres Y, Bock H, van Helleputte T, van den Ijssel J, Loiselet M, Marquardt C, Silvestrin P, Visser P, Yoon Y (2008) Tracking and orbit determination performance of the GRAS instrument on MetOp-A. GPS Solutions 12(4):289–299, DOI 10.1007/s10291-008-0091-2

Montenbruck O, Garcia-Fernandez M, Yoon Y, Schön S, Jäggi A (2009) Antenna phase center calibration for precise positioning of LEO satellites. GPS Solutions 13(13):23–34, DOI 10.1007/s10291-008-0094-z

Montenbruck O, Hackel S, Jäggi A (2017) Precise orbit determination of the Sentinel-3A altimetry satellite using ambiguity-fixed GPS carrier phase observations. Journal of Geodesy 92(7):711–726, DOI 10.1007/s00190-017-1090-2

Moreira A, Krieger G, Hajnsek I, Hounam D, Werner M, Riegger S, Settelmeyer E (2004) TanDEM-X: A TerraSAR-X add-on satellite for single-pass SAR interferometry. IEEE Transactions on Geoscience and Remote Sensing 2:1000–1003, DOI 10.1109/IGARSS.2004.1368578

NASA (2000) NASA Historical Data Book, vol 6, National Aeronautics and Space Administration NASA Historical Office, Washington, D.C., chap 2, pp 45–46

Neubert R, Grunwaldt L, Neubert J (1998) The retro-reflector for the CHAMP satellite: Final design and realization. In: Proceedings of the 11th International Workshop on Laser Ranging, Deggendorf, Germany

Óhgren M, Bonnedal M, Ingvarson P (2011) GNSS antenna for precise orbit determination including S/C interference predictions. In: Proceedings of the 5th European Conference on Antennas and Propagation (EUCAP), Rome, Italy

Owens J (2002) NASA Marshall Engineering Thermosphere Model 2.0. NASA/TM-2002-211786, Marshall Space Flight Center, Alabama

Pavlis D, Poulose S, Deng C, McCarthy J (2007) GEODYN II System Documentation. SGT-Inc., Greenbelt, contractor report edn

Pavlis E (2009) SLRF2008: The ILRS reference frame for SLR POD contributed to ITRF2008. In: 2009 Ocean Surface Topography Science Team Meeting, Seattle

Pavlis E, Beard R (1996) The laser retroreflector experiment on GPS-35 and 36. In: Beutler G, Hein G, Melbourne W, Seeber G (eds) GPS trends in precise terrestrial, airborne and spaceborne applications, Springer, New York, Berlin, Heidelberg, International Association of Geodesy Symposia, vol 115, pp 154–158

Pearlman MR, Degnan JJ, Bosworth JM (2002) The International Laser Ranging Service. Advances in Space Research 30(2):135–143, DOI 10.1016/S0273-1177(02)00277-6

Perellón M, Alvarez R, Petrini P, Sauer A, Dolce S (2015) Sentinel-1 – spacecraft and SAR antenna thermal design, analysis, verification and flight perfornamces. In: 45th International Conference on Environmental Systems, Washington

Perosanz F, Martyand JC, Balmino G (1997) Dynamic orbit determination and gravity field model improvement from GPS, DORIS and Laser measurements on TOPEX/Poseidon satellite. Journal of Geodesy 71(3):160–170, DOI 10.1007/s001900050084

Peter H, Jäggi A, Fernández J, Escobar D, Ayuga F, Arnold D, Wermuth M, Hackel S, Otten M, Simons W, Visser P, Hugentobler U, Féménias P (2017) Sentinel-1A – first precise orbit determination results. Advances in Space Research 60(5):879–892, DOI 10.1016/j.asr.2017.05.034

Picone JM, Hedin AE, Drob DP, Aikin AC (2002) NRLMSISE-00 empirical model of the atmosphere: Statistical comparisons and scientific issues. Journal of Geophysical Research 107(A12):15–5–15–16, DOI 10.1029/2002JA009430

Pompea SM, Breault RP (2009) Handbook of Optics, vol 2, McGraw-Hill Education, chap 37 Black surfaces for optical systems, pp 37.1–37.70

Poole I (2002) Understanding solar indices. QST G3:38–40

Priestley KJ, Smith GL, Thomas S, Cooper D, Lee RB, Walikainen D, Hess P, Szewczyk ZP, Wilson R (2011) Radiometric performance of the CERES Earth Radiation Budget Climate Record Sensors on the EOS Aqua and Terra Spacecraft through April 2007. Journal of Atmospheric and Oceanic Technology 28(1):3–21, DOI 10.1175/2010JTECHA1521.1

Ray R (1999) A global ocean tide model from TOPEX/Poseidon altimeter: GOT99. TM-209478, NASA Technical Memorandum

Rebischung P, Schmid R (2016) IGS14/igs14.atx: a new framework for the IGS products. In: American Geophysical Union, Fall Meeting 2016

Rees M (1989) Physics and Chemistry of the Upper Atmosphere. Cambridge University Press, DOI 10.1017/CBO9780511573118

Reigber C, Lühr H, Schwintzer P (2002) CHAMP mission status. Advances in Space Research 30(2):129–134, DOI 10.1016/S0273-1177(02)00276-4

Ries JC, Eanes RJ, Tapley BD, Peterson GE (2003) Prospects for an improved Lense-Thirring test with SLR and the GRACE gravity mission. In: Noomen R, Klosko

S, Noll C, Pearlman M (eds) Proceedings of the 13th International Laser Ranging Workshop

Rim HJ, Schutz BE (2002) Geoscience Laser Altimeter System (GLAS), Presicion Orbit Determination (POD). Algorithm Theoretical Basis Document 2.2, Center for Space Research, The University of Texas at Austin

Rodriguez-Solano C, Hugentobler U, Steigenberger P (2012) Adjustable box-wing model for solar radiation pressure impacting GPS satellites. Advances in Space Research 49(7):1113–1128, DOI 10.1016/j.asr.2012.01.016

Rothacher M, Grunwaldt L (2006) The TOR-2 experiment on TanDEM-X. In: TanDEM-X 1st Science Meeting, Dresden

Savcenko R, Bosch W, Dettmering D, Seitz F (2012) EOT11a – Global Empirical Ocean Tide model from multi-mission satellite altimetry, with links to modern results. Tech. Rep. 89, Deutsches Geodätisches Forschungsinstitut (DGFI), DOI 10.1594/PANGAEA.834232

Schaaf SA, Chambré PL (1961) Flow of rarefied gases. In: Princeton Aeronautical Paperbacks, Princeton University Press

Schmid R, Dach R, Collilieux X, Jäggi A, Schmitz M, Dilssner F (2016) Absolute IGS antenna phase center model igs08.atx: status and potential improvements. Journal of Geodesy 90(4):343–364, DOI 10.1007/s00190-015-0876-3

Sensor Systems (2004) GPS S67-1575 series data sheet. Tech. rep., Sensor Systems Inc, Chatsworth, California

Sentman LH (1961) Free molecule flow theory and its applications to the determination of aerodynamic forces. Tech. rep., Lockheed Aircraft Corporation

Shampine LF, Gordon MK (1975) Computer solution of ordinary differential equations: the initial value problem. W. H. Freeman, San Francisco

Shedal (2014) The red book. Tech. rep., Shedal

Shum CK, Woodworth PL, Andersen B, Egbert GD, Francis O, King C, Klosko SM, Provost CL, Li X, Mulines JM, Parke M, Ray RD, Schlax MG, Stammer D, Tierney CC, Vincent P, Wunsch CI (1997) Accuracy assessment of recent oceantide models. Journal of Geophysical Research 102(C11):173–194, DOI 10.1029/97JC00445

Springer T (2009) NAPEOS mathematical models and algorithms. Tech. Rep. DOPS-SYS-TN-0100-OPS-GN, European Space Agency (ESA)

Stammer D, Ray RD, Andersen OB, Arbic BK, Bosch W, Carrére L, Cheng Y, Chinn DS, Dushaw BD, Egbert GD, Erofeeva SY, Fok HS, Green JAM, Griffiths S, King MA, Lapin V, Lemoine FG, Luthcke SB, Lyard F, Morison J, Müller M, Padman L, Richman JG, Shriver JF, Shum CK, Taguchi E, Yi Y (2014) Accuracy assessment of global barotropic ocean tide models. Reviews of Geophysics 52(3):243–282, DOI 10.1002/2014RG000450

Stefanis MD, Melendo I, Cluzet G, Dolce S (2015) Sentinel-3 – spacecraft thermal control: design, analysis and verification approach. In: Proceedings on the 45th International Conference on Environmental Systems, Bellvue, Washington

Steigenberger P, Rothacher M, Dietrich R, Fritsche M, Rülke A, Vey S (2006) Reprocessing of a global GPS network. Journal of Geophysical Research 111(B5):1–13, DOI 10.1029/2005JB003747

Stephens GL, Campbel GG, Haar THV (1981) Earth radiation budgets. Journal of Geophysical Research 86(C10):9339–9760, DOI 10.1029/JC086iC10p09739

Stephens GL, O'Brien D, Webster PJ, Pilewski P, Kato S, Li J (2015) The albedo of Earth. Review of Geophysics 53:141–163, DOI 10.1002/2014RG000449

Sust M, Zangerl F, Montenbruck O, Buchert S, Garcia-Rodriguez A (2014) Spaceborne GNSS-receiving system performance prediction and validation. In: NAVITEC 2014: ESA Workshop on Satellite Navigation Technologies and GNSS Signals and Signal Processing, Noordwijk, NL

Sutton EK, Forbes JM, Knipp DJ (2009) Rapid response of the thermosphere to variations in Joule heating. Journal of Geophysical Research 114(A4):1–7, DOI 10.1029/2008JA013667

Tapley B, Schutz B, Born GH (2004) Statistical Orbit Determination. Elsevier

Tapley B, Bettadpur S, Flechtner F, Watkins M (2011) The status and prospect of the GRACE mission. In: American Geophysical Union, Fall Meeting 2011

Tapley BD, Chambers DP, Bettadpur S, Ries JC (2003) Large scale ocean circulation from the GRACE GGM01 geoid. Geophysical Research Letters 30(22):1–4, DOI 10.1029/2003GL01862

Tapping KF (2013) The 10.7 cm solar radio flux. Space Weather 11(7):394–406, DOI 10.1002/swe.20064

Taylor FW (2005) Elementary Climate Physics. Oxford University Press

Teunissen PJG, Kleusberg A (1998) GPS for Geodesy. Springer Berlin Heidelberg, DOI 10.1007/978-3-642-72011-6, ISBN 978-3-642-72013-0

Teunissen PJG, Montenbruck O (2017) Springer Handbook of Global Navigation Satellite Systems. Springer International Publishing, DOI 10.1007/978-3-319-42928-1

Thébault E, Finlay CC, Beggan CD, Alken P, Aubert J, Barrois O, Bertrand F, Bondar T, Boness A, Brocco L, Canet E, Chambodut A, Chulliat A, Coisson P, Civet F, Du A, Fournier A, Fratter I, Gillet N, Hamilton B, Hamoudi M, Hulot G, Jager T, Korte M, Kuang W, Lalanne X, Langlais B, Léger JM, Lesur V, Lowes FJ (2015) International Geomagnetic Reference Field: the 12th generation. Earth, Planets, and Space 67(79):1–19, DOI 10.1186/s40623-015-0228-9

Torres R, Snoeij P, Geudtner D, Bibby D, Davidson M, Attema E, Potin P, Rommen B, Floury N, Brown M, Traver IN, Deghaye P, Duesmann B, Rosich B, Miranda N, Bruno C, L'Abbate M, Croci R, Pietropaolo A, Huchler M, Rostan F (2012) GMES Sentinel-1 mission. Remote Sensing of Environment 120(15):9–24, DOI 10.1016/j.rse.2011.05.028

Ulrich D, Airbus DS (2013) TeraSAR-X optical properties. priv. comm.

Urschl C, Gurtner W, Hugentobler U, Schaer S, Beutler G (2005) Validation of GNSS orbits using SLR observations. Advances in Space Research 36(3):412–417, DOI 10.1016/j.asr.2005.03.021

Vallado D (2007) Fundamentals of Astrodynamics and Applications, Space Technology Library, vol 21, 3rd edn. Springer New York

Vallado DA, Finkleman D (2008) A critical assessment of satellite drag and atmospheric density modeling. In: AIAA/AAS Astrodynamics Conference

Vallado DA, Kelso T (2013) Earth orientation parameter and space weather data for flight operations. Advances in Astronautical Sciences 148(13):373–393

Vetter JR (2007) Fifty years of orbit determination: Development of modern astrodynamics methods. John Hopkins APL Technical Digest 27(3):239–252

Visconti G (2016) Fundamentals of Physics and Chemistry of the Atmosphere. Springer International Publishing, DOI 10.1007/978-3-319-29449-0, ISBN 978-3-319-29447-6

Švehla D, Rothacher M (2002) Kinematic orbit determination of LEOs based on zero or double-difference algorithms using simulated and real SST GPS data. In: Ádám J, Schwarz KP (eds) Vistas for Geodesy in the New Millennium, International Association of Geodesy Symposia, vol 125, Springer, pp 322–328, DOI 10.1007/978-3-662-04709-5_53

Švehla D, Rothacher M (2005) Kinematic precise orbit determination for gravity field determination. In: Sansó F (ed) A Window on the Future of Geodesy, International Association of Geodesy Symposia, vol 128, Springer Berlin Heidelberg, pp 181–188, DOI 10.1007/3-540-27432-4_32

Wermuth M, Montenbruck O, van Helleputte T (2010) GPS High Precision Orbit Determination Tools (GHOST). In: 4th International Conference on Astrodynamics Tools and Techniques, Madrid

Wernham D (2013) Optical coatings in space. In: Proc. of SPIE, Advances in Optical Thin Films, vol 8168, DOI 10.1117/12.902318

Werninghaus R, Buckreuss S (2010) The TerraSAR-X mission and system design. IEEE Transactions on Geoscience and Remote Sensing 48(2):606–614, DOI 10.1109/TGRS.2009.2031062

Wielicki B, Barkstrom B, Harrison E, Lee R, Smith L, Cooper J (1996) Clouds and the Earth's Radiant Energy System (CERES): An Earth observing system experiment. Bulletin of the American Meteorological Society 77(5):853–868, DOI 10.1175/1520-0477

Wu J, Wu S, Hajj G, Bertiger W, Lichten S (1993) Effects of antenna orientation on GPS carrier phase. Manuscripta Geodetica 18:91–98

Wu SC, Yunck TP, Thornton CL (1991) Reduced-dynamic technique for precise orbit determination of low Earth satellites. Journal of Guidance, Control, and Dynamics 14(1):24–30, DOI 10.2514/3.20600

Wübbena G (1985) Software developments for geodetic positioning with GPS using TI 4100 code and carrier measurements. In: Proceedings 1st Interntaional Symposium on Precise Positioning with the Global Positioning System, NOAA, pp 403–412

Yoon YT, Eineder M, Yague-Martinez N, Montenbruck O (2009) TerraSAR-X precise trajectory estimation and quality assessment. IEEE Transactions on Geoscience and Remote Sensing 47(6):1859–1868, DOI 10.1109/TGRS.2008.2006983

Zangerl F, Griesauer F, Zust M, Montenbruck O, Buchert S, Garcia A (2014) Swarm GPS precise orbit determination receiver initial in-orbit performance evaluation. In: Proceedings of the 2007 National Technical Meeting of The Institute of Navigation (ION GNSS), Tampa, Florida, pp 1459–1468

Ziebart M (2001) High precision analytical solar radiation pressure modelling for GNSS spacecraft. PhD thesis, University of East London

Ziebart M (2004) Generalized analytical solar radiation pressure modeling algorithm for spacecraft of complex shape. Journal of Spacecraft and Rockets 41(5), DOI 10.2514/1.13097

Ziebart M, Adhya S, Sibthorpe A, Edwards S, Cross P (2005) Combined radiation pressure and thermal modelling of complex satellites: Algorithms and on-orbit tests. Advances in Space Research 36(3):424–430, DOI 10.1016/j.asr.2005.01.014

Zumberge J, Heflin M, Jefferson D, Watkins M, Webb F (1997) Precise point positioning for the efficient and robust analysis of GPS data from large networks. Journal of Geophysical Research 102(B3):5005–5017, DOI 10.1029/96JB03860